

Design, Construction and Commissioning of an Ortho-TOF Mass Spectrometer for Investigations of Exotic Nuclei

In Partial Fulfilment of the Requirements for
the Degree of Doctor rer. nat.

II. Physical Institute
Justus-Liebig University Giessen

Prepared by:
Sergey Eliseev
St. Petersburg, Russia

Giessen, Germany

2004

Supervisor and Examiner:

Prof. Dr. Geissel

Examiner:

Prof. Dr. Metag

Examiner:

Prof. Dr. Scheid

Contents

Introduction	1
Chapter 1 Basic principles of modern time-of-flight mass spectrometers.....	5
1.1 Time-of-flight mass spectrometry.....	5
1.2 Radio-frequency quadrupole: ion trapping and cooling	13
1.2.1 Introduction	13
1.2.2 Theory of trapping and cooling.....	15
1.3 Ion sources	19
1.3.1 Electrospray ion source	19
1.3.2 Alkali and Alkali Earths ion source	21
1.3.3 Laser ionization ion source	24
Chapter 2 Experimental set-up	25
2.1 Ion source	25
2.2 Quadrupole.....	33
2.3 Einzel lens	37
2.4 Time-of-flight analyzer	39
2.5 Detection system.....	42
2.6 Vacuum system	46
Chapter 3 Experimental results and discussion.....	48
3.1 Investigation of cooling and trapping of the ions in the radio-frequency quadrupole.....	48
3.1.1 Continuous mode	50
3.1.2 Bunch mode	56
3.2 Precision of mass determination	68
3.3 Investigation of the efficiency and mass resolving power of the Ortho-TOF mass spectrometer.....	74
3.3.1 Efficiency of the Ortho-TOF mass spectrometer	74
3.3.2 Mass resolving power of the Ortho-TOF mass spectrometer	77

Chapter 4 Theoretical investigation of the Ortho-TOF mass spectrometer	79
4.1 Mass resolving power	79
4.2 Efficiency	89
4.3 Further improvement of the Ortho-TOF mass spectrometer	89
Chapter 5 Experiment to characterize the SHIPTRAP gas cell ...	91
5.1 Experiment with the Er-laser source	93
5.2 On-line experiment with $^{107}\text{Ag}^{17+}$ -beam provided from a tandem accelerator	95
5.2.1 Efficiency of the gas cell vs the intensity of the primary Ag-beam...	95
5.2.2 Study of the chemical reactions in the gas cell	105
Chapter 6 <i>On-line</i> mass measurement of ^{107}Ag	110
Summary and outlook	113
Appendix 1: Principle of time-of-flight mass spectrometer.....	I
Appendix 2: Einzel lens	VIII
Appendix 3: Space charge effect on an ion capacity of the linear RFQ trap	XII
Appendix 4: Space charge of He-ions, created in the stopping volume of the gas cell during the stopping of the primary beam	XVIII
Appendix 5: Geometry and electrical settings of the Ortho-TOF mass spectrometer	XXVI
Acknowledgement	XXVIII
References.....	XXX

Zusammenfassung

Präzise Messungen atomarer Massen sind für viele wissenschaftliche Bereiche und technische Anwendungen sehr wichtig. In der Kernphysik sind Massenmessungen von kurzlebigen Nukliden fern ab vom Stabilitätstal von großer Bedeutung zum besseren Verständnis der starken Wechselwirkung. In der nuklearen Astrophysik haben Massen- und Lebensdauer-messungen von Kernen entlang den Pfaden für die Elementsynthese (bspw. r-, rp-Prozesse) in den Sternen eine zentrale Rolle, um den Ursprung und die Zusammensetzung der sichtbaren Materie im Universum zu verstehen. Für Biochemie und Medizin sind Massenmessungen in der Strukturanalyse von komplexen Biomolekülen unverzichtbar. In der Umweltwissenschaft werden Massenmessungen in der Spurenanalyse zur Indikation von Giftstoffen verwendet.

Die präzisesten Massenmessungen an exotischen Nukliden sind entweder auf die Bestimmung der Flugzeit (TOF), der Umlauffrequenz (RF) oder der Zyklotronfrequenz (CF) eines Ions in den elektromagnetischen Feldern der Massenspektrometer zurückzuführen.

Im Rahmen dieser Doktorarbeit wurde ein Flugzeitmassenspektrometer mit orthogonaler Extraktion (Ortho-TOF MS) aufgebaut und in ersten Experimenten erfolgreich eingesetzt. Ziele der Doktorarbeit waren, das Ortho-TOF MS aufzubauen und ausführliche experimentelle Untersuchungen damit durchzuführen. Dabei wurden die Ergebnisse mit Modellrechnungen verglichen, um die Funktionen der verschiedenen Anteile der Spektrometerabschnitte zu verstehen. Der geplante Einsatzbereich der Apparatur sind Massenmessungen und Spektroskopie an exotischen Nukliden.

Das Ortho-TOF MS kann am Wienfilter SHIP für die Massenmessungen von kurzlebigen Fusionsprodukten verwendet werden. Es kann komplementär zu den

SHIPTRAP Penning-Fallen benutzt werden, da diese aufgrund der Meßtechnik keinen Zugang zu den kurzlebigen superschweren Kernen haben. Der große Massenbereich des Ortho-TOF-MS in einem Spektrum ermöglicht es darüber hinaus, dieses als diagnostisches Gerät für die neue Generation von gasgefüllten Ion-Catcher zu verwenden.

Andere Anwendungen, die in der Zukunft realisiert werden können, sind die Untersuchung von chemischen Reaktionen der superschweren Kerne und die massenaufgelöste Zerfallspektroskopie von Nukliden. Beispielsweise können die doppelmagischen ^{100}Sn Isotope die mit hohen Produktionsquerschnitten in Fusionsreaktionen gebildet werden, auch der Spektroskopie zugänglich gemacht werden. Obwohl ^{100}Sn Ionen am Fragmentseparator FRS entdeckt wurden, so ist die Häufigkeit dieser Reaktionsprodukte an der Coulomb Barriere etwa um einen Faktor 1000 größer. Jedoch fehlt in diesem Energiebereich die selektive Separation. In Zukunft wird eine solche Spektroskopie mit einem entsprechenden Massenfilter nach dem Ortho-TOF Prinzip von unserer Gruppe angestrebt.

Die Entwicklung der Flugzeitspektrometer hat in unserem Institut schon eine längere Tradition, jedoch waren die Anwendungsgebiete und damit die Anforderungen sehr verschieden. So nützt es wenig, wenn eine hohe Massenauflösung erreicht wird, aber die niedrige Akzeptanz und Transmission für die exotischen Kerne nicht adäquat sind. Deshalb wurde zunächst eine ausführliche Untersuchung der Kühlungs- und Speicherverhalten des RF-Quadrupoles durchgeführt. Der RF-Quadrupol hat eine zentrale Rolle im Massenspektrometer, da er den Eingangsphasenraum präpariert und festlegt.

Da das Ortho-TOF-MS ein universelles Gerät mit einem großen Massenbereich ist, wurde es erfolgreich auch als Diagnosegerät für die Charakterisierung und Optimierung der SHIPTRAP Gaszelle in Experimenten am Münchner Tandem – Beschleuniger eingesetzt. Gerade für die Analyse der möglichen chemischen Reaktionen in der Gaszelle sind solche Messungen essentiell.

Die maximale Effizienz des hier entwickelten Ortho-TOF-MS beträgt 1% und 3% jeweils für den kontinuierlichen und den gepulsten Betrieb. Dieses Ergebnis entspricht den theoretischen Abschätzungen und ist durchaus für Experimente am SHIP geeignet.

Die erreichte maximale Präzision in einer Massenbestimmung mit den Pb-Isotopen ist besser als 0,7 ppm, entsprechend etwa 100 keV. Theoretische Vorhersagen mit mikroskopischen Modellen sind derzeit noch um Faktoren von 5 bis 10 schlechter für exotische Kerne, so daß mit einer solchen Messgenauigkeit noch gute Beiträge zum besseren Verständnis der Kernbindungsenergie geleistet werden können.

Die *on-line* Massenmessungen von stabilen ^{107}Ag Projektionen am Münchner Tandem-Beschleuniger erreichten eine Präzision von 1.3 ppm, entsprechend 130 keV und sind somit etwas schlechter als die off-line Pb-Experimente. Jedoch sind die Präzision und die absolute Genauigkeiten in Zukunft leicht mit den gewonnen Erkenntnissen aus dieser Arbeit zu verbessern.

Introduction

Precise atomic mass measurements are very important in many disciplines of science, e.g. in physics, biochemistry, medicine, archaeology and environmental research. In nuclear physics, mass measurements of nuclides are essential for testing nuclear mass models. From the knowledge of the mass of a nuclide the nuclear binding energy can be derived. The mass measurements provide a better knowledge of the strong interaction between the constituents in the nucleus. In nuclear astrophysics, mass measurements of exotic nuclides are of great importance for our understanding of the synthesis of the elements. In biochemistry and medicine, mass measurement methods are helpful in a structural analysis of complex biomolecules. Mass measurement techniques are widely used in the trace analysis of poisonous substances in environmental research. Leak searchers and rest gas analysers are also based on the principles of mass measurements.

The most precise methods of mass measurements, employed in nuclear physics, are based either on the determination of the time of flight (TOF), the revolution frequency (RF), or cyclotron frequency (CF) of the ion in mass spectrometers. Nowadays, there are several scientific centers such as GSI, CERN, GANIL and ANL employing these techniques. The RF-technique is realized at GSI in the Experimental Storage Ring (ESR) [Fra87] (Schottky Mass Spectrometry SMS and Isochronous Mass Spectrometry IMS) for ions produced in the in-flight Fragment Separator (FRS) [Gei92]. At GANIL, the TOF-technique is employed at the Second Separated-Sector Cyclotron (CSS2) and at the Spectromètre à Perte d'Énergie du Ganil (SPEG) [Bia89, Aug94]. The CF-technique is implemented in MISTRAL [Lun01] and in Penning traps ISOLTRAP [Bol87, Her03] at ISOLDE (CERN). The CF-technique is also used at SHIPTRAP [Dil01, Sik03] at GSI and at the Canadian Penning Trap (CPT), coupled to the Argonne Tandem Linac Accelerating System (ATLAS) at ANL [Sav01]. In the following diagram 1, the relative accuracy of mass determination achieved by the above mentioned techniques and typical half-lives reached by each method are presented.

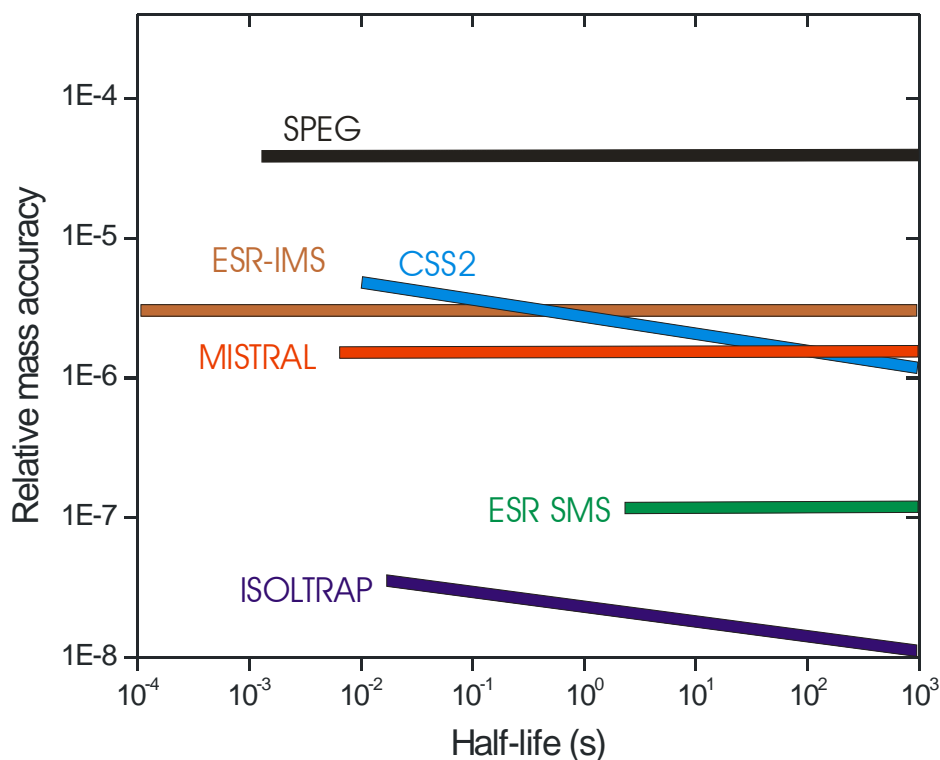


Diagram 1: Relative accuracy of mass determination achieved by the above mentioned techniques and typical half-lives reached by each method

The IMS is expected to give access to very short-lived nuclides. The highest relative mass accuracy for exotic nuclides (10^{-8}) can be reached nowadays at ISOLTRAP.

Besides the techniques mentioned above there is a class of relatively small (transportable) mass spectrometers based on the time-of-flight technique. Having the accuracy of mass determination of exotic nuclei and access to short lived nuclei comparable to the methods mentioned above, such mass spectrometers have a broad mass band. Such versatile mass spectrometers (TOF MS) are intensively used in all disciplines of science. The first report on a TOF MS is dated by the late 1940s by Cameron and Eggers [Cam48]. Wiley and McLaren in 1955 [Wil55] built a linear system with the mass resolving power of about 100. The low mass resolving power, the lack of electronics that can operate in a nanosecond time range and the absence of detectors suitable for such applications were the reasons for the very slow development of TOF MS during the following two decades. The second birth of time-of-flight mass spectrometry in the late 1980s was enabled by several break-

throughs in the design of TOF MS, by the development of micro-channel plates, by advances of fast timing electronics and by the invention of new ionization methods. The realization of double stage ion reflectors by Mamyrin [Mam73] and grid-free reflectors by Wollnik and Piyadasa [Wol99,Piy99] in TOF-MS increased the mass resolving power up to a few thousands. The invention of the orthogonal extraction method by Dodonov [Dod87,Dod91] allowed to increase the sensitivity of TOF-MS without sacrificing mass resolving power.

For the registration of the ions in TOF-MS, micro-channel plate detectors are used nowadays [Wiz79,Wur94,Wur96]. Such MCP detectors usually provide a peak width of less than a nanosecond for a single ion.

For the data acquisition, the time-to-digital converter (TDC) is best suited due to its high time resolution of the order of 100ps and its small dead time of the order of a few nanoseconds.

The invention of matrix-assisted laser desorption ionization (MALDI) [Kar88] and electrospray ionization (ESI) [Men88,Fen89] has caused a revolution in the mass spectrometry for biological research.

In this thesis a mass spectrometer with orthogonal extraction based on the TOF-technique is presented (Ortho-TOF MS). The goal in this thesis was to build and commission the Ortho-TOF MS and to perform comprehensive theoretical and experimental investigations of the Ortho-TOF MS for the application in nuclear physics such as mass measurements of exotic nuclides.

The Ortho-TOF MS can be used at SHIPTRAP for mass measurements of short-lived nuclides. It will be complementary to the SHIPTRAP Penning trap in the cases when an access to the nuclides with the half-lives of a few 10 ms is required.

The broad mass range of the Ortho-TOF MS gives the valuable possibility to use the Ortho-TOF MS as a diagnostic tool for characterization of the SHIPTRAP gas cell and the Ion-Catcher gas cell at the FRS.

Other applications that may be attempted in the future are the investigation of chemistry of super heavy nuclides (ion mobility, reaction rates) and the decay spectroscopy of mass-identified nuclides. A good example is double magic ^{100}Sn .

This thesis consists of six chapters. In Chapter 1 basic principles of time-of-flight mass spectrometry are described. The experimental set-up (Ortho-TOF MS) is

subject of Chapter 2. Chapter 3 presents a detailed experimental investigation of the constituents of the Ortho-TOF MS that affect the mass resolving power, accuracy of mass determination and efficiency. The achieved mass resolving power, accuracy of mass determination and efficiency of the Ortho-TOF MS and their consistency with the theoretical predictions are also the subject of Chapter 3. A comprehensive theoretical investigation of the individual parts of the Ortho-TOF MS with respect to such important parameters of the Ortho-TOF MS as the mass resolving power, accuracy of mass determination and efficiency are presented in Chapter 4. Chapter 5 describes the on-line test of the SHIPTRAP gas cell with the Ortho-TOF MS. Mass measurements that took place in Garching, are presented in Chapter 6.

Chapter 1

Basic principles of modern time-of-flight spectrometers

1.1 Time-of-flight mass spectrometry

The basic principles of time-of-flight mass spectrometry can be understood from Fig.(1-1). Ions with different mass-to-charge ratios (M/Q) have different flight-times along the path l . After passing the path l they get spatially separated at the detector.

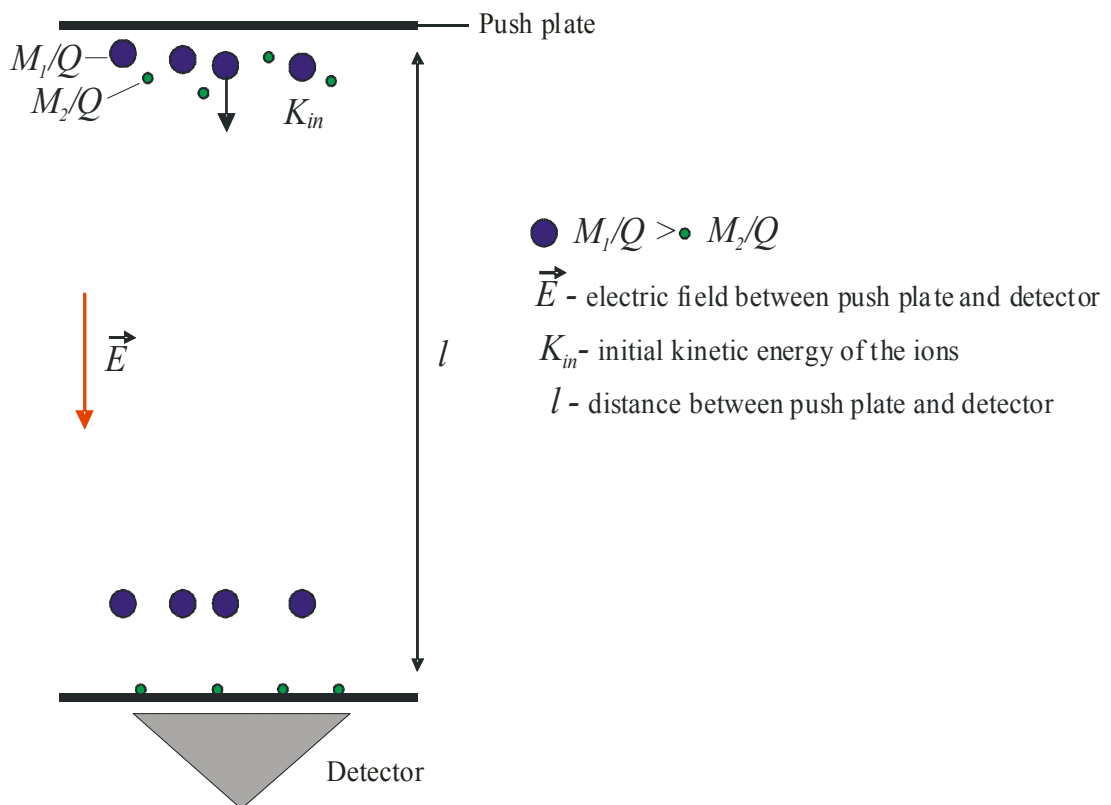


Fig.(1-1): Basic principle of time-of-flight mass spectrometry. Ions with different mass-to-charge ratios (M/Q) have different flight-times along the path l . After passing the path l they get spatially separated at the detector.

The time of flight of ions with mass M , electric charge Q and initial kinetic energy $K_{in}=0$ along the path l can be expressed as follows (see Appendix 1):

$$t = \sqrt{\frac{M}{Q}} \times \sqrt{\frac{2l}{E}} \quad (1_1)$$

It can be seen that a time-of-flight spectrometer separates ions with respect to their mass-to-charge M/Q .

A schematic view of a linear time-of-flight mass spectrometer (linear TOF MS) is shown in the Fig.(1-2) [Wil55,Wil00]. It consists of an ion source, an acceleration region, a drift tube and a detector. The three regions are separated by grids. Ions are stored or generated in the ion source. After the DC electric fields E_1 and E_2 are applied between the push plate and the grid 1 (G1), and G1 and grid 2 (G2) (see Fig.(1-2)), the ions start moving towards the detector with the energy K gained by passing the regions with the electric fields E_1 and E_2 . If the ions were at rest in the ion source, their time of flight can be expressed as follows (Appendix 1):

$$t = t_1 + t_2 + t_3 \quad (1_2)$$

$$t_1 = \sqrt{\frac{M}{Q}} \frac{2l_1}{\sqrt{2l_1E_1}} \quad (1_3)$$

$$t_2 = \sqrt{\frac{M}{Q}} \frac{2l_2}{\sqrt{2(l_1E_1 + l_2E_2)} + \sqrt{2l_1E_1}} \quad (1_4)$$

$$t_3 = \sqrt{\frac{M}{Q}} \frac{l_3}{\sqrt{2(l_1E_1 + l_2E_2)}} \quad (1_5)$$

Here, t_1 , t_2 , t_3 are the time-of-flight of the ion in the ion source, the acceleration region and the field-free drift tube, respectively, l_1 is the distance between the start position of the ion and the first grid G1, E_1 is the extracting field strength in the ion source, E_2 is the accelerating field strength, l_2 and l_3 are the lengths of the acceleration region and the field-free drift tube.

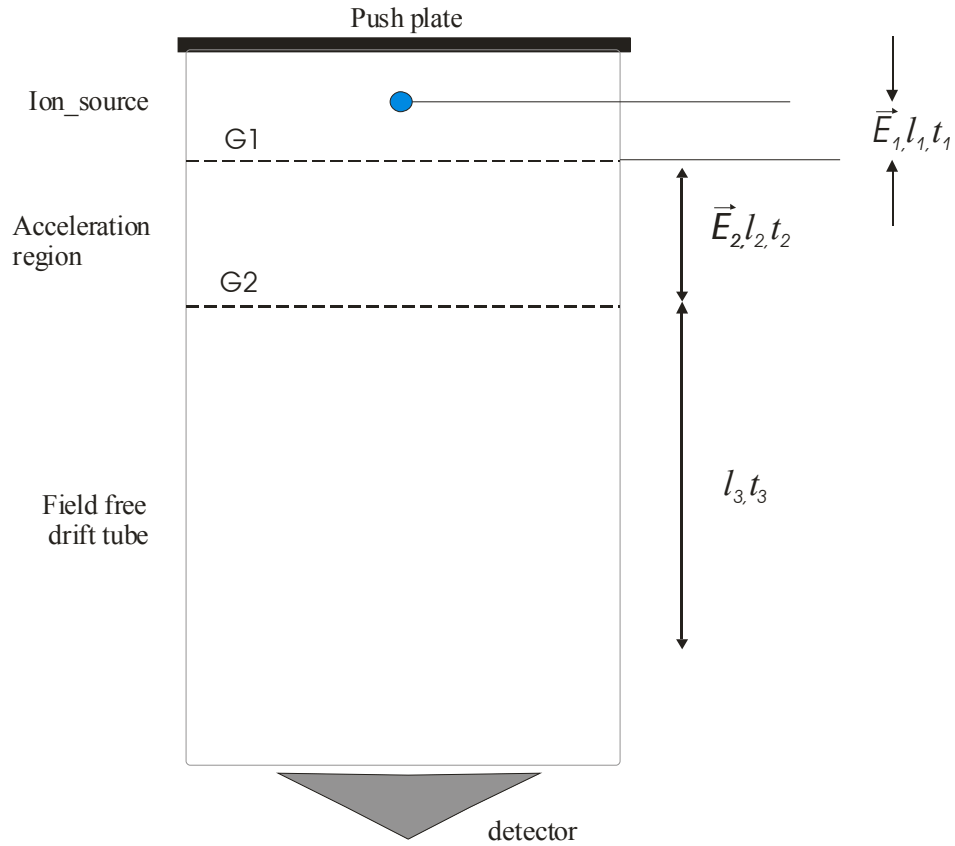


Fig.(1-2): Schematic view of a simple linear time-of-flight mass spectrometer [Wil55,Wil00]. It consists of an ion source, an ion acceleration region, a field free drift tube and a detector. Ions are stored or generated in the ion source. After the DC electric fields E_1 and E_2 are applied between the push plate and grid 1 (G1), and G1 and grid 2 (G2), the ions start moving towards the detector with the kinetic energy K gained by passing the regions with the electric fields E_1 and E_2 . The total flight-time of the ions ($t_1+t_2+t_3$) is a measure for M/Q .

The mass resolving power of a time-of-flight mass spectrometer R_m can be derived from the time resolving power R_t as follows (see Eq.(1_1)):

$$\Delta t = \frac{1}{2} \sqrt{\frac{l}{MQ}} \times \sqrt{\frac{2l}{E}} \Delta M \quad (1_6)$$

$$R_m = \frac{M}{\Delta M} = \frac{1}{2\Delta t} \sqrt{\frac{M}{Q}} \times \sqrt{\frac{2l}{E}} = \frac{t}{2\Delta t} = \frac{R_t}{2} \quad (1_7)$$

Thus the mass resolving power R_m is given by

$$R_m = \frac{R_t}{2} \quad (1_8)$$

Here the finite time interval Δt corresponds to the full-width at half-maximum height of the spectral peak (FWHM).

It can be seen from Eq.(1_2)-Eq.(1-5) that the time-of-flight for the ions with the same M/Q is the same only if the initial position of the ions in the ion source is the same. In reality the ions in an ion source have both finite spatial and velocity distributions in the z -direction. Fig.(1-3) illustrates four different possibilities:

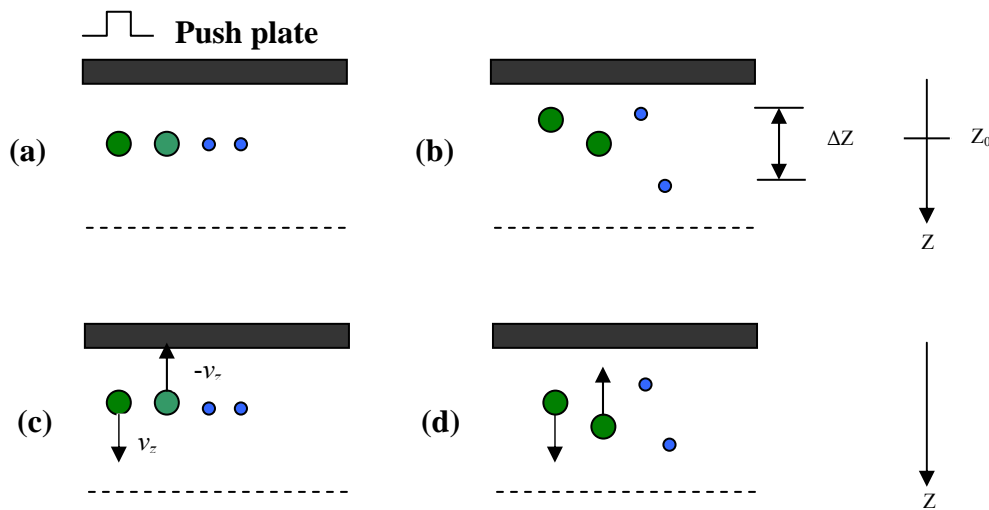


Fig.(1-3): Four different initial conditions of ions in the ion source. Case (a) shows the ideal case when there is neither a spatial nor a velocity and velocity spread in z -direction. In case (b) the ions have a spread Δz and zero velocity and zero velocity spread in the z -direction. In case (c) the ions have different initial velocities in the z -direction but no a spatial spread. Case (d) is a realistic situation of ions in a ion source, where they have a spatial spread Δz and a velocity spread in the z -direction.

Case (a) shows the ideal case when there is neither a spatial nor a velocity and velocity spread in z -direction. In case (b) the ions have a spread Δz and zero velocity and velocity spread in the z -direction. In case (c) the ions have different initial velocities in the z -direction but without a spatial spread. Case (d) is the common situation of ions in a ion source, where ions have a spatial spread Δz and a velocity spread in the z -direction .

A characteristic feature of a time-of-flight mass spectrometer is its ability to compensate (to some extent) a finite spatial distribution of the ions (see Fig.(1-3)

(b)). This feature is referred to as spatial focusing. The time-of-flight of an ion from the start point z to the detector can be expanded:

$$t(z) = t_0 + \frac{I}{1!} \left[\frac{\partial t(z)}{\partial z} \right]_{z=z_0} \Delta z + \frac{I}{2!} \left[\frac{\partial^2 t(z)}{\partial z^2} \right]_{z=z_0} \Delta z^2 + \dots \quad (1_9)$$

where z_0 is a reference start position of the ion in the ion source, $\Delta z = z - z_0$.

Usually the condition of spatial focusing is formulated as follows:

$$\begin{aligned} \left[\frac{\partial t(z)}{\partial z} \right]_{z=z_0} &= 0 \\ &\vdots \\ \left[\frac{\partial^n t(z)}{\partial z^n} \right]_{z=z_0} &= 0 \end{aligned} \quad (1_{10})$$

where n is the order of spatial focusing. It is clear that the higher an order of spatial focusing is, the wider the spatial spread Δz that can be compensated. It is easy to be shown that for a linear time-of-flight mass spectrometer (Fig.(1-2)) only the second order of spatial focusing can be fulfilled. The second order of spatial focusing can be obtained by selecting the flight length l_3 according to the condition [Wil55]:

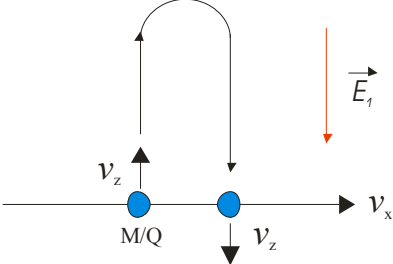
$$l_3 = 2z_0 k_0^{\frac{3}{2}} \left(1 - \frac{I}{k_0 + \sqrt{k_0}} \frac{l_2}{z_0} \right) \quad (1_{11})$$

where $k_0 = \frac{z_0 E_1 + l_2 E_2}{l_1 E_1}$ and l_1, l_2, E_1, E_2 are defined in Eq.(1_2)-Eq.(1_5).

A linear time-of-flight mass spectrometer with 2 mm initial spatial spread of the beam would have a resolving power ~ 6400 at a total flight distance of 20 cm. But the presence of a velocity distribution of the ions in the z -direction (see Fig.(1-3) (c) and (d)) leads to a substantial reduction of the mass resolving power of such a linear time-of-flight mass spectrometer.

Let us consider two ions I_1 and I_2 with the same initial velocity Δv_z , however moving in opposite directions, as shown in Fig.(1-3) (c). Ion I_1 moves towards the push plate and is decelerated by the extraction field E_1 until it stops. It is then re-

accelerated, returning to the starting position with its original speed but in the reversed direction. Subsequently, the later motion of the ion I_1 is identical to that of the ion I_2 but delayed by the turn-around time. This turn-around time, Δt_{turn} , can be calculated as follows:

$$\Delta t_{turn} = \frac{2M \Delta v_z}{QE_1} \quad (1_{12})$$


This flight time error caused by the initial velocity spread can not be compensated by any constant stationary electrical field.

For a linear time-of-flight mass spectrometer the time-of-flight distance and, therefore, the time of flight t is coupled to the extraction field E_1 and l_1 (see Fig.(1-2)), therefore, to the turn-around time Δt_{turn} . It limits the mass resolving power to a few hundred for acceptable system parameters. Although several techniques were used for the design of a linear time-of-flight mass spectrometer, the mass resolving power could not be increased above ~ 5000 [Daw87,Gru94,Kev85]. Higher mass resolving powers could only be achieved in reflection time-of-flight mass spectrometers.

A reflection time-of-flight mass spectrometer (see Fig.(1-4)) consists of an ion source, an accelerator, a field-free drift tube, a reflector and an ion detector. The addition of the reflector decouples the time-of-flight distance from the extraction field E_1 and l_1 . It allows to increase the time of flight t and, therefore, the mass resolving power, independently on E_1 and l_1 . The idea of a reflection time-of-flight mass spectrometer is that the variations of the time-of-flight due to different ion energies are compensated by corresponding variations of their time-of-flight in the reflector, i.e. ions with higher energies will penetrate more deeply into the reflector and therefore travel on a longer flight path inside the reflector.

For an ion which was at rest before acceleration, the total time-of-flight in a reflection time-of-flight mass spectrometer as shown in Fig.(1-4) can be expressed as follows (see Appendix 1):

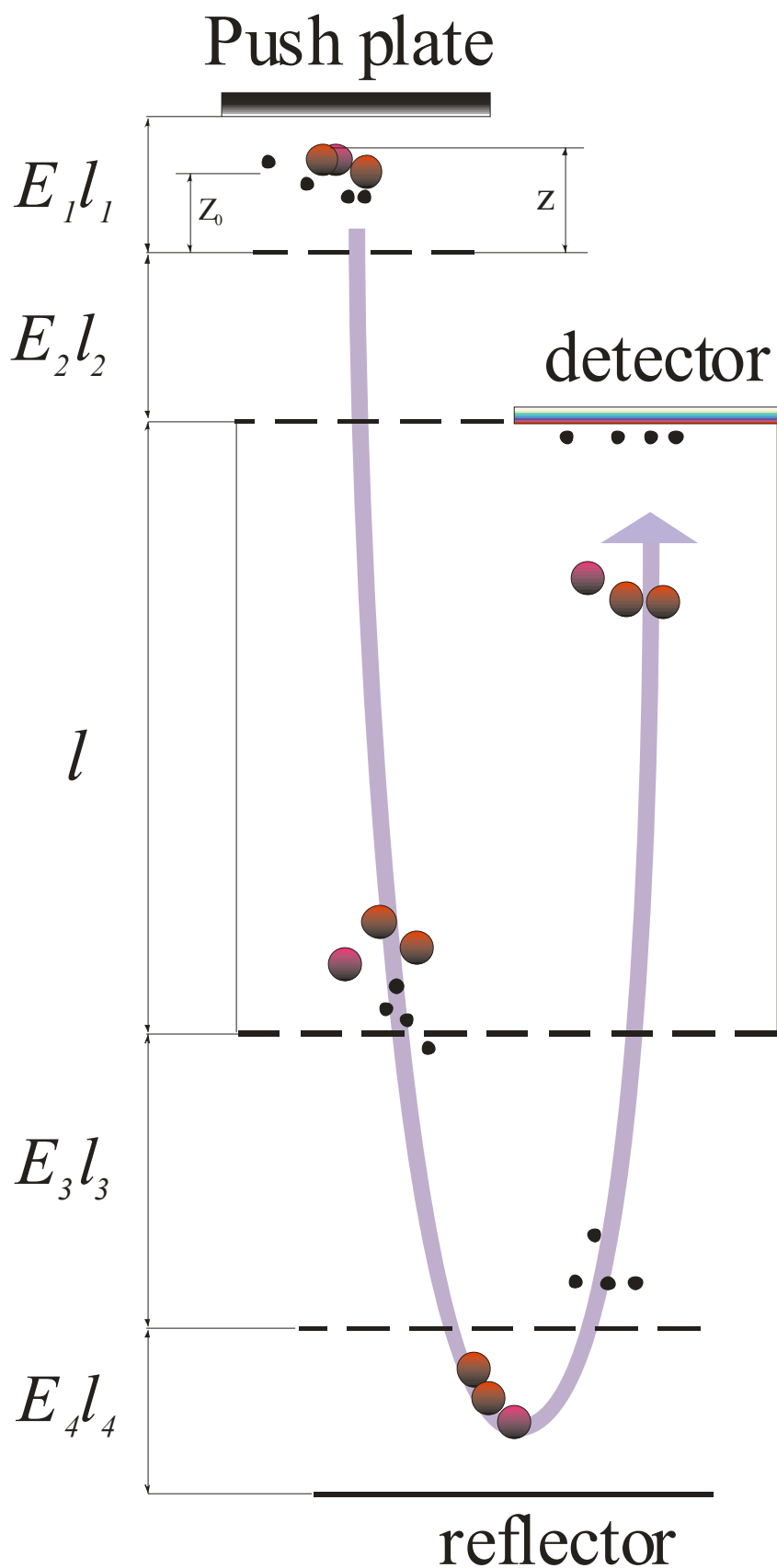


Fig.(1-4): Schematic view of a reflection time-of-flight mass spectrometer. It consists of an ion source, an ion accelerator, a field-free drift tube, a reflector and an ion detector. The addition of the reflector decouples the time-of-flight distance from the extraction field E_1 and l_1 . It allows to increase

the time of flight t and, therefore, the mass resolving power, independently on E_1 and l_1

$$t(z) = \sqrt{\frac{2M}{QE_1}} \left[\left(1 - \frac{E_1}{E_2}\right) \sqrt{z} + \left(\frac{E_1}{E_2} - 2\frac{E_1}{E_3}\right) \sqrt{z + \frac{l_2 E_2}{E_1}} + \right. \\ \left. + \frac{l}{\sqrt{z + \frac{l_2 E_2}{E_1}}} + 2\left(\frac{E_1}{E_3} - \frac{E_1}{E_4}\right) \sqrt{z + \frac{l_2 E_2}{E_1} + \frac{l_3 E_3}{E_1}} \right] \quad (1_{13})$$

where z is the start position of the ion, $\frac{M}{Q}$ is the mass-to-charge ratio of the ion,

E_1 is the extracting field strength, E_2 is the accelerating field strength, E_3 is the field strength of the first stage of the reflector, E_4 is the field strength of the second stage of the reflector, l_1, l_2, l, l_3, l_4 are the length of the ion source, the ion accelerator, the drift tube, the first stage of the reflector and the second part of the reflector.

If the average ion start position z_0 in Fig.(1-4) is taken as the reference for the start position of the ion, Eq.(1_13) can also be written as:

$$t(z) = t_0 + \frac{1}{1!} \left[\frac{\partial t(z)}{\partial z} \right]_{z=z_0} \Delta z + \frac{1}{2!} \left[\frac{\partial^2 t(z)}{\partial z^2} \right]_{z=z_0} \Delta z^2 + \dots \quad (1_{14})$$

Postulating the condition for second order focusing

$$\left[\frac{\partial t(z)}{\partial z} \right]_{z=z_0} = 0 \\ \left[\frac{\partial^2 t(z)}{\partial z^2} \right]_{z=z_0} = 0 \quad (1_{15})$$

one can find the relations between E_1, E_2, E_3, E_4 and l_1, l_2, l, l_3, l_4 . (See Appendix 1).

1.2 Radio-frequency quadrupole: ion trapping and cooling

1.2.1 Introduction

A radio-frequency quadrupole (RFQ) is an electrode structure which, if RF and DC potentials are applied to it with appropriate polarities and phases, confines the motions of charged particles to a small region of space. The two dimensional trapping effect of an alternating quadrupole electric field is achieved by using four hyperbolic cylinders mounted symmetrically about a central axis as shown schematically in Fig.(1-5). This effect was discovered independently by Paul and his colleagues[Pau53] and by Post[Pos53] in 1953.

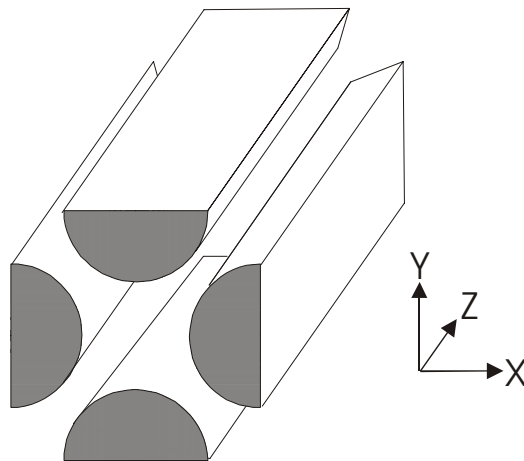


Fig. (1-5): Schematic view of a quadrupole ion guide. A radio-frequency quadrupole (RFQ) is an electrode structure which, if RF and DC potentials are applied to it with appropriate polarities and phases, confines the motions of charged particles to a small region in space. The two dimensional trapping effect of an alternating quadrupole electric field is achieved by using four hyperbolic cylinders mounted symmetrically about a central axis.

The axial motion of the ions in such a device remains free. By application of the proper amount of non-alternating (DC) quadrupole field, the radial confinement can be made to be dependent on the mass of the ion. By application of an electric potential of a certain profile along the axis Z , three-dimensional confinement of the ions can be achieved.

The theory of the radio frequency quadrupole is considered in [Daw76], where it is shown that the motion of the ions in the RFQ can be described roughly by introducing a “pseudo-potential” which is independent of time.

Unlike the real potential, the pseudo-potential can have a minimum at the same position in space for both the negative and the positive ions, thus trapping both types at once.

Here, as an introduction, a qualitative description of the ion motion in the RFQ will be given.

Let us consider the total effect of an alternating electric field over one cycle. Over exactly one-half of the cycle the ion is pushed toward the stronger electric field region (away from trap center) while over the other half it is pushed toward the weaker region (toward trap center). However, the push toward the stronger field, which occurs while the ion is in the weaker field, will be weaker than the push toward the weaker field region. Hence the ion will progress toward the weaker field. Since the weakest field of a quadrupole is at its center, where it is zero, the ions will be driven to collect about the axis.

It was thought long time that such RF-devices can function only at high vacuum ($10^{-4} - 10^{-7}$ mbar). In 1992 the collisional focusing effect of ions in RFQ at increased pressure was discovered [Dou92]. The ions, moving in an alternating quadrupole field and undergoing collisions with residual gas, are focused on the axis of the quadrupole. If the ions originally have large spatial and energy distributions (a large phase space), then while moving in the RFQ their phase space becomes smaller and their energy distribution approaches a Maxwell-Boltzmann distribution related to the corresponding temperature of the residual gas (thermalization of ions). First the effect of “thermalization of ions” in an RFQ was used for an investigation of low temperature ion-molecular reactions [Die92]. On the other hand, such a method of reducing the phase space of an ion beam has proved to be very useful and promising in mass-spectrometry, because the phase space of ions is directly related to the resolving power and a sensitivity of a mass-spectrometer. In the work [Moo88] the ions from an accelerator after collecting and cooling in a three-dimensional quadrupole trap were injected into a time-of-flight mass spectrometer for mass analysis.

For the first time in the works [Kru95,Kru98] such an RFQ with buffer gas was used with an electrospray ion source. Recently [Lob98] it was coupled to a MALDI ion source. In the work [Koz99] such a device was used as a molecular-ion reactor (MIR) for the investigation of different fragmentation reactions.

1.2.2 Theory of trapping and cooling

A very detailed survey of the theory and properties of different multipole ion-transport systems is presented in the works [Die92,Daw76].

In this work only RF-only mode of a radio-frequency quadrupole is considered.

The movement of ions in RF-multipoles with residual gas was analyzed with help of different analytical and numerical methods [Kru98, Die92, To197, Mar89, To097]. While the method of numerical modeling has many advantages such as, for instance, precise calculations of ion trajectories in an RFQ, it is not illustrative and it does not give a possibility to make conclusions about behavior of the system with respect to some basic parameters of an RFQ. Thus, in spite of many restrictions, approximate analytical methods of describing such system have been proven to be very useful and promising. In the work [Daw76] applying a method of the theory perturbation theory in its most general form an expression for so-called pseudo-potential in case of a movement of ions *in vacuum* was derived.

$$U_{eff}(r) = \frac{Q V_{rf}^2}{M\Omega^2 r_0^4} r^2 \quad (1_{16})$$

where $U_{eff}(r)$ is a pseudo-potential, independent of time, Q and M are the electrical charge and mass of the ion respectively, V_{rf} is the amplitude of harmonically oscillating electric potential, r is the average coordinate of the ion, Ω is the angular frequency of electric potential.

The method implemented in the work [Tol97] has been proven to be very fruitful. In this approach the collisions of the ion with the molecules of the residual gas is considered(viscous force approach [Mar89]).

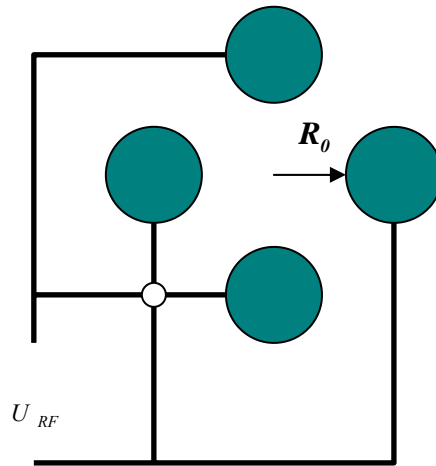


Fig.(1-6): In technical realization a typical RF-only quadrupole consist of four *cylindrical* rods, to which potentials in RF-only mode are applied in pairs.

Undergoing a collision with a residual gas molecule the ion changes its velocity. In the work [Tal62] it was shown that the ion with the kinetic energy less than a few eV and the residual gas molecule produce a compound during the collision, therefore after the collision their flight progresses isotropically.

Provided the residual gas molecule is at rest before a collision with the ion and gains the velocity equal to the mean velocity of the ion after a collision (which is valid for heavy ions, $\frac{M}{m} \gg 1$), one can write an equation of momentum balance for the ion moving in gas [Koz99]:

$$QE\Delta t = M\Delta v + mv\omega\Delta t \quad (1_{17})$$

where E is the electrical field strength, M , v , Q is the mass, mean velocity and electrical charge of the ion, m is the mass of the residual gas molecule, $\omega=kn$ is the mean frequency of collisions of the ion with molecules of the residual gas per time unit, k is a gas-kinetic constant of collisions, and n is the density of the gas molecules. For $\Delta t \rightarrow 0$ Eq.(1_17) can be transformed into the following form:

$$\frac{dv}{dt} + \frac{v}{\tau} = \frac{QE}{M} \quad (1_{18})$$

where $\tau = \frac{M}{m\omega}$ is the characteristic time of relaxation of the ion velocity.

In the approximation when ω depends weakly on the ion velocity the so-called mobility ratio is fulfilled:

$$v = \kappa E = \frac{\tau Q}{M} E \quad (1_{19})$$

where $\kappa = \frac{\tau Q}{M}$ is the ion mobility.

Let us consider the movement of the ion in an RF-only quadrupole with residual gas. In a practical technical realization a typical RF-only quadrupole consist of four *cylindrical* rods, to which potentials in RF-only mode are applied in pairs (see Fig.(1-6)). In such a geometry the electrical field between the rods can be described by two independent components [Daw76] (This holds for ideal hyperbolic rods and only approximately for cylindrical rods):

$$\begin{aligned} E_x &= \frac{2x}{r^2} V_{rf} \cos \Omega t \\ E_y &= -\frac{2y}{r^2} V_{rf} \cos \Omega t \end{aligned} \quad (1_{20})$$

where Ω is the angular frequency and V_{rf} is the amplitude of the radio-frequency voltage applied to a pair of the rods, r_0 is the distance between the axis of the quadrupole and the rod. In this case Eq.(1_18) can be separated into two independent equations for the x – and y- coordinates:

$$\begin{aligned} \frac{d^2 x}{dt^2} + \frac{1}{\tau} \frac{dx}{dt} &= \frac{2x}{r_0^2} \frac{QV_{rf}}{M} \cos \Omega t \\ \frac{d^2 y}{dt^2} + \frac{1}{\tau} \frac{dy}{dt} &= -\frac{2y}{r_0^2} \frac{QV_{rf}}{M} \cos \Omega t \end{aligned} \quad (1_{21})$$

These equations are identical to the Mathieu equation [Daw76] for ion movement in vacuum except for the second term in Eq.(1_21) that is called a viscous term.

A solution of these equations [Tol97] allows to obtain formulae for the pseudo-potential and a mean radius squared of the ion beam in presence of residual gas in the RF-quadrupole:

$$U_{eff}^{quad} = \frac{V_{rf}^2 r^2}{(M/Q)\Omega^2 r_0^4} \frac{\Omega^2 \tau^2}{1 + \Omega^2 \tau^2} \quad (1_{22})$$

$$R_0^2 = \frac{M}{Q^2} \frac{\Omega^2 r_0^4}{V_{rf}^2} k_b T_0 \frac{1 + \Omega^2 \tau^2}{\Omega^2 \tau^2} \quad (1_{23})$$

The stability of ion movement in a RF-quadrupole in case of vacuum is characterized by the Mathieu-parameter q [Daw76],

$$q = \frac{4QV_{rf}}{Mr_0^2 \Omega^2} \quad (1_{24})$$

In case of vacuum ($1/(\Omega\tau) \rightarrow 0$), when $q > 0.906$, the movement of ions in an RF-quadrupole becomes unstable; Mean velocity and oscillation amplitude of ions increase exponentially with time. Since such a situation is realized at

$$M = M_0 = \frac{4QV_{rf}}{0.906r_0^2 \Omega^2}, \text{ this mass is called light-ion-mass cut-off.}$$

With a growth of the viscous friction, the relaxation time τ becomes smaller, which according to Eq.(1_22) leads to a reduced pseudo-potential and an increased mean radius of the ion beam.

In a pseudo-potential, focusing ions on the axis of a quadrupole, the average movement of the ion due to collisions with residual gas molecules is a periodic or non-periodic relaxation depending on friction magnitude [Koz99]. The ions are focused on the axis of the quadrupole, the kinetic energy spread of the ions in stationary condition is doubled kinetic energy spread of the residual gas. The equilibrium distribution of ions over the radius in an RF-only quadrupole is given in [Koz99]:

$$n(r) = \frac{n_0}{\left(1 + \left(\frac{2m}{M}\right)\left(\frac{r}{r_0}\right)^2\right)^{\frac{2M}{m}}} \quad (1_{25})$$

where $n(r)$ and n_0 are the densities of the ions at distance r off the axis and on the axis of the RFQ respectively, r_0 is the radius of the RFQ, all other quantities are defined in Eq.(1_17).

1.3 Ion sources

In this subchapter three different types of ion sources are described. Each ion source is able to produce only certain ion species. Thus, the type of an ion source should be chosen according to the ion species required for the particular experiment or application.

1.3.1. Electrospray ion source

The production of ions by evaporation of charged droplets obtained through spraying or bubbling, has been known for about a century, but it was only fairly recently discovered that these ions may hold more than one charge[Gie84]. A model for ion formation in ESI (electrospray ion source), containing the commonly accepted themes, is described below [Fen93].

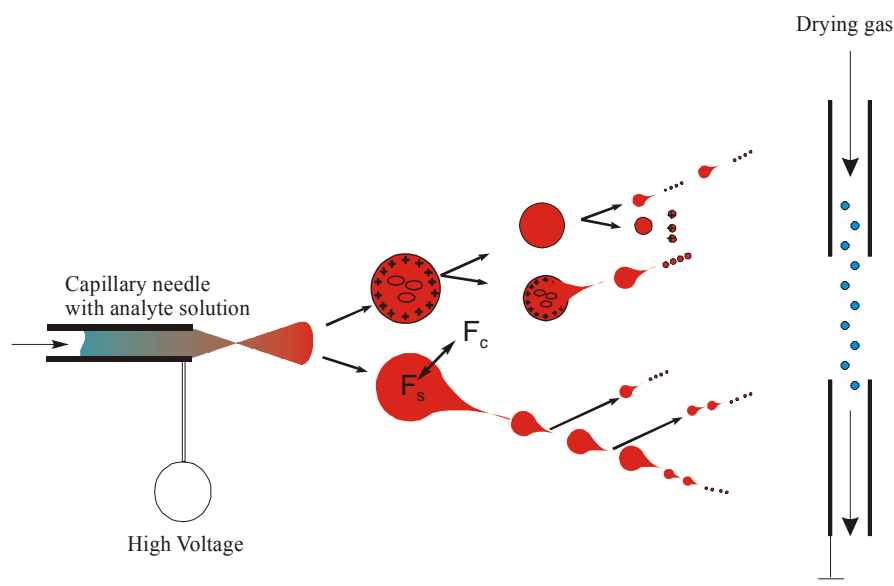


Fig.(1-7): A basic principle of an electrostatic ion source. Large charged droplets are produced by ‘pneumatic nebulization’; i.e. the forcing of the analyte solution through a needle, where a high voltage (usually about 3000 V) is applied. The polarity of the applied voltage depends on the sign of the ion charge. Due to the voltage the emerging solution is dispersed into a very fine spray of charged droplets all at the same polarity. The solvent evaporates away, shrinking the droplet size and increasing the charge concentration at the droplet’s surface. Eventually, at the Rayleigh limit [Ray82], Coulombic repulsion overcomes the droplet’s surface tension and the droplet explodes.

Large charged droplets are produced by ‘pneumatic nebulization’; i.e. the forcing of the analyte solution through a needle (see Fig.(1-7)), at the end of which is applied a high voltage (usually about 3000 V). The polarity of the applied voltage depends on the sign of the ion charge. Due to the voltage the emerging solution is dispersed into a very fine spray of charged droplets all at the same polarity. The solvent evaporates away, shrinking the droplet size and increasing the charge concentration at the droplet’s surface. Eventually, at the Rayleigh limit [Ray82], Coulombic repulsion overcomes the droplet’s surface tension and the droplet explodes.

The Rayleigh limit can be expressed as follows:

$$Q = 8\pi (\epsilon_0 \gamma R^3)^{\frac{1}{2}} \quad (1_{26})$$

where Q is the droplet charge, R is the droplet radius, ϵ_0 is the permittivity of vacuum, and γ is the surface tension of the solvent.

This 'Coulombic explosion' forms a series of smaller, lower charged droplets. The process of shrinking followed by explosion is repeated until individually charged 'naked' analyte ions are formed. The charges are statistically distributed among the analyte's available charge sites, leading to the possible formation of multiply charged ions under the correct conditions. Increasing the rate of solvent evaporation, by introducing a drying gas flow counter current to the sprayed ions (see Fig.(1-7)) increases the extent of multiple-charging. Decreasing the capillary diameter and lowering the analyte solution flow rate i.e. in nanospray ionization, will create ions with higher M/Q ratios (i.e. it is softer ionization technique) than those produced by 'conventional' ESI and are of much more use in the field of bioanalysis.

1.3.2 Alkali and Alkali Earths ion source

Heating a sample substance to a high temperature on a surface of a metal (a filament) by passing an electric current through the filament in vacuum causes positive ions and neutral species to desorb from its surface. Because of the high temperature involved, only certain elements are useful for construction of the filament. Typically platinum, rhenium, tungsten and tantalum are used because they are metallic and can be heated to temperatures of about 1000 to over 2000⁰ C without melting. A further important criterion for the filaments is that they should not readily react chemically with surrounding gas or with any sample placed on them. Since hot filaments are used in a high vacuum so as to facilitate evaporation and the manipulation of the emitted ions and neutrals, interaction of the filaments with air or background vapors is automatically reduced to a low level.

Samples examined by surface emission are almost always inorganic species because, at the high temperatures involved, any organic material is seriously degraded (thermolysed) and will react with the filaments. At temperatures of 1000 to 2000⁰ C, most inorganic substances yield positive ions without reacting with the typical filament elements listed below.

To obtain positive ions from a sample, it must come into contact with the filament. This may be done by directing a gas or vapor over the hot filament but, more usually, the sample is placed directly onto a cold filament, which is then inserted into the instrument and heated. A consequence of the high temperatures is that much of

the sample is simply evaporated without producing isolated positive ions. There is a ‘competition’ between formation of positive ions and the evaporation of neutral particles. Since only charged particles are of interest for TOF mass spectrometry, it is important for maximum sensitivity that the ratio of positive ions to neutrals should be as large as possible. Eq.(1_27) governing this ratio is given below[Val00]:

$$\frac{n^+}{n^0} = Ae^{(\varphi-I)/kT} \quad (1_27)$$

where n^+/n^0 is the ratio of the number of positive ions to the number of neutrals evaporated at the same time from a hot surface at temperature T , k is the Boltzman constant and A is another constant (often taken to be 0.5), the expression $\varphi-I$ is the difference between the ionization energy (I ; sometimes known as the ionization potential) of the element or neutral, from which the ions are formed and the work function (φ or sometimes W) of the metal from which the filament is made. The ionization energy and the work function control the energy needed to remove an electron from a neutral atom of the sample and the material from which the filament is constructed. The difference between I and φ governs the ease with which positive ions can be formed from sample molecules lying on the filament. Some typical values for ionization energies and work functions are give in Tables 1 and 2. By inserting a value for k and adjusting the Eq.(1_27) to common units (eV) and putting $A = 0.5$, the simpler Eq.(1_28) is obtained.

$$\frac{n^+}{n^0} = 0.5e^{11,6*10^3(\varphi-I)/T} \quad (1_28)$$

where T is in Kelvin degree, φ and I are in eV.

Examination of Eq.(1_28) reveals that, for $\varphi > I$, the expression $(\varphi - I)$ is positive, hence the greater the temperature, the smaller the proportion of positive ions to neutrals. For example, with a sample of caesium (ionization energy, 3.89 eV) on a tungsten filament (work function, 4.5 eV) at 1000 K, the ratio of $n^+/n^0 = 591$. Thus, for every caesium atom vaporized, some 600 atoms of Caesium-ions are produced. At 2000 K, the ratio n^+/n^0 becomes 17 and only about 20 ions of caesium are evaporated for every Cs-atom. Clearly, the lower the ionization energy with respect

to the work function, the greater the proportion of ions to neutrals produced. For this reason, filaments are used, for which their work functions give highest yields of ions.

Element	Ionization Energy (eV)
Aluminium	5.98
Calcium	6.11
Carbon	11.26
Caesium	3.89
Copper	7.72
Gold	9.22
Lanthanum	5.61
Lead	7.42
Lithium	5.39
Rubidium	4.18
Strontium	5.69
Thorium	6.95
Uranium	6.08

Table 1: A table of first ionization energies (eV) for some commonly examined elements

Element	Work function (eV)	Melting point (K)
Platinum	6.2	2028
Rhenium	4.8	3440
Tantalum	4.2	3120
Tungsten	4.5	3640

Table 2: Values of the average work function (eV) for the commonly used filament metals. The melting points of the metals are also shown to give some guidance as to the maximum temperature, at which they can be used

1.3.3 Laser ionization ion source

The laser ionization of the elements placed in the target of the ion source can occur resonantly and non-resonantly. In order that resonant ionization can take place the nuclide that is to be ionized must have an electromagnetic transition between two electron shells, the energy of which should coincide with the frequency of the laser radiation ($E_{\text{laser}} = h\nu$). Thus, resonant ionization is selective and applicable only to a few species. In the case of non-resonant ionization the laser beam hitting the target transfers the momentum to the target and, therefore, kinetic energy. As the result, the target gets heated and ionization of the target material occurs (laser ablation).

Chapter 2

Experimental set-up

The Ortho-TOF mass spectrometer

The design of the Ortho-TOF MS is based on a system developed by A. Dodonov et al. [Dod87,Dod94]. A detailed scheme of the Ortho-TOF MS is shown in Fig.(2-1). Ions produced in the ion source (1) enter a gas filled RF-only quadrupole (2) where they are cooled. After extraction out of the RF-only quadrupole, the cooled ions pass an einzel lens (7) and enter the modulator (10). In the modulator the ions are pushed by a pulsed electric field in the direction perpendicular to the initial beam direction and are accelerated in the accelerator (13). The time-of-flight of the ions from the modulator to the MCP-detector (21) is a measure for mass-to-charge ratio of the ions. Fig.(2-2) is a photo of the Ortho- TOF MS and electronics dedicated to it.

2.1 Ion source

Different ion sources were used in this work. The choice of the type of the ion source depended on the task that the author was going to carry out.

As it was already mentioned in chapter 1, three different types of ion sources can be used with the Ortho-TOF MS.

Schematic views of the ion sources are presented in Fig.(2-3(a,b,c)).

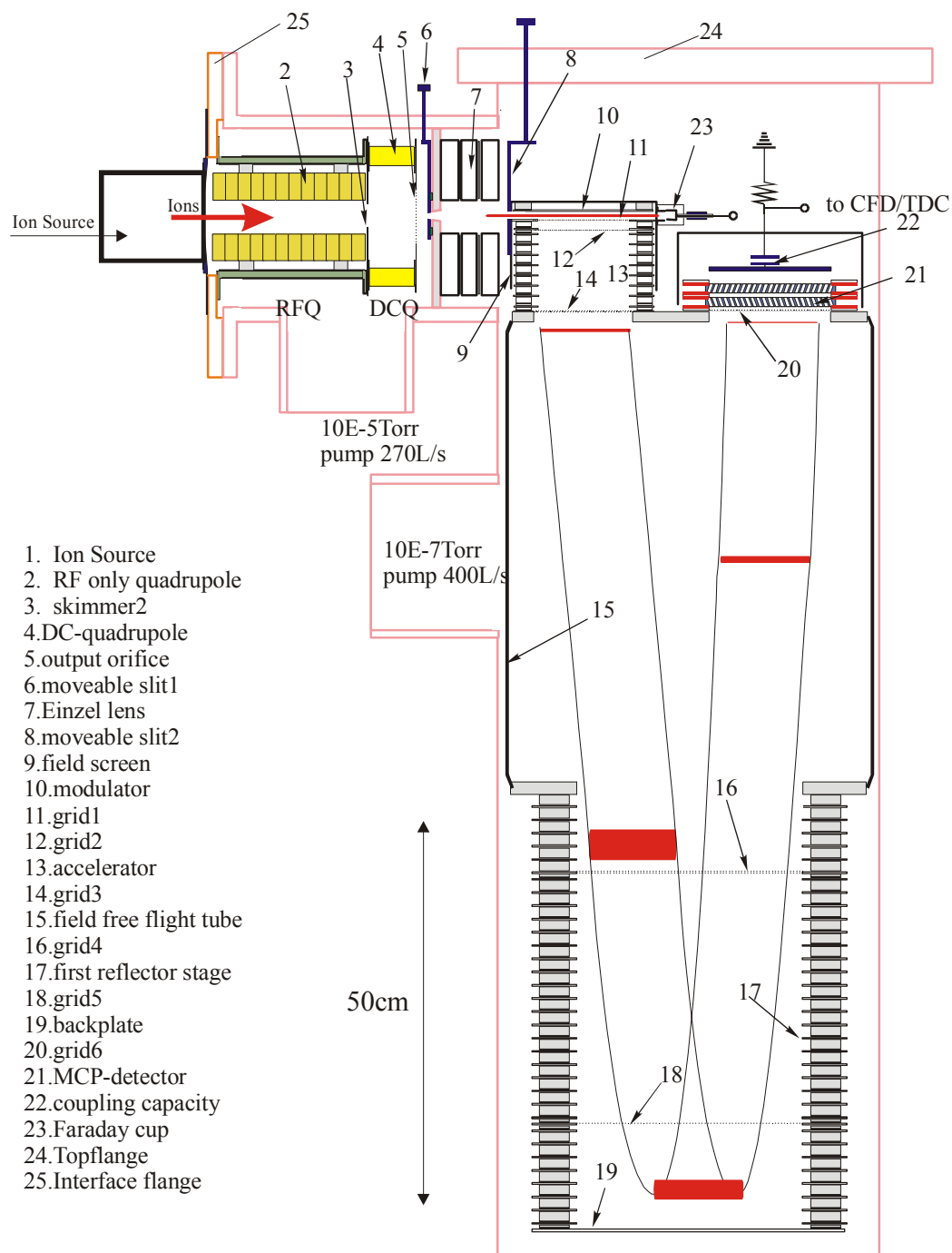


Fig.(2-1): Schematic view of the Ortho-TOF MS. Ions produced in the ion source (1) enter the gas filled RF-only quadrupole (2) where they get cooled. After extraction from the RF only quadrupole the cooled ions passing the einzel lens (7) enter the modulator (10). In the modulator the ions get repelled in the direction perpendicular to the initial beam direction and get accelerated in the accelerator (13). The time-of-flight of the ions from the modulator to the MCP-detector (21) is a measure for M/Q ratio of the ions.

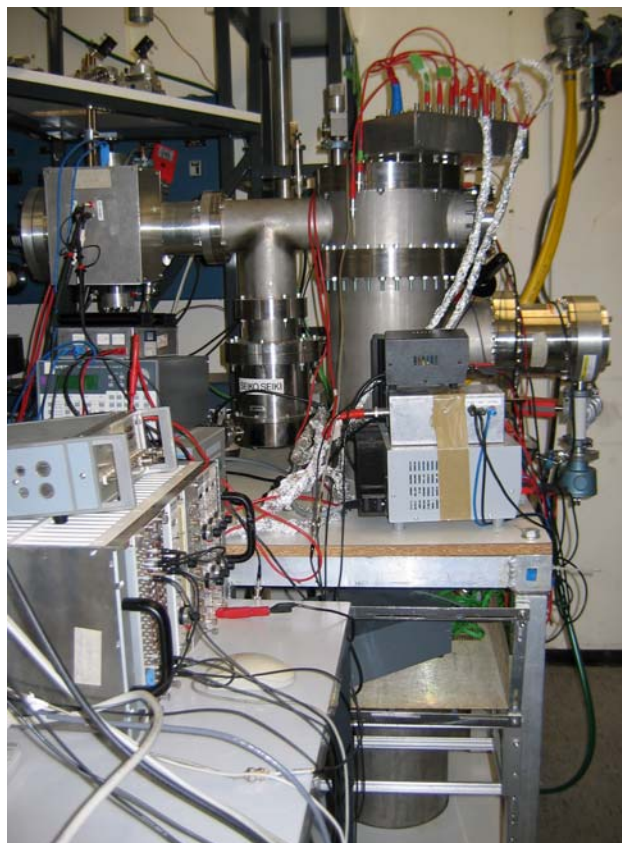


Fig.(2-2) : A photo of the Ortho-TOF MS and electronics dedicated to it.

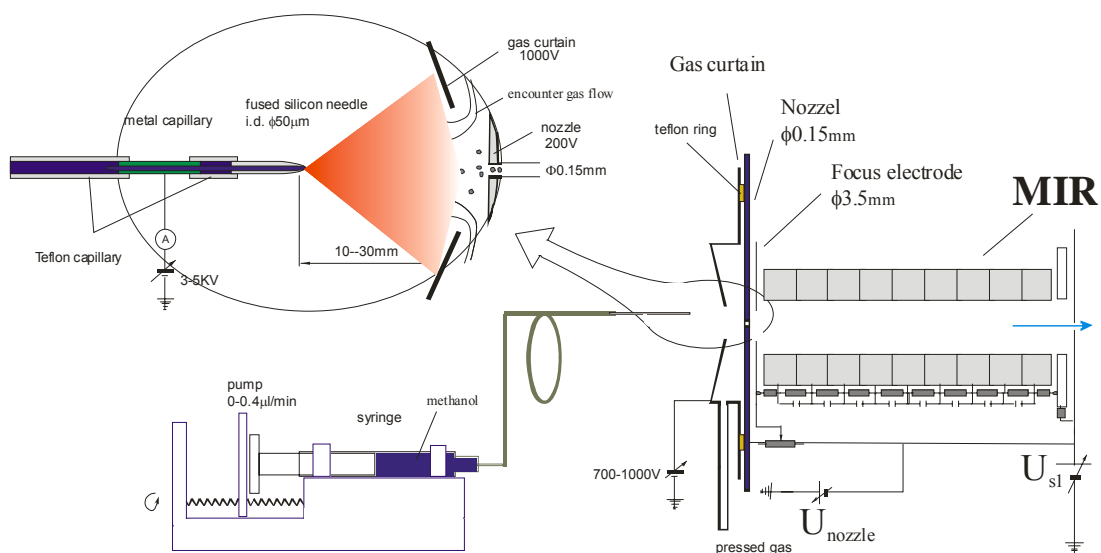


Fig.(2-3(a)): Schematic view of the electrospray ion source. It consists of a syringe pump with an infusion syringe, a teflon capillary that contains the sample, a stainless steel capillary, a connecting teflon capillary, a fused silicon spray needle, and a gas curtain. The sample (about 20 μl) is stored in the 20 cm long teflon capillary of 400 μm inner diameter. The sample is injected at a 0.1 ~ 0.4 $\mu\text{l}/\text{min}$ flow rate controlled by the syringe pump (KD Scientific 88, kdScientific Inc., USA), whose syringe is filled with methanol in advance.

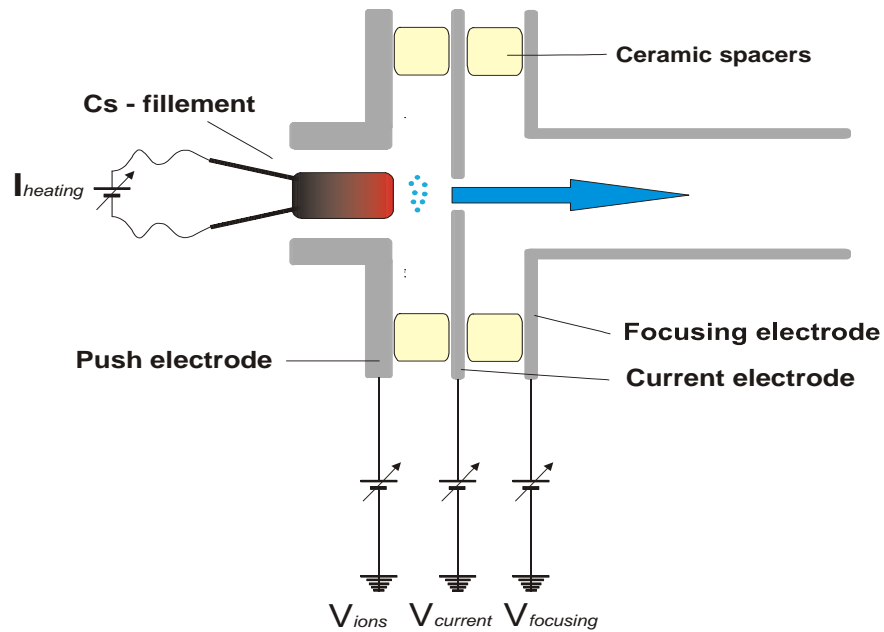


Fig.(2-3(b)): Schematic view of the Cs ion source. It consists of a filament and an electrode structure. The filament is a aluminosilicate sponge which contains Cs. The remarkable feature of such a sponge structure is its large effective surface. The larger the effective surface of the source is the higher the emitted Cs-Ion current of such a source is.

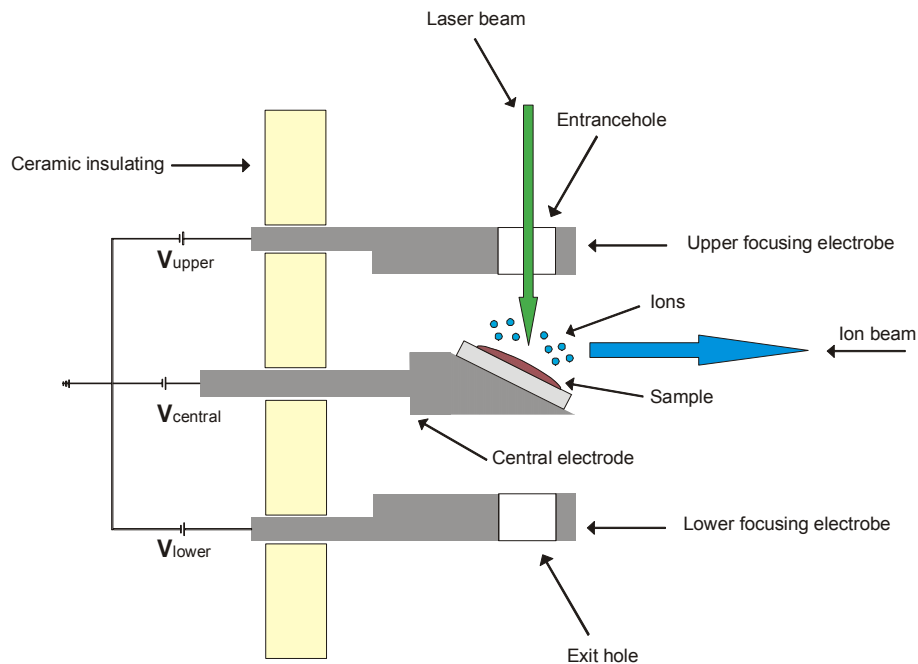


Fig.(2-3(c)): Schematic view of the Laser ion source. It consists of three electrodes: a central electrode, an upper electrode and a lower electrode. The central electrode serves as a holder for the target. Two holes are made in the upper and the lower electrodes and serve for guiding the laser beam from the laser onto the target. The target is placed on the central electrode. The central electrode is moveable, so the position of the target can be adjusted to the laser beam.

1. Electrospray ion source

The electrospray ion source (see Fig.(2-3(a))) consists of a syringe pump with an infusion syringe, a teflon capillary that contains the sample, a stainless steel capillary, a connecting teflon capillary, a fused silicon spray needle, and a gas curtain. The sample (about 20 μ l) is stored in the 20 cm long teflon capillary of 400 μ m inner diameter. The sample is injected at a flow rate of 0.1 ~ 0.4 μ l/min, which is controlled by the syringe pump (KD Scientific 88, kdScientific Inc., USA), whose syringe is filled with methanol in advance. A fully filled sample capillary can sustain the spray for about half an hour. A voltage of about +3500 V (for positive ions) is applied to the sample through the stainless steel capillary, which is connected to the spray needle by a short teflon capillary. The spray needle typically is of 100 μ m outer and 50 μ m inner diameter and located 1 ~ 3 cm from a counter electrode (gas curtain, in Fig.(2-3(a))). Supposing that the counter electrode is large and planar, the electrical field at the capillary tip can be calculated using the approximate relationship [Pfe68]:

$$E_c = \frac{4V_c}{r_c \ln\left(\frac{8d}{r_c}\right)} \quad (2_1)$$

where V_c is the voltage drop between the needle and the gas curtain electrode, r_c is the outer radius of the tip of the capillary, and d is the distance from the capillary tip to the counter electrode. According to Eq.(2_1), E_c is proportional to V_c , inversely proportional to r_c , and decreases slowly with the electrode separation d due to the logarithmic dependence. Because it is easy to reduce the value of r_c in order to obtain a higher electrical field E in the region at the tip of the spray needle, the needle tip should be prepared as a small cone.

The electrospray ion source is operated at a pressure of one atmosphere. The ions extracted out of the syringe move through a dry nitrogen counter flow and pass through a nozzle into the first gas-filled RF-quadrupole, i.e. molecule-ion reactor (MIR). As a part of electrospray ion source the MIR serves as (1) an interface between the 1 atmosphere and the second RF-only quadrupole in which a typical pressure is $5 \cdot 10^{-3}$ mbar, (2) a device that reduces the emittance of the beam coming into the MIR to the proper value needed in order to be accepted by the second RF-

only quadrupole, and (3) A device that removes adducts or moreover molecule ion decomposition by varying the strength of the electrical field applied along the MIR.

From the principle of operation of electrospray it is seen that the samples that one wants to investigate must be prepared in liquid form. This technique is widely used in biochemistry and medicine in order to deliver organic samples to a TOF MS. Usually such organic samples (gramicidin, insulin- β chain, fibrinopeptide- β) are dissolved in the methanol or acetonitrile. In many cases 2% acetic acid is added for better spray condition. In order to generate light ions, salts like NaCl, KCl, CsI, PbI_2 can be used. The typical concentration of the samples is about 10^{-5} M.

2. Cs-ion source

The Cs-ion source, built by the author (see Fig.(2-3(b))), consists of a filament and an electrode structure. The filament is a aluminosilicate sponge which contains Cs. The remarkable feature of such a sponge structure is its large effective surface. As was described in the previous chapter the larger the effective surface of the source is the higher the emitted Cs-ion current of such a source. In this work a commercial aluminosilicate Cs-filament (TB-118, HeatWave Labs Inc, USA) was used. The push electrode serves to convey kinetic energy to the ions. The current electrode is used for measuring the emission current of the filament. It can also be used as a shutter electrode if one wants to bunch the ion current. The focusing electrode is used for varying the focusing condition of the ion source. The measured dependence of the ion source current on the heating current of the filament is presented in Fig.(2-4). The measurement of the ion source current was carried out with a faraday cup (see cut-in in Fig.(2-4)). The measured curve is reproducible with a precision of about 5%.

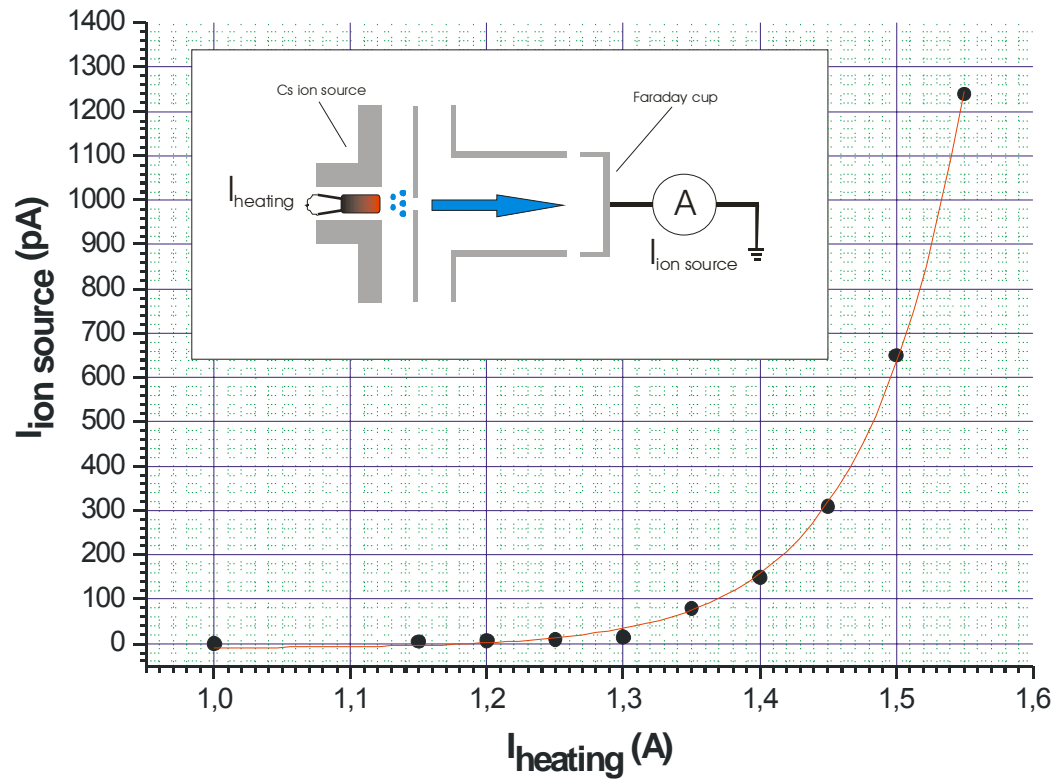


Fig.(2-4): Measured Cs-ion current vs heating current of the Cs-ion source. The measurement of the ion source current was carried out with a faraday cup (see in-set in Fig.(2-4)). The measured curve is reproducible with a precision of about 5%.

3. Laser ion source

The laser ion source used in the present work was designed and built by Z.Wang. Since the laser source is a subject of his PhD-work, here only a brief description of this source is presented.

The laser ion source (see Fig.(2-3(c))) consists of three electrodes: a central electrode, an upper electrode and a lower electrode. The central electrode serves as a holder for the target. Two holes are made in the upper and the lower electrodes and serve to guide the laser beam from the laser (Nd:YAG Laser, $\lambda=532$ nm, pulsed (10;20;50Hz), energy 300 mJ, pulselength 8 ns) onto the target. The target is placed on the central electrode. The central electrode is moveable, so the position of the target can be adjusted to the laser beam. The target is manufactured from the samples of interest as a solid tablet. Thus, the great advantage of such a source is its ability to produce positive ions of any nuclide that can be prepared as a solid state tablet. One

of its disadvantages is that the laser power is temporally unstable. In this work the following samples were used: metallic Pb, metallic Sn, CsI, C₆₀ and a mixture of PbF₂, CsI, NaCl, Sn and KCl.

Table 3 presented below summarizes the advantages and the disadvantages of all three sources and gives the notes where each source was used.

	electrospray	Cs-ion source	Laser ion source
advantage	1.The ions of interest can be introduced in the Ortho-TOF MS directly from atmosphere. 2. The source is cheap.	1. The ion current is well defined by the heating current and can be regulated from 0A up to several μ A. 2. The source is cheap.	1. Large variety of ions can be produced in such a source.
disadvantage	1. The ion current can not be regulated and is unstable with time. 2. Only substances that are soluble in water can be investigated.	1. The application of such a source is limited by Alkali an Alkali Earths elements.	1. The ion current is strongly unstable due to the instability of the laser power in the particular case of the laser used . 2. The source is very expensive.
application	Investigation of biomolecules like proteins, peptides, etc	A variety of applications that require an ion beam with well defined parameters.(efficiency measurements, buncher-cooler characterization).	Applications that require many different ions. TOF-MS accuracy measurement, absolute mass calibration of the TOF MS).

Table 3 : Comparison of three ion sources used in this work. The advantages and the disadvantages of all three sources are summarized and the notes where each source was used are given. The electrospray ion source and Cs-ion source were built by the author, the laser ion source was built by Z. Wang.

2.2 Quadrupole

The RF quadrupole plays the two following roles in the Ortho-TOF MS: (1) It serves as an interface stage between the ion source and the Ortho-TOF MS in order to match the pressure in the ion source and in the Ortho-TOF MS. (2) It serves as an ion cooler/buncher, which reduces the phase space of the ion beam.

In the present work two different type of quadrupoles were used: a segmented quadrupole and a quadrupole with LINAC geometry (PE SCIEX's patent).

A photo of the RFQ assembly mounted on a flange is shown in Fig.(2-5).

A schematic view of both quadrupoles is shown in Fig.(2-6(a,b)), and electrical diagrams are shown in Fig.(2-7(a,b)).



Fig.(2-5): A photo of the RFQ assembly mounted on a flange. The red box is a PIRANI-gauge. On the front side of the flange a gas inlet is mounted. Two feedthroughs are needed for DC and RF power supply.

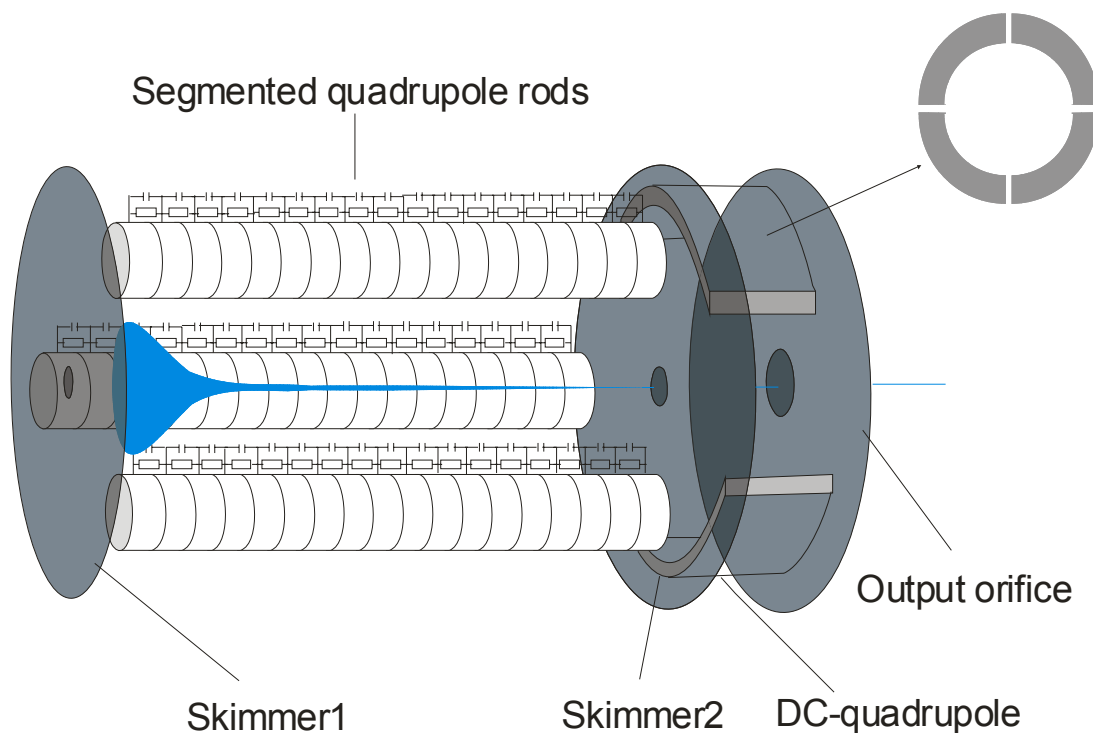


Fig.(2-6(a)): Schematic view of the segmented quadrupole. In order to form a uniform electrical field along the quadrupole, 29 pieces of stainless steel rings are used for each rod of the quadrupole. The adjacent rings are insulated by a 0.125 mm thick kapton foil and electrically connected by 640Ω resistors and capacities of 10 nF. This resistor chain forms a voltage divider, thus the voltage applied between the beginning and the end of each rod is homogeneously distributed over the rod, creating a uniform electrical field along the axis of the quadrupole.

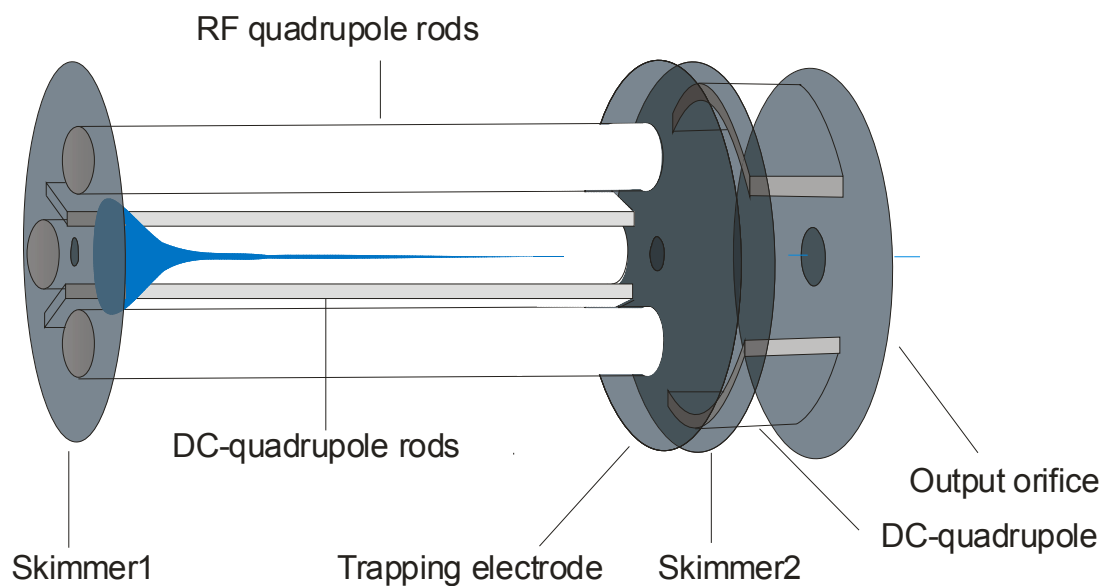


Fig.(2-6(b)): Schematic view of the LINAC quadrupole (PE SCIEX's patent). Four additional tilted rectangular rods are used to form a uniform electrical field along the axis of the quadrupole.

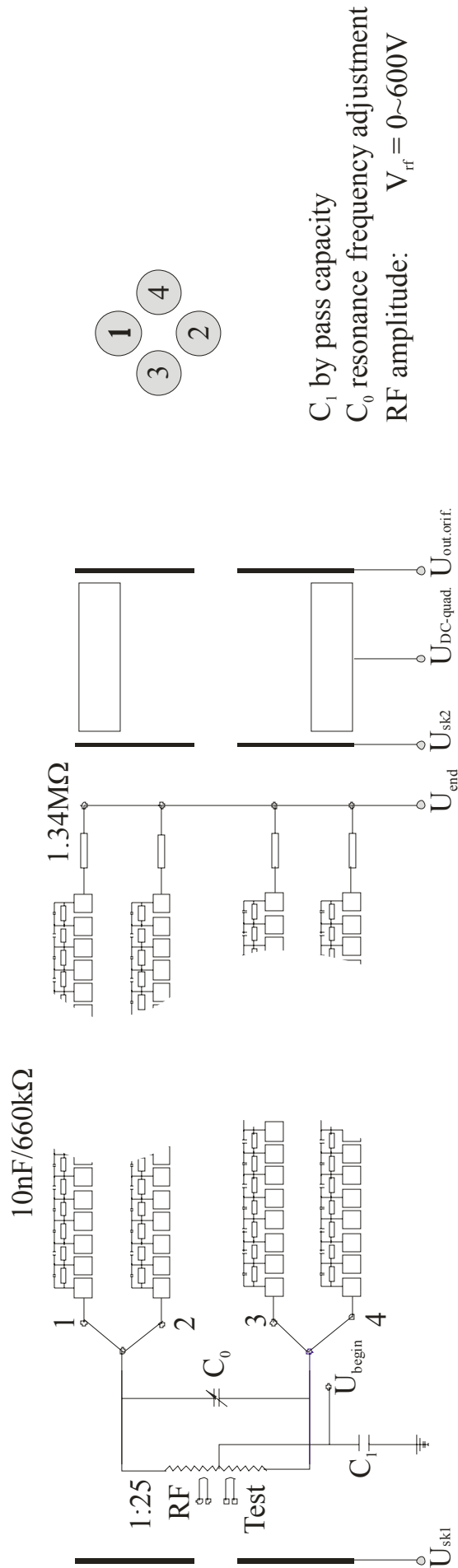


Fig.(2-7(a)): Electrical diagram of the segmented quadrupole. In order to form a uniform electrical field along the quadrupole, 29 pieces of stainless steel rings are used for each rod of the quadrupole. The adjacent rings are insulated by a 0.125 mm thick kapton foil and electrically connected by 640Ω resistors and capacities of 10 nF. This resistor chain forms a voltage divider, thus the voltage applied between the beginning and the end of each rod is homogeneously distributed over the rod, creating a uniform electrical field along the axis of the quadrupole.

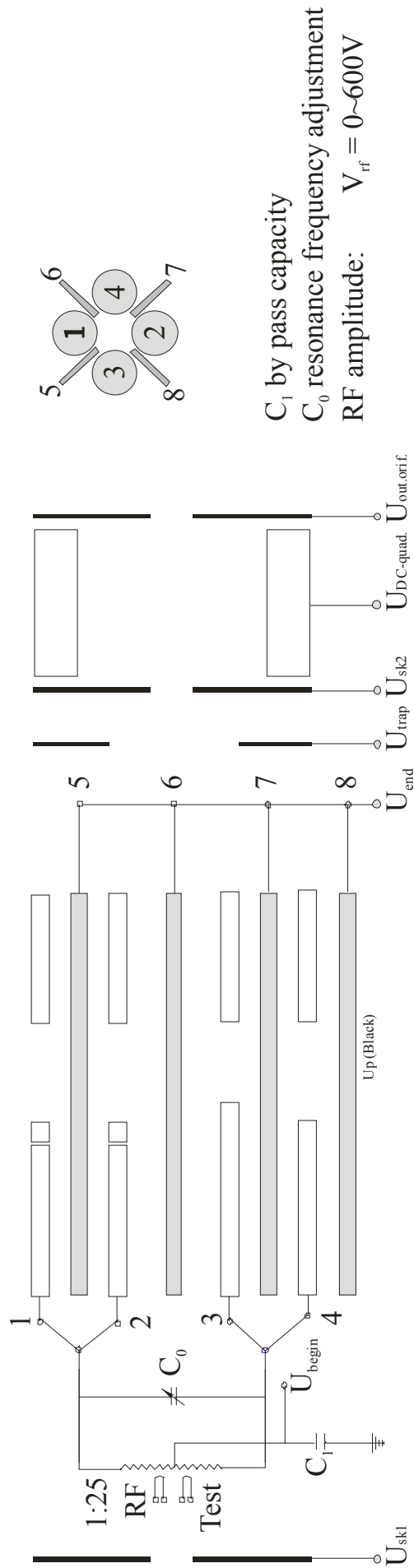


Fig.(2-7(b)): Electrical diagram of the LINAC quadrupole. In order to form a uniform electrical field along the quadrupole, four tilted rectangular stainless steel rods are used in addition to the round ones. Otherwise, the electrical diagram of the LINAC quadrupole is similar to the segmented one (see Fig.(2-7(a))).

The segmented and the LINAC quadrupoles have different longitudinal electrical fields, which serve to drag the ions through the quadrupole. In the case of the segmented quadrupole, in order to form a uniform electrical field, 29 pieces of stainless steel rings are used for each rod of the quadrupole. The adjacent rings are insulated by a 0.125 mm thick kapton foil and electrically connected by 640 Ω resistors and capacities of 10 nF. This resistor chain forms a voltage divider, thus the voltage ($\sim 1V$) applied between the beginning and the end of each rod is homogeneously distributed over the rod, creating an approximately uniform electrical field along the axis of the quadrupole.

In case of the LINAC quadrupole four additional tilted rectangular rods are used to form an approximately uniform electrical field along the axis of the quadrupole. Otherwise, these two quadrupoles are identical. More detailed information about mechanical and electrical realizations of the quadrupoles can be found in work [Zhe00].

2.3 Einzel lens

In Fig.(2-8) the time-of-flight analyzer(1) including the einzel lens(2) is shown

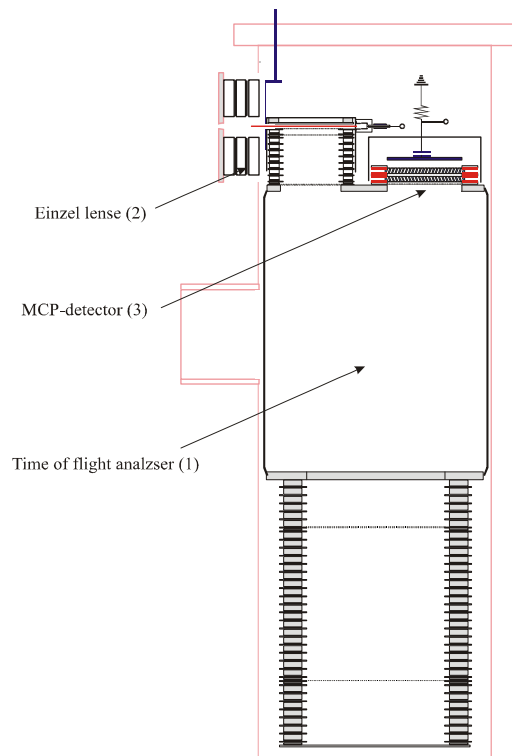


Fig.(2-8): Schematic view of the time-of-flight analyzer including an einzel lens and a MCP-detector. The einzel lens is placed on the beam trajectory between the quadrupole and the entrance of the accelerator. Like the quadrupole the einzel lens serves as a device that prepares the beam for the further stage.

The einzel lens is placed between the quadrupole and the entrance of the accelerator (see Fig.(2-1) and Fig.(2-8)). The einzel lens serves as a device that converts the angular divergence of the beam into the spatial spread of the beam. A schematic view of the lens is shown in the Fig.(2-9(a)), the electrical diagram is presented in Fig.(2-9(b)).

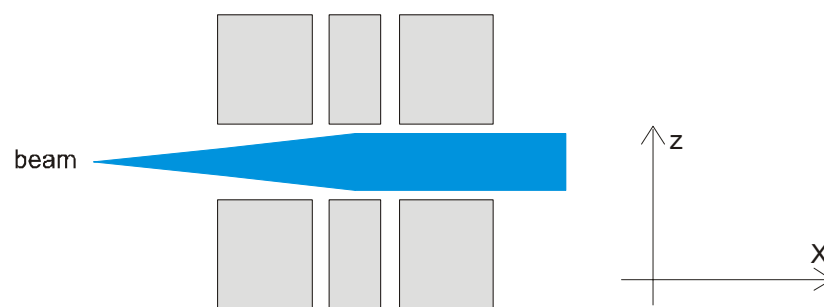


Fig.(2-9(a)): Schematic view of the einzel lens and its action on a beam

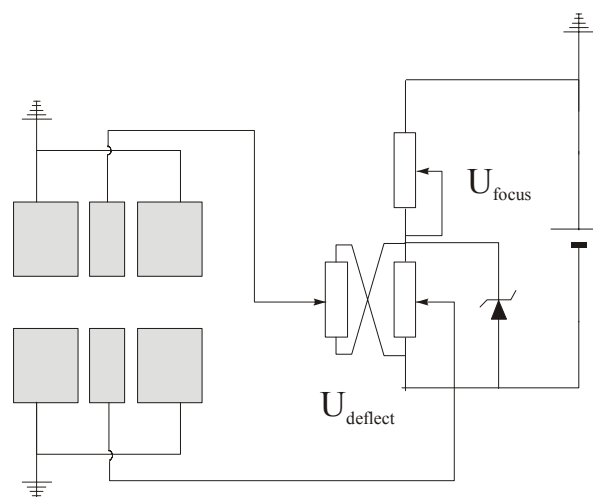


Fig.(2-9(b)): Electrical diagram of the einzel lens. Two potentials (U_{focus} and $U_{deflect}$) are applied to the einzel lens. Thus, the einzel lens can focus as well as deflect a beam.

The velocity spread (Δv_z) and the spatial spread in z -direction (Δz) (see Fig.(1-3)) are the main factors that affect the mass resolving power of the Ortho-TOF MS. According to the Liouville theorem the phase space volume of the beam before and behind the einzel lens is the same. A spatial spread of the ions in the modulator can be compensated by the reflector, whereas a velocity spread can not be compensated (see Appendix 1). Thus, the einzel lens is intended to widen the beam in the modulator in order to reduce the velocity spread in z -direction (see Fig.(2-9(a))) and therefore also the turn-around time. Since an ideal mechanical alignment can never be achieved, the einzel lens is segmented in order to be able to adjust the direction of the beam, in addition to its focusing property.

2.4 The time-of-flight analyzer

The time-of-flight analyzer (see Fig.(2-8)) can be functionally divided into three parts: modulator-accelerator, drift region and reflector.

The basic principles of functioning of such TOF mass spectrometers are done in subchapter 1.1 of chapter 1. Here is shortly considered only the technical realization of the time-of-flight analyzer. A more detailed description of the time of flight analyzer can be found in work [Zhe00]

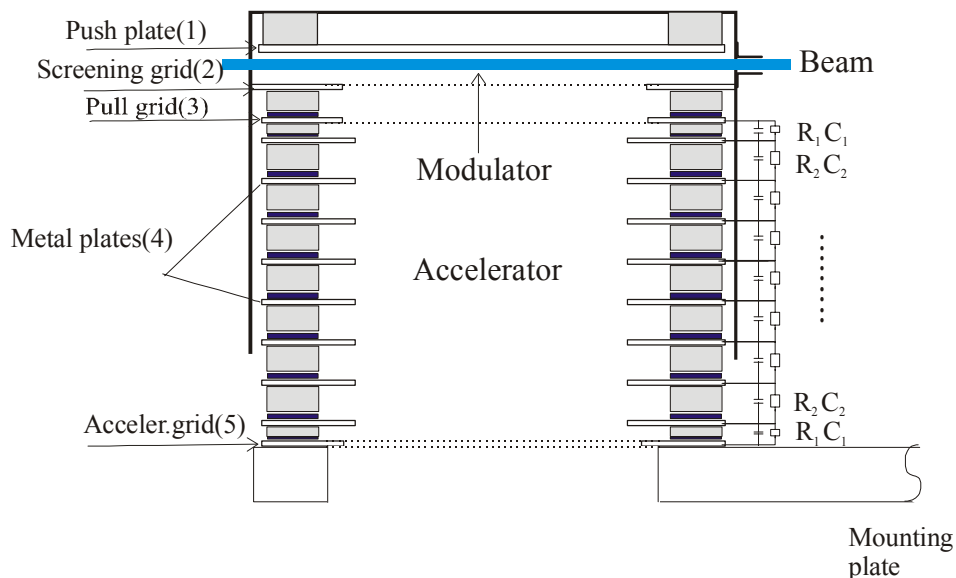


Fig.(2-10): Schematic view of the modulator-accelerator[Zhe00]. The modulator is a region between the push plate (1) and screening grid (2). The accelerator is a region between the pull grid (3) and the accelerating grid (5). The set of metal plates forms a uniform electrical field (4). The working cycle of the modulator-accelerator consists of two phases: Collecting the ions in the modulator and extraction of the ions out of the modulator through the accelerator into the drift region by applying short pulses of a voltage to the push plate and the pull grid.

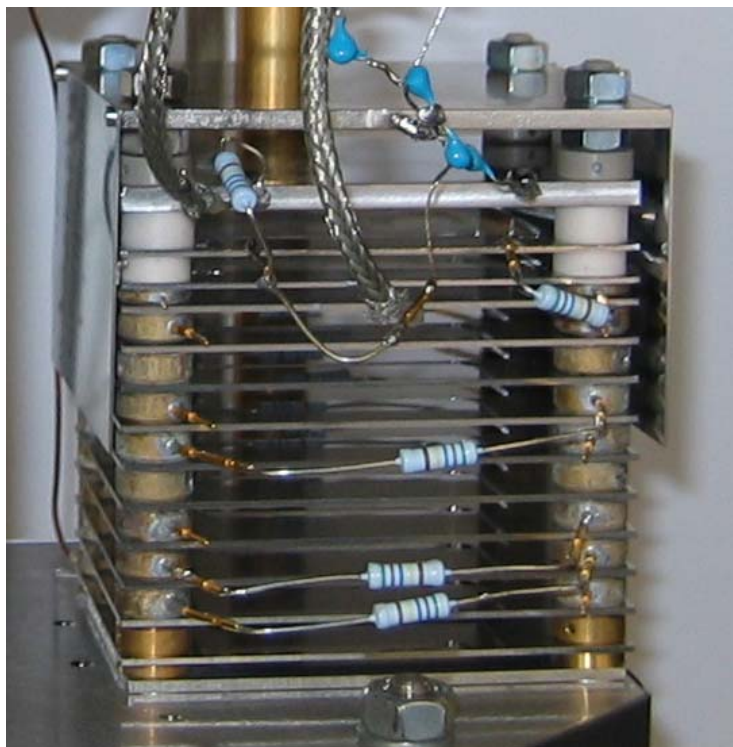


Fig.(2-11): A photo of the modulator.

The ion beam coming from the quadrupole and passing the einzel lens enters the modulator (see Fig.(2-10) (schematic view of the modulator) and Fig.(2-11) (photo of the modulator)). The modulator is a region between the push plate (1) and screening grid (2). The accelerator is a region between the pull grid (3) and the accelerating grid (5). The set of metal plates forms a uniform electrical field (4). The working cycle of the modulator-accelerator consists of two phases: Collection of the ions in the modulator and extraction of the ions out of the modulator through the accelerator into the drift region by applying short pulses of a voltage to the push plate and the pull grid.

During the next phase of ion collection, the new ions fill the modulator and simultaneously the bunch of ions originating from the previous collection phase passes the drift region, enters the reflector, gets reflected and hits the MCP-detector. The drift region is held at an electric potential of -6000V . It is protected against field penetration from outside by a metal screen. The potentials of about -300 V and $+1200\text{ V}$ are applied to the second grid and back plate respectively. A table with typical values of geometrical parameters of the TOF-analyzer and the potentials applied to the Ortho-TOF MS is presented in Appendix 5.

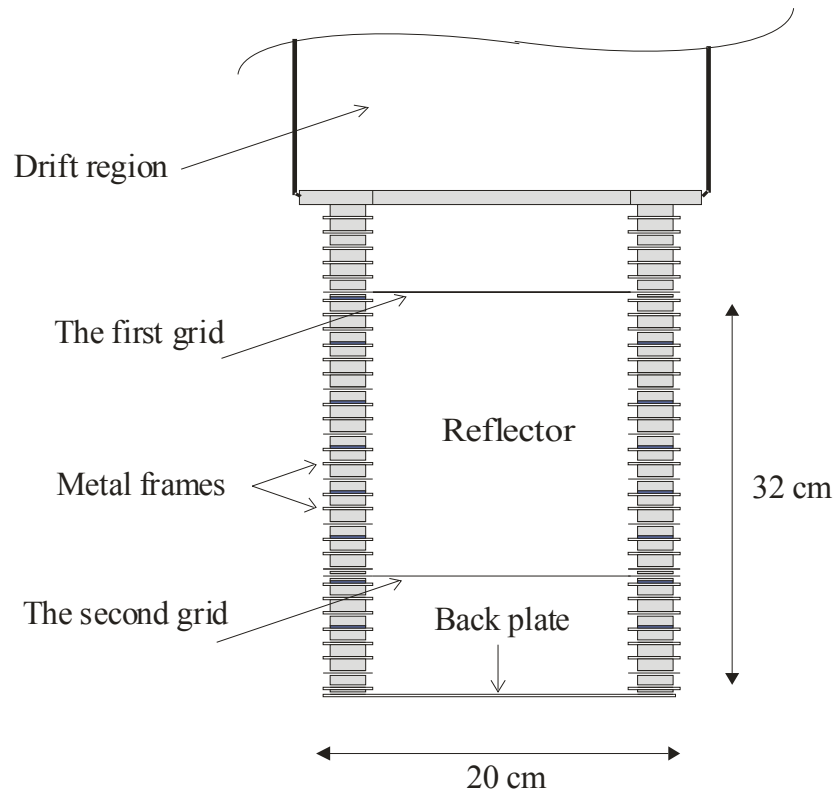


Fig.(2-12): The reflector of the time-of-flight analyzer. The homogeneous electrical fields in the reflector, similarly as in the modulator-accelerator, are created by the set of metal frames, the first grid at the entrance of the drift region, the second grid and the back plate. The first grid screens the reflecting region from the field free drift region. The second grid divides the reflector into two regions with different field strengths.

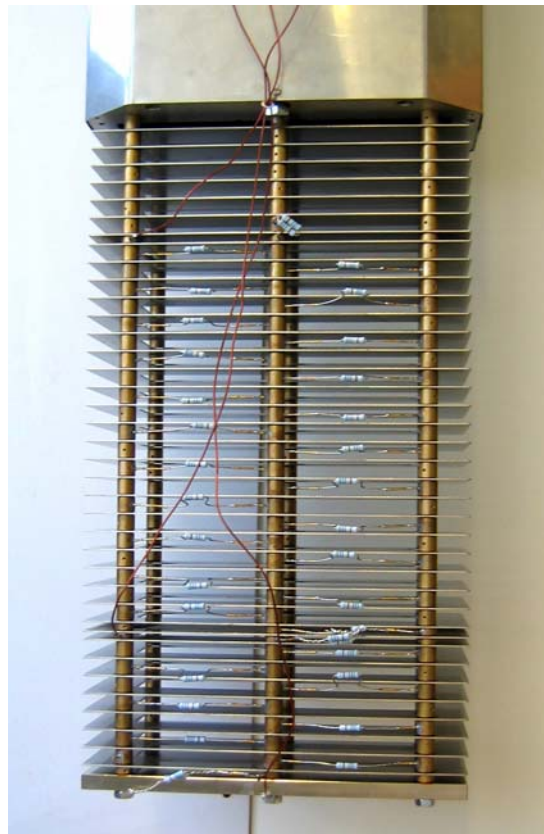


Fig.(2-13): A photo of the reflector.

The homogeneous electrical fields in the reflector, similarly as in the modulator-accelerator, are created in a set of metal frames. There are a first grid at the entrance of the drift region and a second grid in the reflector (see Fig.(2-12) (schematic view of the reflector) and Fig.(2-13) (photo of the reflector)). The first grid screens the reflection region from the field free drift region. The second grid divides the reflector into two regions with different electric field strengths.

2.5 Detection system

The detection system consists of a detector and a data-acquisition system.

As a charged particle detector a chevron-type microchannel plate (MCP) detector is used. A schematic view of the MCP-detector and the electrical diagram is presented in Fig.(2-14). Fig.(2-15) is a photo of the MCP-detector. The position of the MCP-detector in the Ortho-TOF MS is shown in Fig.(2-8).

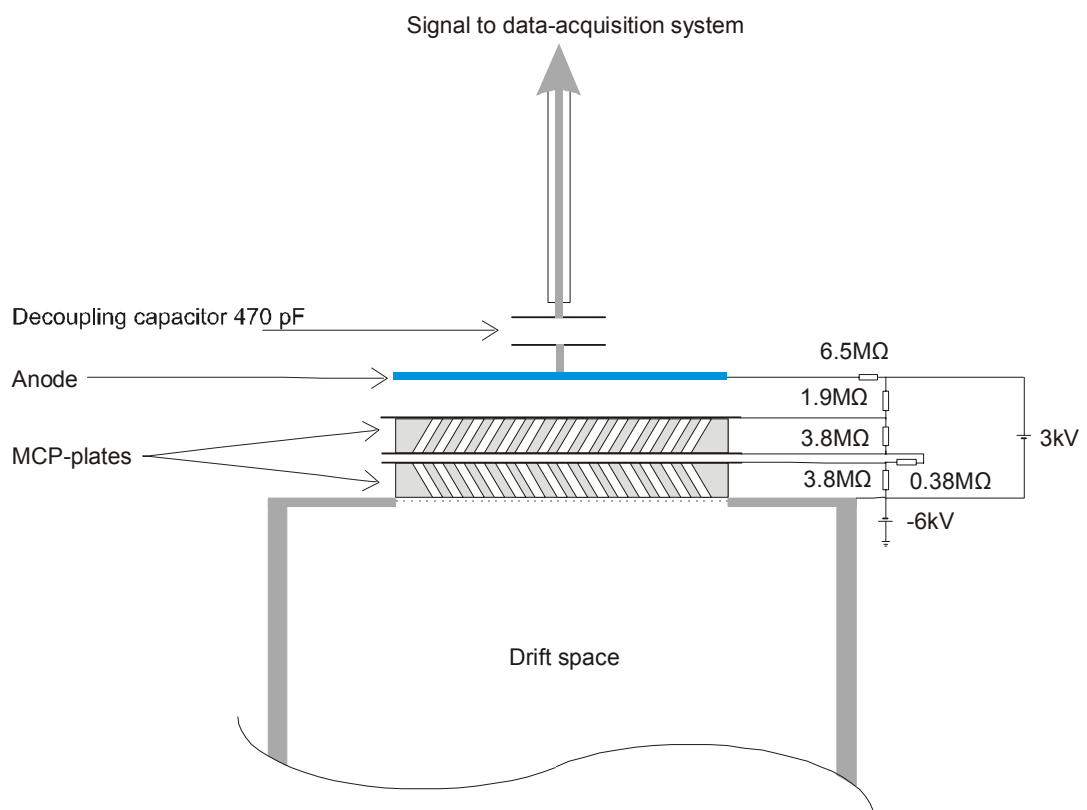


Fig.(2-14): MCP-detector, operated in a high voltage anode configuration. In the MCP-detector two large micro channel plates (MCP) are used. The active area of each MCP is $60 \times 40 \text{ mm}^2$, channel diameter of $12 \mu\text{m}$, and bias angle of 8° . The voltages are applied to each MCP through a resistor divider. Since the MCP-detector is operated in a high voltage anode configuration, a decoupling capacitor between the anode and the input of the data-acquisition system has to be used.

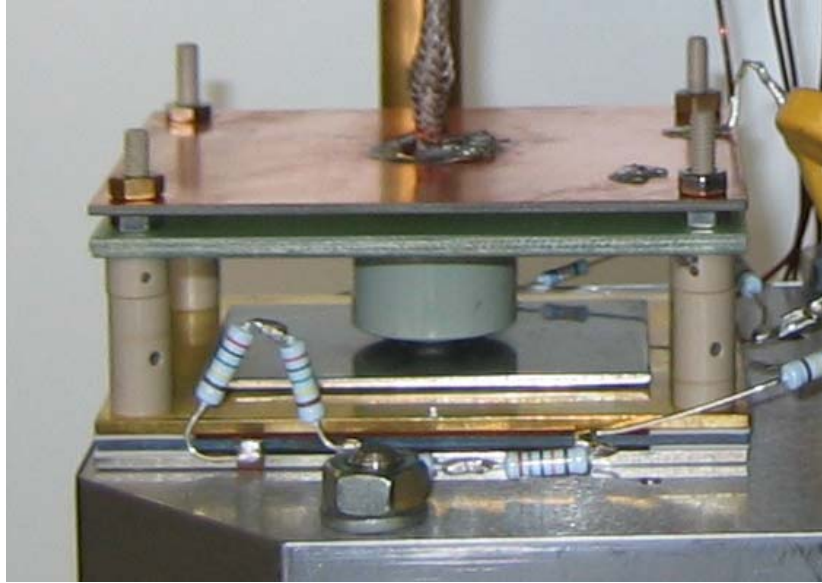


Fig.(2-15): A photo of the MCP-detector used in the Ortho-TOF MS

In the MCP-detector two large micro channel plates (MCP) are used. The active area of each MCP is $60 \times 40 \text{ mm}^2$, the channel diameter is $12 \mu\text{m}$, and the bias angle is 8° . The voltages are applied to each MCP through a resistor divider. Since the MCP-detector is operated in a high voltage anode configuration, a decoupling capacitor between the anode and the input of the data-acquisition system has to be used.

In Table 4 the efficiency of a MCP as a function of the energy of incident ions is listed [Pro00].

	Energy	Efficiency
ions	500eV ... 3keV	5% ... 40%
	3keV ... 10keV	40% ... 70%
	10keV ... 50keV	70% ... 80% ... 70%
	50keV ... 200keV	70% ... 40%

Table 4: Efficiency of the a MCP vs. the energy of incident ion [Pro00]

The amplification of the MCP-detector is about 10^7 [Pro00].

Taking into account that the input impedance of the data-acquisition system is 50Ω one can estimate the average amplitude of the signal at the input of the data-acquisition system.

$$V_0 = R \frac{Q}{\tau} \quad (2_2)$$

Where Q is the charge at the anode, caused by one charged particle hitting the MCP-detector, τ is the typical time-width of the charge signal at the anode, R is the input impedance of the data-acquisition system.

Substituting typical values of $R = 50 \Omega$, $\tau = 1\text{ns}$, $Q = 5 \cdot 10^{-13}$ As values into Eq.(2_2) one receives $V_0 = 80 \text{ mV}$. Therefore, a preamplifier is required in order to amplify the signal from a MCP-detector to the voltage level necessary for a data-acquisition system.

Three different types of time-digital converters (TDC) are used in the data-acquisition system in this work:

The Time-Digital Converter (TDC) (IONWERKS, Houston, USA)

The Picosecond Time Analyzer 9308(PTA) (ORTEC, USA)

The Time-Digital Converter 9353(TDC) (ORTEC, USA)

The configuration of the data-acquisition system is shown in Fig.(2-16). The configuration is typical for time-of-flight applications. A pulse generator (National Instrument delay generator computer built-in card) generates a start NIM-signal for the TDC. As a stop signal the ion arrival signal from the MCP-detector is used. A preamplifier is needed to amplify the signal from the MCP-detector for the next stage. A constant fraction discriminator (CFD) should be used as an intermediate stage before the TDC. It is defined by the following:

The amplitudes of the signals from the MCP-detector are not constant, after the pre-amplification they range from several 100 mV up to 2V. In order to receive a high resolving power of the Ortho-TOF MS an amplitude-insensitive converting device such as a CFD should be used.

In this work a CFD 935 from ORTEC is used. Table 5 lists the main properties of the TDCs.

Type of the TDC	Time-resolution	Dead time
TDC from IONWERKS	0.625 ns	20 ns
PTA 9308 from ORTEC	Down to 1 ps	50 ns
TDC 9353 from ORTEC	Down to 100 ps	1 ns

Table 5: The main properties of the TDCs used in the present work

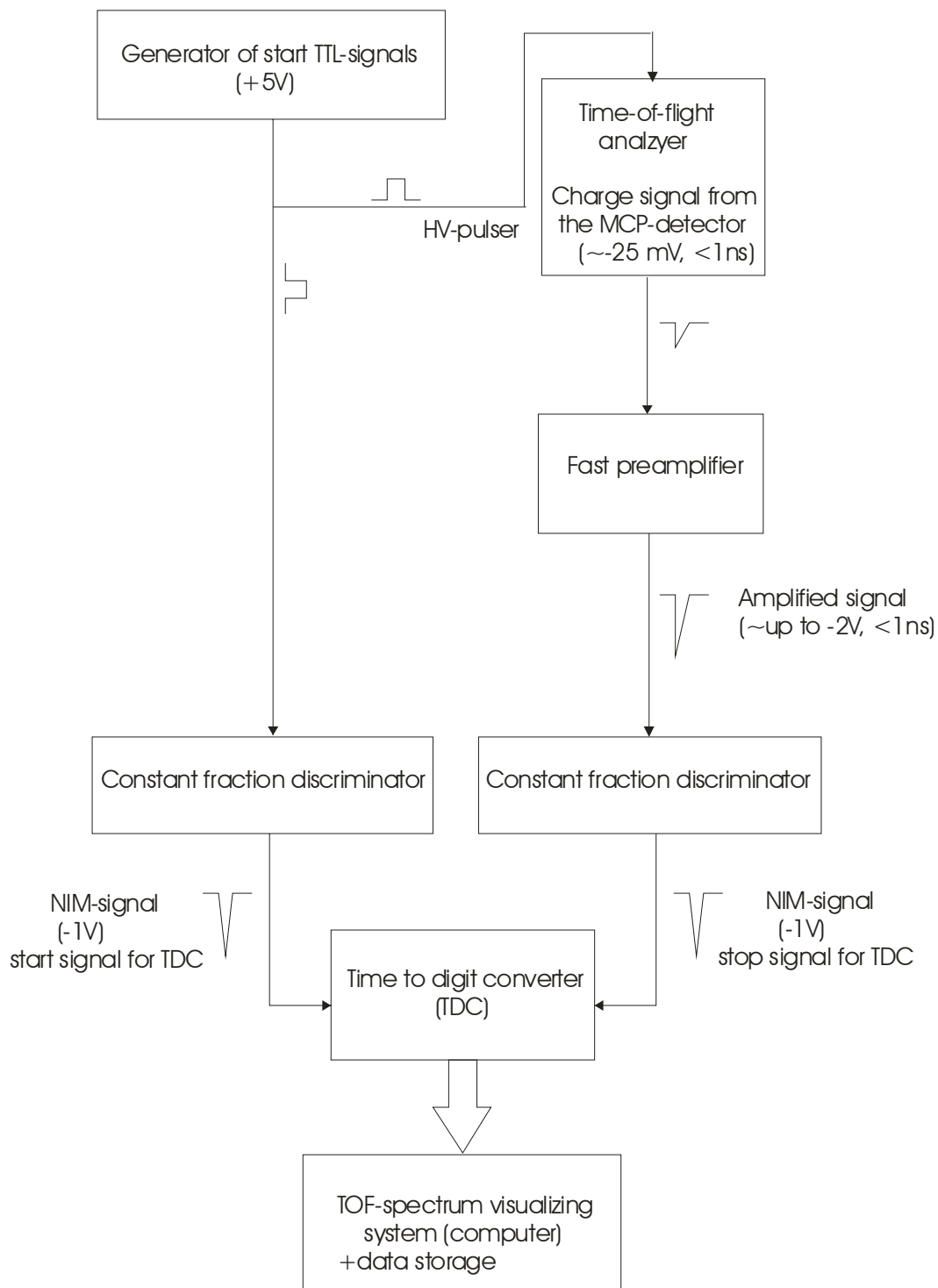


Fig.(2-16): A schematic view of the configuration of the data-acquisition system. The configuration of data-acquisition system is typical for time-of-flight applications. A pulse generator (National Instrument delay generator computer built-in card) generates a start NIM-signal for the TDC. As a stop signal a signal from the MCP-detector is used. A preamplifier is needed to amplify the signal from the MCP-detector for the next stage. A constant fraction discriminator (CFD) is used before the TDC in order to decrease the time jitter of the MCP signal.

The PTA 9308 from ORTEC has the largest dead time and the highest time resolution. So it is used at very low signal count rate of the MCP-detector. Due to the very high time resolution, the PTA 9308 is best suited for the applications where a high accuracy of mass determination is crucial. (Precision of determination of the peak center of gravity depends on the number of time-bins in the mass peak).

The TDC 9353 from ORTEC has the shortest dead time and a time resolution which is sufficient for many applications. So it is used at high signal count rate of the MCP-detector when it is necessary to have a maximal efficiency of the Ortho-TOF MS.

The TDC from IONWERKS was the first TDC used in this work. Now it is used as a spare system for the other two TDCs.

2.6 Vacuum system

The vacuum system of the Ortho-TOF MS is double-staged or three-staged according to the ion source used. When the electrospray ion source is used the vacuum system is three-staged. Otherwise, it is double-staged. The schematic view of the vacuum system is presented in Fig.(2-17(a,b)).

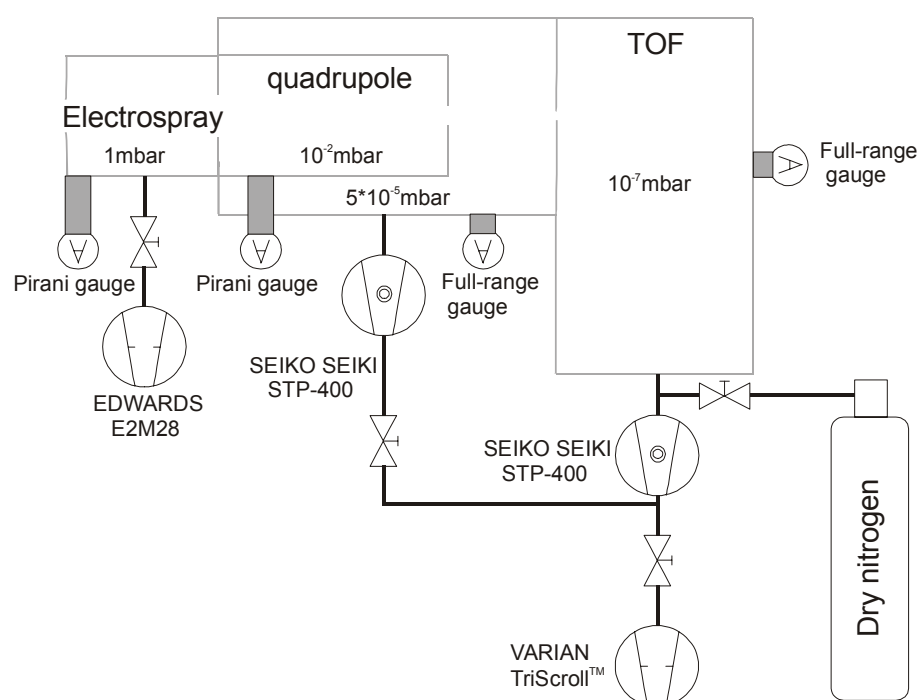


Fig.(2-17(a)): The vacuum system with electrospray ion source. It has three stages of differential pumping in order to maintain the needed pressure in the Ortho-TOF MS.

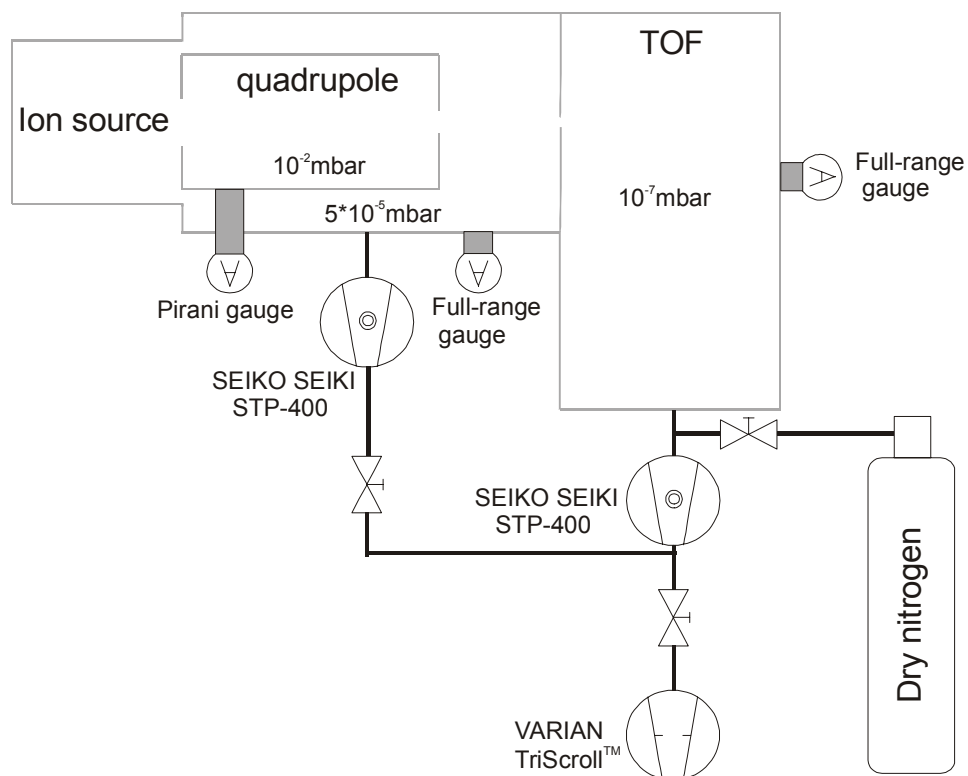


Fig.(2-17(b)): The vacuum system with Cs- or Laser- ion source. It has two stages of differential pumping in order to maintain the needed pressure in the Ortho-TOF MS.

Chapter 3

Experimental results and discussion

3.1 Investigation of cooling and trapping of the ions in the RFQ

The RFQ can be operated in two modes; in a continuous mode and bunch mode.

In the continuous mode the RFQ works as an ion cooler/guide. In the bunch mode the ions after cooling are trapped at the end of the RFQ for a controlled time interval and then extracted out of the RFQ in a well-confined bunch. The distribution of the DC-electrical field along the RFQ for both modes is shown schematically in Fig.(3-1). The green curve corresponds to the continuous mode and to the extraction stage of the bunch mode. The red curve corresponds to the storage stage of the bunch mode.

While the efficiency in the continuous mode due to the geometrical realization is about three times lower than in the bunch mode, a broad mass range of a few hundreds atomic mass units can be simultaneously investigated in the continuous mode, where as in the bunch mode only a few tens of atomic mass units can be covered.

The choice between these two modes is determined by the conditions of the experiment to be conducted. For instance, at an *on-line* experiment at the SHIP at GSI where the production rate of the ions of interest is very low and can amount to several nuclides of interest per hour only the bunch mode should be used in order to achieve the maximum efficiency. For other experiments where the production rate of the nuclides of interest is high enough and the broad mass range is more important than the high efficiency the continuous mode should be chosen.

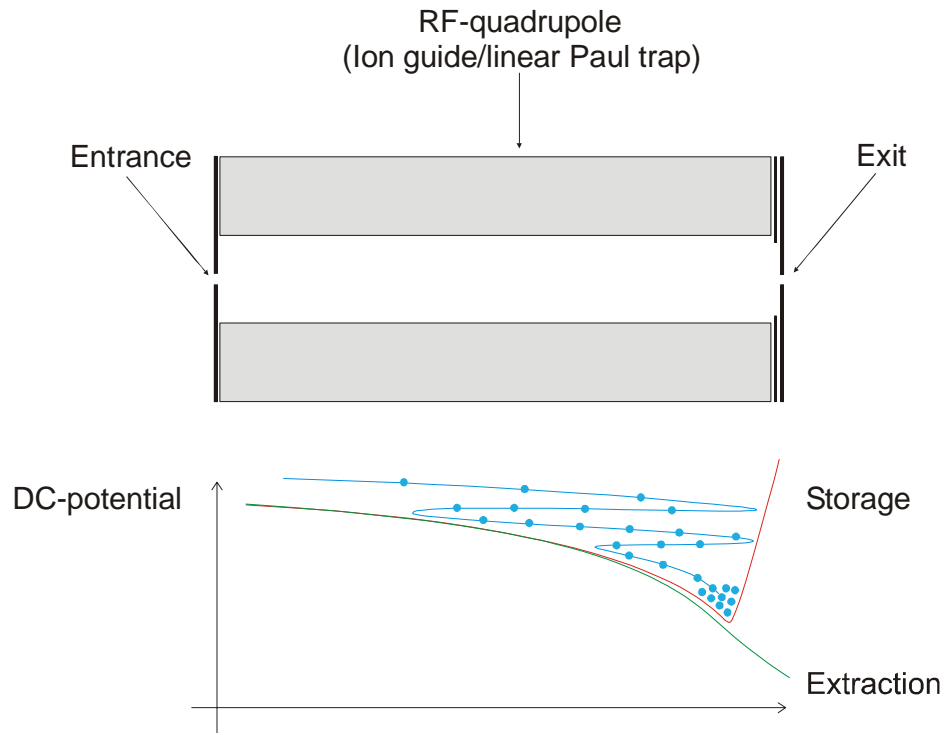


Fig.(3-1): Schematic view of the distribution of the electrical DC-potential along the RFQ. The RFQ can be operated in two modes; in a continuous mode and bunch mode. In the continuous mode the RFQ works as an ion cooler/guide. In the bunch mode the ions after cooling are trapped at the end of the RFQ for a controlled time interval and then extracted from the RFQ in the form of a well-confined bunch.

In order to investigate the cooling and storage properties of the RFQ in both modes, the test set-up shown in Fig.(3-2) was developed.

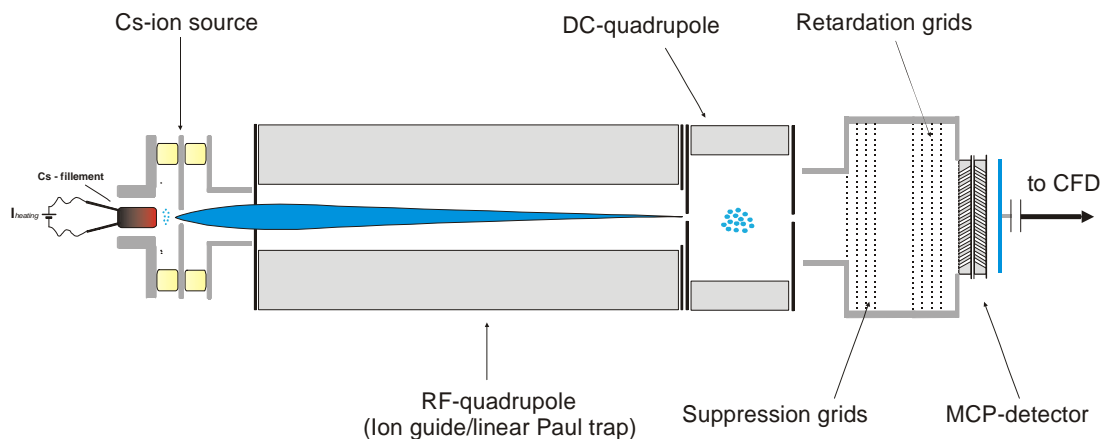


Fig.(3-2): Test set-up for the investigation of the cooling and trapping properties of the RFQ. As the test-RFQ a LINAC-type RFQ was chosen. The detection system consists of three parts: MCP-detector, retardation grids and suppression grids. By varying the electrical potential applied to the retardation grids one can measure the energy distribution of the ions.

As the test-RFQ the LINAC-type RFQ was chosen. As ion source the Cs-surface ionization ion source was used. It delivers an ion beam with a very stable ion current up to a few μA . This gives the possibility to conduct quantitative investigations.

The detection system of the test system consists of three parts: a MCP-detector, several retardation grids and several suppression grids.

The ions with a kinetic energy less than the potential energy defined by the retardation grids potential are reflected by the retardation grids. The ions with a kinetic energy higher than the potential energy defined by the retardation grids potential can fly through the retardation grids and reach the MCP-detector. Thus, by varying the electrical potential applied to the retardation grids one can measure the kinetic energy and kinetic energy distribution of the ions. The detection efficiency of the MCP-detector depends on the intensity of the ion beam hitting the MCP-detector. Due to a saturation effect the detection efficiency drops at a high beam intensity. In order to avoid this drop, and therefore an uncertainty in the detection efficiency, a set of suppression grids can be inserted between the exit of the RFQ and the retardation grids.

3.1.1 Continuous mode

As it is shown in Chapter 4 the mass resolving power of the Ortho-TOF MS is mainly limited by the turn-around-time which depends on the energy spread of the ions after the cooling in the RFQ.

There are two effects that can influence the energy spread of the ions after the cooling in the RFQ: gas pressure in the RFQ and RF-heating of the ions.

Investigation of the mean kinetic energy and the kinetic energy spread of the ions after cooling vs pressure in the RFQ

The experimentally measured mean kinetic energy and kinetic energy spread (FWHM) of the ions after cooling vs pressure in the RFQ are plotted in Fig.(3-3(a,b)).

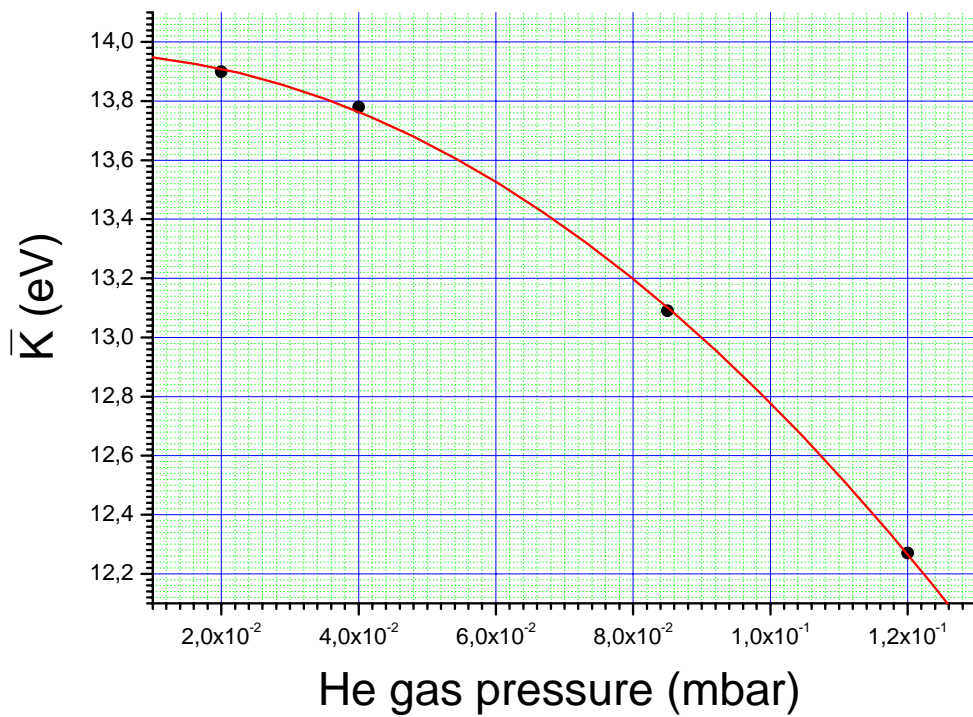


Fig.(3-3(a)): The measured mean kinetic energy of the ions after cooling vs He pressure in the RFQ. The errors of the measurements are smaller than the full circles.

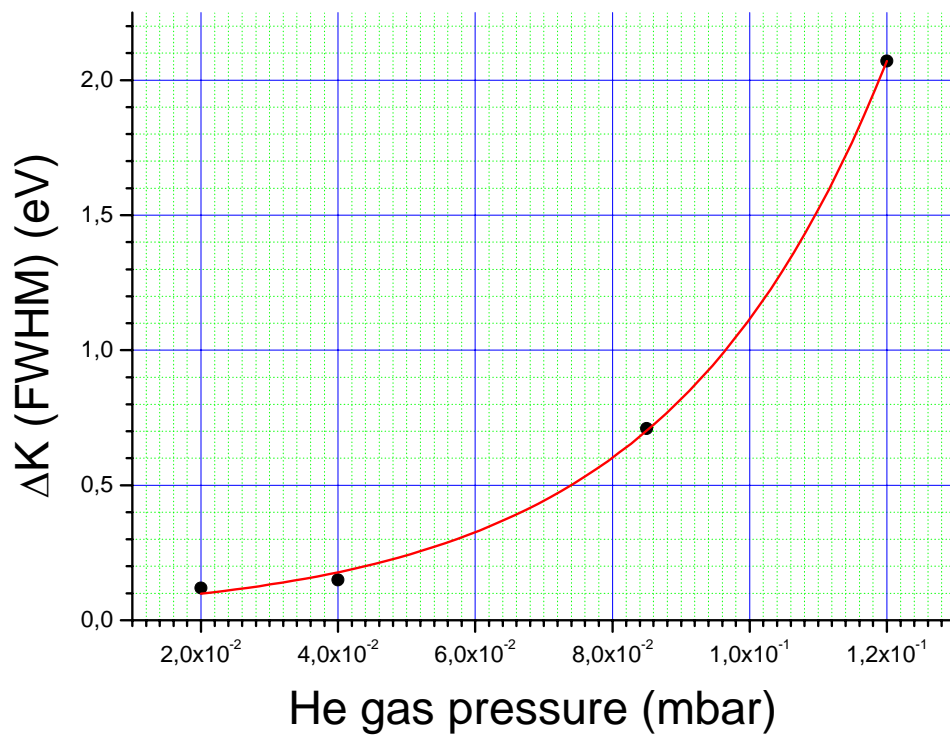


Fig.(3-3(b)): The measured kinetic energy spread of the ions after the cooling and ejection from the RFQ vs He pressure in the RFQ. The errors of the measurements are smaller than the full circles.

From the measurements it can be seen that the mean kinetic energy of the ions drops and the kinetic energy spread of the ions becomes broader with increase of the pressure in the RFQ. This can be explained in the following way: The RFQ can be divided into two regions with respect to strength of the electrical field applied along the RFQ (see Fig.(3-4)).

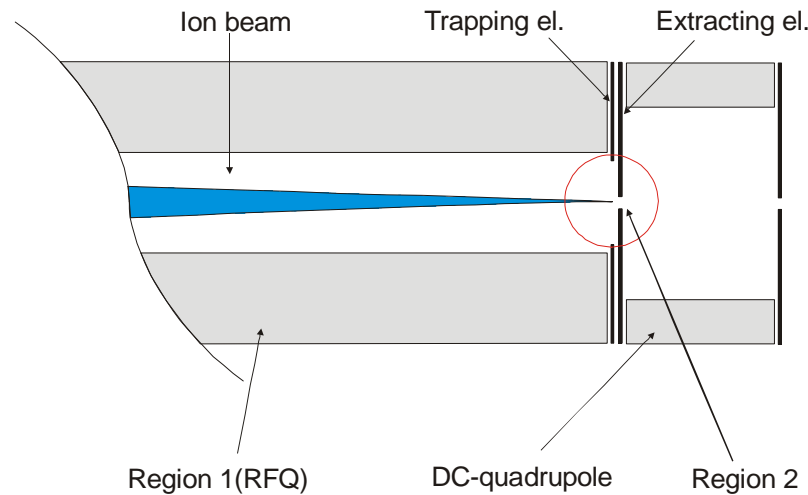


Fig.(3-4): The RFQ: In region 1 cooling of the ions takes place, region 2 is for fast ion extraction from the RFQ. In region 1 the strength of the electrical field along the RFQ is very weak ($E=0.05\text{V/cm}$), whereas in region 2 between the end of the RFQ, trapping electrode and extracting electrode, the strength of the electrical field is very high (100V/cm).

In the first region the strength of the electrical field along the RFQ is very weak ($E=0.05\text{V/cm}$) and serves for dragging the ions along the RFQ. The kinetic energy distribution of the ions in region 1 is $\sim 0.1\text{ eV}$. In region 2 between the end of the RFQ, trapping electrode and extracting electrode, the strength of the electrical field is very high (100 V/cm). If the ions undergo collisions with the buffer gas in this region their mean energy becomes lower and the energy spread becomes broader. The more collisions they undergo the lower the mean energy and the broader the energy spread of the ions extracted out of the RFQ. This explains the qualitative behavior of the curves in Fig.(3-3(a,b)).

A typical energy spread of cooled ions in Region 1 is $\sim 0.1\text{ eV}$. From the experimental curve it can be concluded that the pressure of He in the RFQ should not exceed $2 \cdot 10^{-2}\text{ mbar}$ if one wants to keep the kinetic energy spread of the ions at the level of the kinetic energy distribution of the buffer gas. This value should be the

upper limit for the He pressure in the RFQ when the Ortho-TOF MS is coupled to the RFQ.

Cs-ion transmission through the RFQ vs the RF-potential applied to the RFQ

In Fig.(3-5) the measured transmission of the RFQ for Cs-ions is shown as a function of the RF-potential applied to the RFQ. q -axis indicates Mathieu parameter (see Eq.(1_24)). The parameters of the LINAC RFQ are following: radius $r_0=3.65$ mm, length $L=40$ cm, angular frequency $\Omega=10^7$ 1/s.

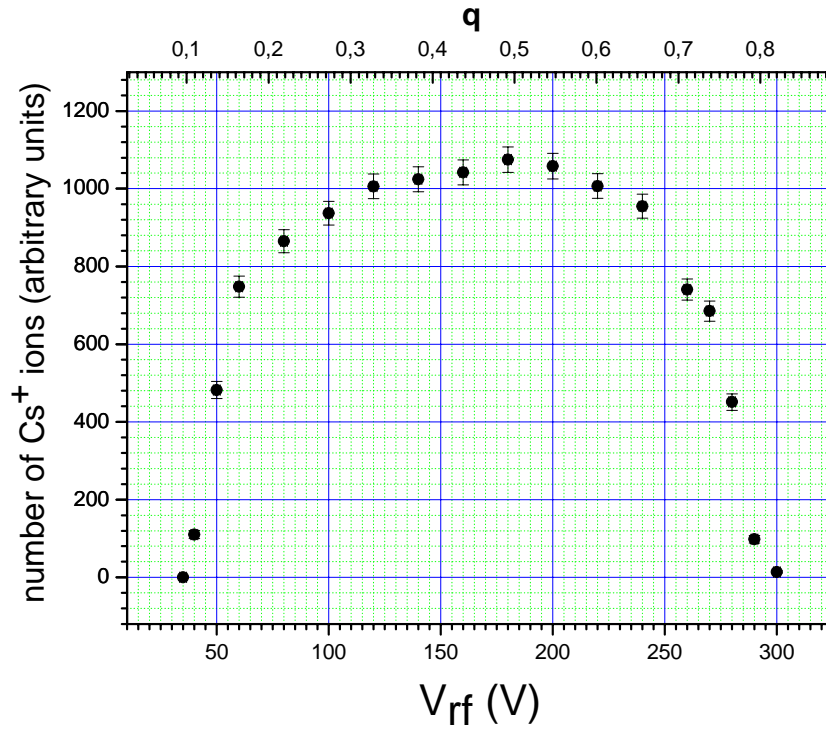


Fig.(3-5): Measured Cs-ion transmission through the RFQ vs the RF-potential. The q -axis indicates the Mathieu parameter.

The transmission efficiency of the RFQ is low at low values of q due to a low value of the pseudo-potential (see Eq.(1_22) and Eq.(1_24)), which accounts for the focusing of the ions towards the RFQ-axis, stays constant at moderate values of q and drops to zero at q -values close to 0.9, which corresponds to the onset of ion motional instability.

Investigation of the mean kinetic energy and the kinetic energy spread of the ions
after cooling vs RF-amplitude applied to the RFQ

The experimental mean kinetic energy and kinetic energy spread of the ions after the cooling vs RF-potential of the RFQ are plotted in Fig(3-6(a,b)).

From the figures it can be seen that the mean kinetic energy of the ions increases linearly and the energy spread of the ions becomes broader with an increase of RF-amplitude.

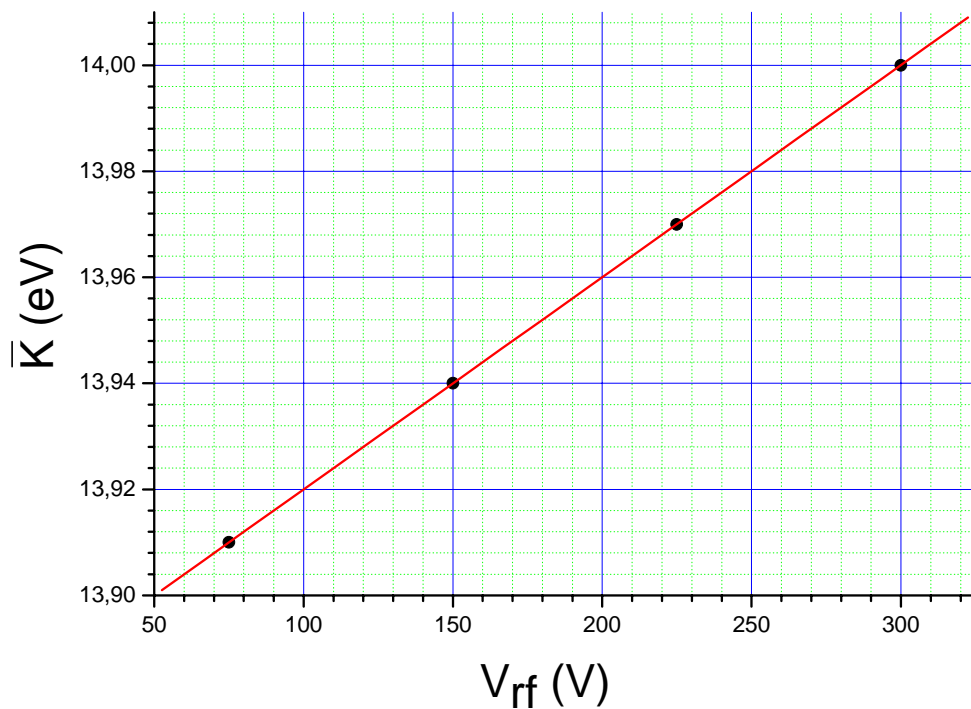


Fig.(3-6(a)): The measured mean kinetic energy of the ions after cooling vs RF-potential applied to the RFQ. The errors of the measurements are smaller than the full circles.

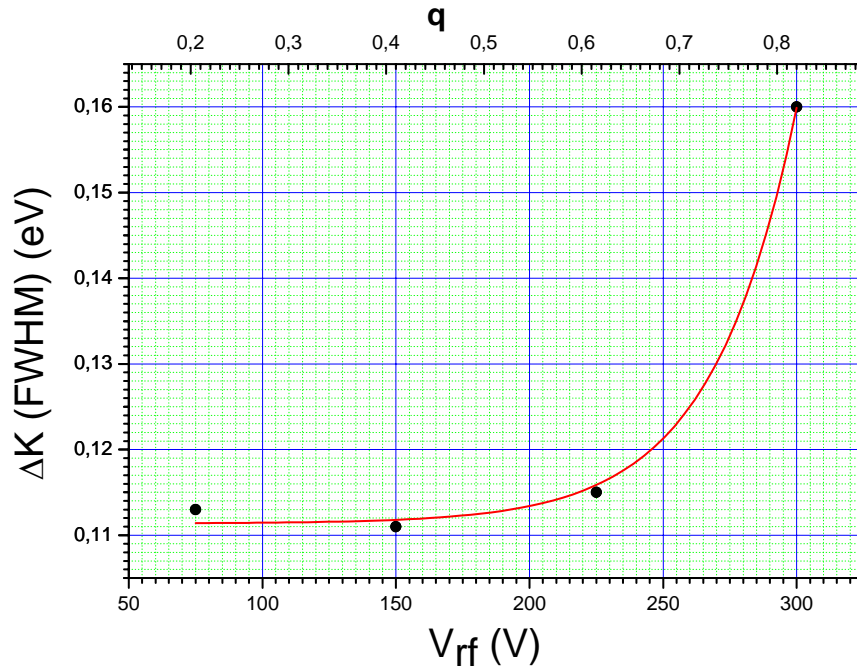


Fig.(3-6(b)): The measured kinetic energy spread of the ions after cooling vs RF-amplitude applied to the RFQ. The errors of the measurements are smaller than the full circles. The q -axis indicates the Mathieu parameter. The drastic increase of the kinetic energy spread at higher RF-amplitude, i.e. at higher Mathieu parameter, is due to RF-field heating of the ions and agrees with the theory [Daw76]

From the theory of the cooling in a RFQ (see chapter 1, subchapter 1.2.2) is known that the ions in a RFQ are subject to two different effects: (1) cooling effect: due to the collisions of the ions with the buffer gas the energy spread of the ions tends to reach the doubled energy spread of the buffer gas and (2) heating effect: the ions gain some amount of energy from the RF-field. The heating effect starts to play a significant role only when q (see Eq.(1_24)) is higher than 0.8. Below this value the cooling effect dominates and heating effect can be neglected.

The rise of the mean energy of the ions after cooling with respect to RF-amplitude can be explained by a slight asymmetry of the RF-potential. The energy spread of the ions after cooling is constant for $q < 0.4$ and equals ~ 0.11 eV and grows drastically for $q > 0.7$, which is in agreement with the theory [Daw76]. The following conclusion can be derived:

The RFQ should be operated at q -values between 0.35 and 0.6 in order to: (1) avoid a low transmission efficiency of the ions through the RFQ and (2) to achieve the most effective cooling of the ions in the RFQ.

3.1.2 Bunch mode

Investigation of ions time of flight through the RFQ vs pressure in the RFQ

The overall time of flight of the ions from the entrance of the RFQ to the MCP-detector of the Ortho-TOF MS ($t_{flight}^{overall}$) is a very important characteristic. Only nuclides with half-life longer than $t_{flight}^{overall}$ can be efficiently investigated with the Ortho-TOF MS. The time of flight of the ions through the RFQ t_{flight}^{RFQ} dominates in $t_{flight}^{overall}$.

The goal is to minimize t_{flight}^{RFQ} . This can be achieved by varying the pressure in the RFQ. The experimental set-up is shown in Fig.(3-2). The timing diagram of the measurement is presented in Fig.(3-7). The output electrode of the Cs-ion source can be pulsed. When a potential of $\sim +25V$ is applied, the ion source is closed ($V_{ion\ source}$ corresponding to “closed” level in Fig.(3-7)). Switching the ion source potential down to zero ($V_{ion\ source}$ corresponding to “open” level in Fig.(3-7)) a bunch the Cs-ions is extracted. Making a scan of the trapping time of the linear RFQ trap (see Fig.(3-7)) one obtains the number of ions reaching the linear RFQ trap as a function of the trapping time (see Fig.(3-8)). The time of flight of the Cs-ions through the RFQ corresponds to the saturation of the curve. Making the same procedure for different He pressures in the RFQ one obtains the time of flight of the ions through the RFQ as a function of the He pressure in the RFQ (see Fig.(3-9)).

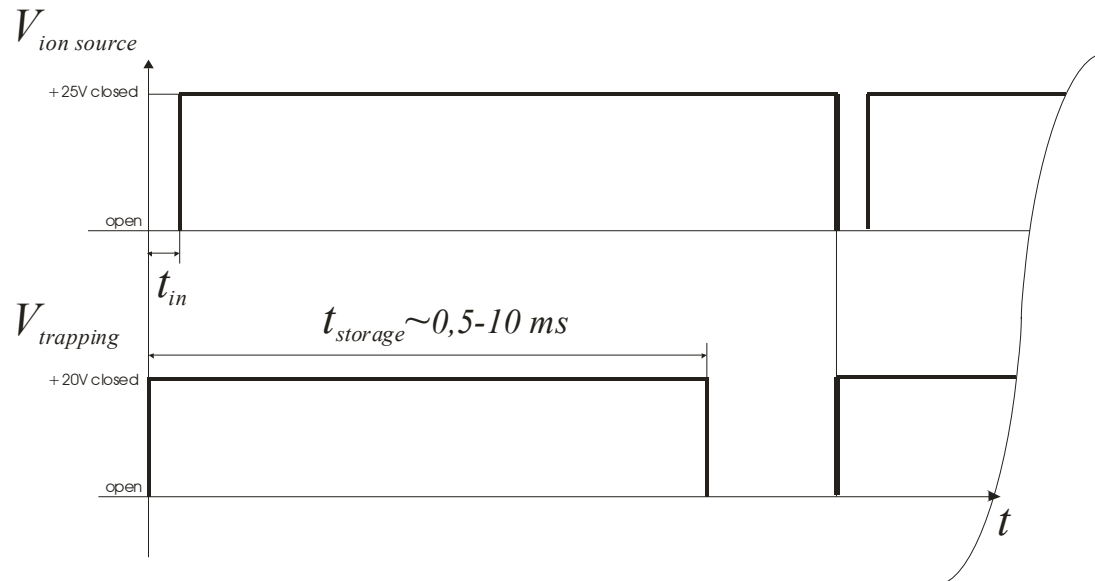


Fig.(3-7): Timing diagram for the investigation of the ions flight-time through the RFQ. The output electrode of the Cs-ion source can be switched. When a potential of $\sim +25\text{V}$ is applied, the ion source is closed ($V_{ion\ source}$ corresponding to “closed” level). Switching the ion source potential down to zero ($V_{ion\ source}$ corresponding to “open” level) one can bunch the Cs-ion source beam. By scanning the trapping time of the linear RFQ trap one obtains the number of ions reaching the linear RFQ trap as a function of the trapping time.

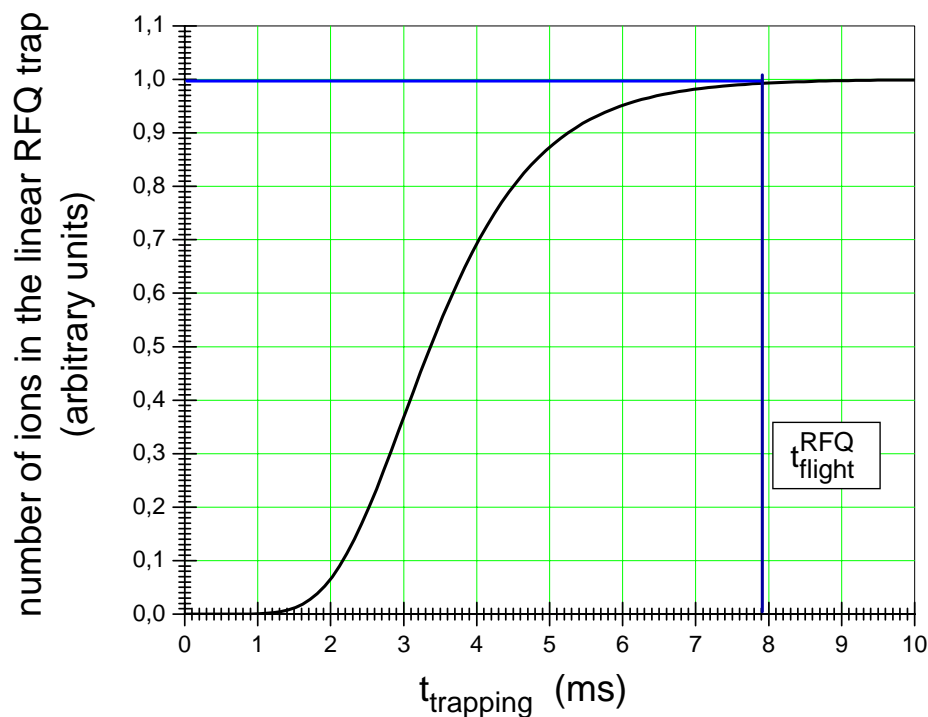


Fig.(3-8): Measured number of ions reaching the linear RFQ trap as a function of the trapping time of the linear RFQ trap for a He pressure of $3 \cdot 10^{-2}$ mbar in the RFQ.

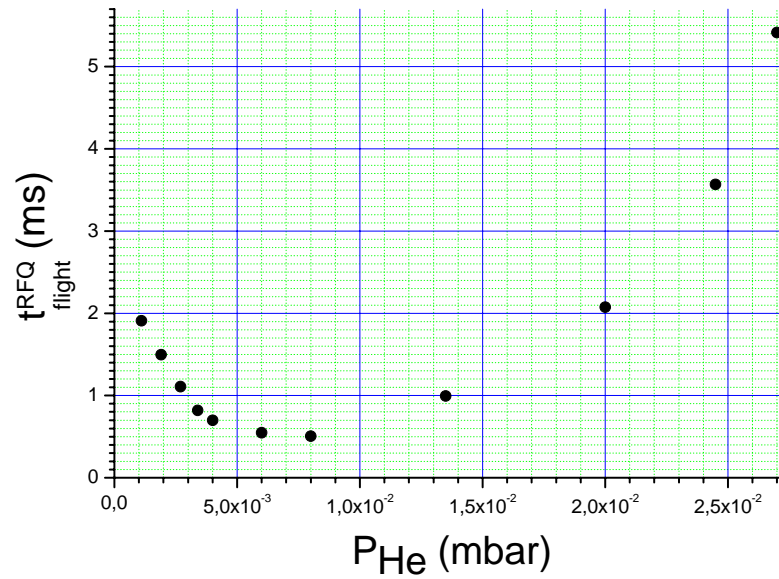


Fig.(3-9): Measured time of flight of the ions through the RFQ vs the He pressure in the RFQ. The errors of the measurements are smaller than the full circles. The curve has a minimum $t_{minimum}^{RFQ} = 0.5ms$ at a pressure $8 \cdot 10^{-3} mbar$. At this pressure the ions are cooled right at the exit of the RFQ after one pass (the RFQ length is 40 cm, the kinetic energy of the incoming ions is about 4 eV). At lower pressure the ions make several passes until they are cooled. At higher pressure the ions are already cooled somewhere in the RFQ and slowly drift to the exit of the RFQ.

The curve has a minimum $t_{minimum}^{RFQ} = 0.5ms$ at a pressure $8 \cdot 10^{-3} mbar$. At this pressure the ions are cooled right at the exit of the RFQ after one pass (the RFQ length is 40 cm, the kinetic energy of the incoming ions is about 4 eV). At lower pressure the ions make several passes until they are cooled. This explains why t_{flight}^{RFQ} at lower pressure is longer than $t_{minimum}^{RFQ}$. At higher pressure the ions are already cooled somewhere in the RFQ and slowly drift to the exit of the RFQ.

It can be concluded that the time property of the TOF allows to investigate the nuclides with half-life longer than 0.5 ms, the pressure $8 \cdot 10^{-3} mbar$ should be chosen as an optimal pressure of He in the RFQ.

Investigation of the ion storage capacity of the linear RFQ trap

According to the calculation presented in Appendix 3 the ion storage capacity of the linear RFQ trap (the number of ions which can be stored in the linear RFQ trap) amounts to about $2 \cdot 10^5$ singly charged ions. Usually only a few ions of interest will

be stored in the linear RFQ trap during an *on-line* experiments with exotic ions. But besides the ions of interest many contaminant nuclides are produced and not separated in the in-flight separator, therefore, the total production rate of all nuclides can become comparable with the ion capacity of the linear RFQ trap. Therefore, and investigation of the ion capacity of the linear RFQ trap is required.

In Fig.(3-10) the experimental dependence of the number of the ions n stored in the linear RFQ trap on the number of the ions injected into the RFQ is presented. The measurement procedure was similar to that for the flight time of the Cs-ions through the RFQ except that the He pressure in the RFQ and the trapping time were kept constant to $1 \cdot 10^{-2}$ mbar and 1ms, respectively (optimum pressure and trapping time; see Fig.(3-9)). As can be seen from Fig.(3-10), the trapping efficiency of the linear RFQ trap is almost 100% for up to $5 \cdot 10^4$ ions injected into the RFQ. For larger number of ions injected into the RFQ the space charge of the ions trapped in the linear RFQ trap becomes significant, and this limits the capacity of the linear RFQ trap to about $1,4 \cdot 10^5$ ions.

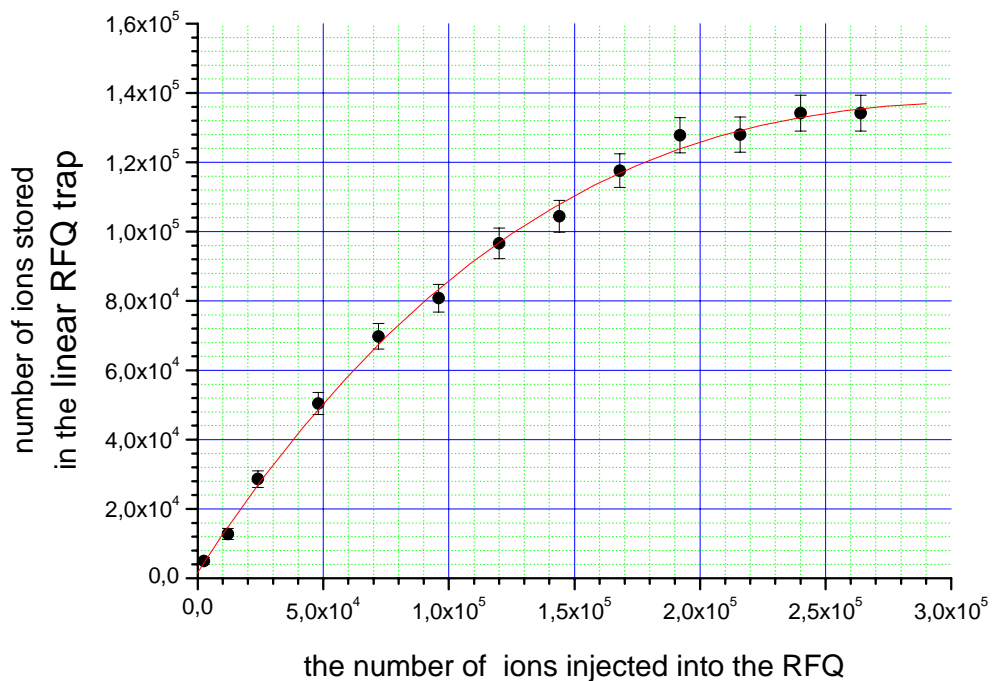


Fig.(3-10): Experimental dependence of the number of the ions n stored in the linear RFQ trap on the number of the ions injected into the RFQ. The ion capacity of the linear RFQ trap (the number of the ions which can be stored in the linear RFQ trap) amounts to about $1.4 \cdot 10^5$ ions and limited by space charge repulsion of the ions in the linear RFQ trap.

From the SIMION simulation (see Fig.(A3-5), Appendix 3) it can be seen that the linear RFQ trap can efficiently store up to $2.2 \cdot 10^5$ ions. The experimental measurement gives $1.4 \cdot 10^5$ ions. Taking into account that the errors of the measurement of the absolute number of the Cs-ions and the SIMION simulation are estimated to lie in a range of about a hundred percents one can conclude that the experimental measurement is in agreement with the SIMION simulation.

Investigation of the mean kinetic energy and the kinetic energy spread of the ions extracted from the linear RFQ trap vs the number of the ions stored.

In this subchapter the mean kinetic energy and the kinetic energy spread of the ions extracted out of the linear RFQ trap are investigated. The experimental results of the mean kinetic energy and the kinetic energy spread of the ions extracted out of the linear RFQ trap are shown in Fig.(3-11).

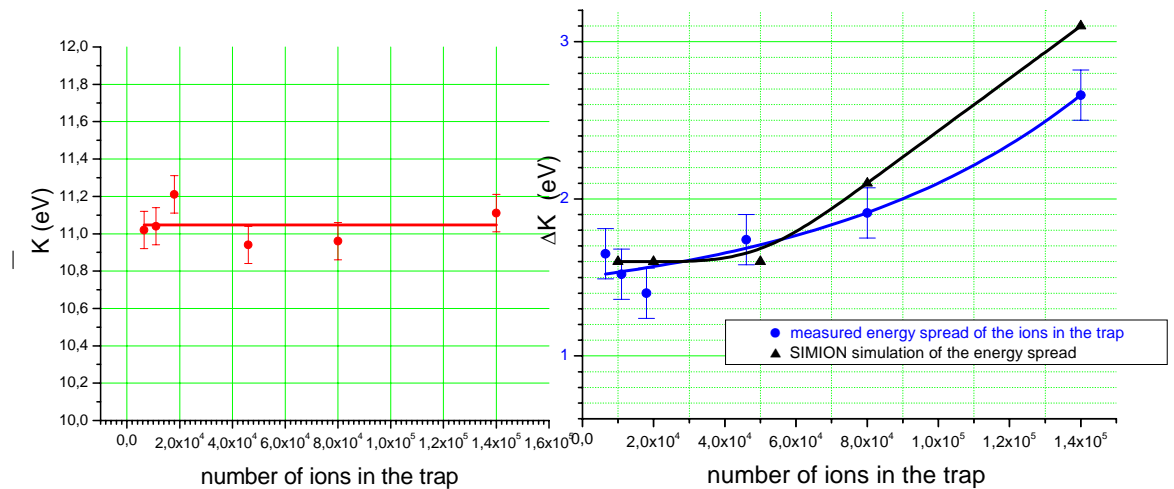


Fig.(3-11): Measured mean kinetic energy (red curve), measured kinetic energy spread (blue curve) and SIMION simulation of kinetic energy spread (black curve) of the ions extracted from the linear RFQ trap

It should be noted that in the bunch mode the kinetic energy spread of the ions extracted out of the RFQ is defined by their spatial distribution in the linear RFQ trap (see Fig.(A3-3) in Appendix 3). The experimentally measured mean kinetic energy does not depend on the number of ions stored in the linear RFQ trap, which is in agreement with the Fig.(A3-3) in Appendix 3. The experimentally measured mean

energy (11.05 ± 0.05 eV) and the mean energy derived from Fig.(A3-3) (11.1 eV) are in perfect agreement with each other.

The ions due to their quasi-thermal kinetic energy distribution occupy a certain minimum volume in the RFQ trap until their number exceeds $n_{no_charge_effect} \cong 5 * 10^4$ (Appendix 3) and space charge effect starts to push them away from each other, increasing the space they occupy and, as a result, the kinetic energy spread of the ions extracted out of the linear RFQ trap. As one can see the behavior of the experimental curve (Fig.(3-11) blue curve) agrees with the expected behavior of the ions in the linear RFQ trap mentioned above. Let us do a quantitative comparison:

It can be seen from Fig.(A3-3) that the kinetic energy spread of the extracted ions is a function of $U_{trapping}$ (see Appendix 3 for the definition of $U_{trapping}$) and, thus, a function of the number of the ions. From Fig.(A3-3) this function can be derived:

$$\Delta K = -1.8 + 40.5 * U_{trapping} - 65 * U_{trapping}^2 \quad [\text{eV}] \quad (3_1)$$

where $U_{trapping}$ ranges from 0.1eV to 0.5eV. For $U_{trapping} < 0.1\text{eV}$ one obtains $\Delta K = 1.6\text{eV}$.

Combining Eq.(3_1) and Eq.(A3_8) one can find the following dependence which is plotted in Fig.(3-11).

The SIMION simulation increases more steeply with the number n of ions. While Eq.(A3_8) does not correctly describe the ‘tail’ part of the linear RFQ trap (large values of n) (see Appendix 3, Fig.(A3-6)), the central part of the linear RFQ trap (low values of n) is well described. Since, only the shape of the central part of the RFQ trap is important for our applications one can conclude that the SIMION-simulation predicts the behavior of the linear RFQ trap correctly.

Investigation of the storage time of the ions in the linear RFQ trap vs impurity pressure in the RFQ

The storage time $T_{storage}$ of the ions in the linear RFQ-trap can be defined as the time after which only half of the initial quantity of the ions remains in the trap. There are

several conditions which determine the storage time:(1) space charge effects, (2) mechanical imperfection of the RFQ and (3) charge exchange collisions of the ions with impurities in the buffer gas He and, therefore, neutralization of the ions.

Since we consider here only a small number of ions stored in the linear RFQ trap, space charge effects can be neglected. The impurity pressure (the pressure of residual gases and water vapors in He) was varied from 10^{-5} mbar up to 10^{-3} mbar . The experimental dependence of the storage time from the impurity level is presented in Fig.(3-12). As expected, the storage time drops with increasing impurity pressure (a sum of the O₂, N₂ and H₂O partial pressures). This indicates that the collisions of the ions with impurities does lead to significant reduction of the storage time. Unfortunately, there is a lack of the experimental data on charge-exchange cross-sections in sub-eV and eV kinetic energy ranges. Thus, we have to rely on model calculations. These calculations are done below.

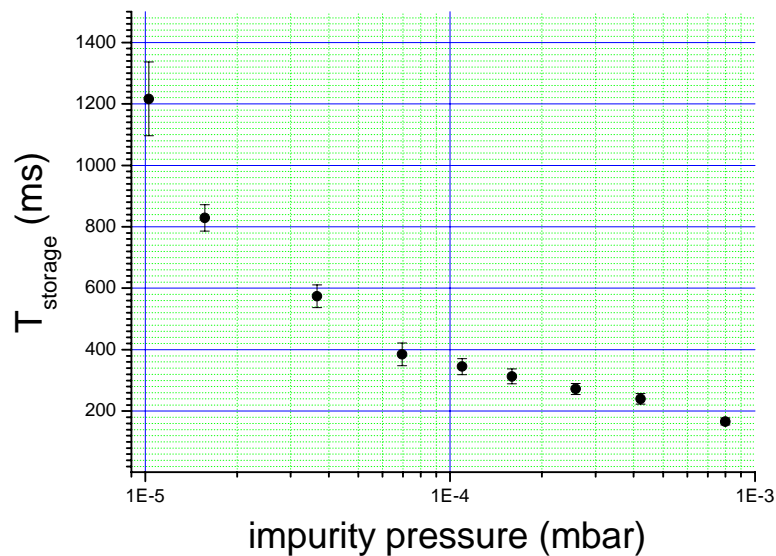


Fig.(3-12): Measured storage time of the Cs-ions in the linear RFQ trap vs the impurity pressure in the RFQ. The impurity pressure implies the pressure of residual gases and water vapors in He (O₂, N₂ and H₂O).

Charge-changing collisional processes taking place in a gas are listed in Table 6 [Has72].

Process	Equation
Single charge transfer	$A^+ + B \rightarrow A + B^+$
Transfer ionization	$A^+ + B \rightarrow A + B^{2+} + e$
Stripping	$A^+ + B \rightarrow A^{2+} + e + B$

Charge transfer to an excited level	$A^+ + B \rightarrow A' + B^+, A^+ + B \rightarrow A + B^{+'}$
Capture by neutral atom	$A + B \rightarrow A^- + B^+$
Collisional detachment	$A^- + B \rightarrow A + e + B$

Table 6: Charge-changing collisional processes taking place in a gas. A^+, B^+ are the projectile and target ions, respectively. A, B are the projectile and target neutrals respectively. A prime is inserted if one of the systems is excited and the symbol e is used if an electron is ejected [Has72]

The kinetic energy of Cs-ions undergoing collisions with the buffer gas in the RFQ is around 0.1 eV, thus transfer ionisation and stripping can not occur because the ionisation potentials of the colliding ions or neutrals are large compared to the kinetic energy. Collisional detachment takes place only when one of the colliding ions is negative. Thus, charge transfer is predominant in our case [Has72].

Two different charge transfer processes can take place [Has72]: (1) Symmetrical resonance charge transfer and (2) Charge transfer between unlike ions and atoms.

Symmetrical resonance charge transfer takes place between two ions or atoms of the same kind. That is not our case.

In our case the Cs-ions collide with the buffer gas, which is He and with impurities, which are mostly N_2 , O_2 and water, thus only charge transfer between unlike ions and atoms should be taken into account.

The adiabatic criterion proposed by Massey [Mas49] is important in these collisions:

$$v_a = \frac{a|\Delta E|}{h} \quad (3_2)$$

where v_a is the impact velocity, a is known as the ‘adiabatic parameter’, a distance of the order of atomic dimensions over which the charge transfer transition is significant, ΔE is the difference between the ionization potentials of colliding ions and atoms, h is the Plank constant.

The kinetic energy that corresponds to v_a is much larger than 1 eV for all charge transfer processes between unlike ions and atoms. Below this energy collisions are called ‘adiabatic’. In this region the relative motion of the atoms is so slow that charge transfer becomes a very unlikely event [Has72]. The collisions of Cs-ions

with the buffer gas can be characterized as ‘adiabatic’. The cross-section σ of an ‘adiabatic’ collision can be approximated as follows [Has72]:

$$\sigma \cong F \left(\frac{v}{\Delta E} \right)^4 E^i \quad (3_3)$$

where v is the impact velocity, F is a constant defined in [Has72] and E^i is the ionization potential of the projectile ion.

The direct calculation of the cross-section σ from Eq.(3_3) can lead to a large error because the theory on which Eq.(3_3) is based is simplified. Instead, one can scale experimentally determined cross-sections to the required conditions, using Eq.(3_3). In our case charge transfer reaction of Cs^+ ions with He, O_2 , N_2 and H_2O can occur. From Eq.(3_3) one has for this case

$$\frac{\sigma_{\text{Cs}^+ + A}}{\sigma_{B^+ + C}} = \left(\frac{v_{\text{Cs}^+ + A}}{v_{B^+ + C}} \right)^4 \left(\frac{\Delta E_{B^+ + C}}{\Delta E_{\text{Cs}^+ + A}} \right)^4 \frac{E_{\text{Cs}^+}^i}{E_{B^+}^i} \quad (3_4)$$

where A , B^+ , C are the ions and atoms undergoing the charge transfer reactions and E^i is the first ionization potential of the ion or atom considered.

The reactions that are considered are listed in Table 7. The buffer gas is assumed to be at rest. Thus, the impact velocity is assumed to be the velocity of incident ions (0.1 eV).

reaction	B^+	C	$K_{B^+ + C}^+$, eV	$E_{B^+}^i$, eV	E_C^i , eV	σ , cm^2	Ref
$\text{Ne}^+ + \text{Ar}$	Ne^+	Ar	0.1	21.564	15.73	10^{-19}	[Has72]
$\text{Cs}^+ + \text{Al}$	Cs^+	Al	0.1	3.89	5.986	$<10^{-19}$	[Rut81]
$\text{Cs}^+ + \text{Fe}$	Cs^+	Fe	0.1	3.89	7.87	$<10^{-19}$	[Rut81]

Table 7: Data on reference reactions used in the storage time estimation. $K_{B^+ + C}^+$ is the kinetic energy of relative motion of B^+ and C that corresponds to $v_{B^+ + C}$ in Eq.(3_4).

Values for $\sigma_{Cs^+ + A}$, calculated from Eq.(3_4) using the data in Table 7, for different gases A (He, O₂, N₂ and H₂O) are presented in Table 8.

reaction	$\sigma_{Cs^+ + A(Ne^+ + Ar)}$, cm ²	$\sigma_{Cs^+ + A(Cs^+ + Al)}$, cm ²	$\sigma_{Cs^+ + A(Cs^+ + Fe)}$, cm ²
Cs ⁺ +He	$\sim 2.5 \cdot 10^{-24}$	$< 6.5 \cdot 10^{-24}$	$< 6.5 \cdot 10^{-23}$
Cs ⁺ +N ₂	$\sim 3.5 \cdot 10^{-23}$	$< 9 \cdot 10^{-23}$	$< 9 \cdot 10^{-22}$
Cs ⁺ +O ₂	$\sim 3.5 \cdot 10^{-23}$	$< 9 \cdot 10^{-23}$	$< 9 \cdot 10^{-22}$
Cs ⁺ +H ₂ O	$\sim 5 \cdot 10^{-19}$	$< 1.3 \cdot 10^{-18}$	$< 1.3 \cdot 10^{-17}$

Table 8: Charge transfer cross-sections of Cs⁺ on He, N₂, O₂ and H₂O derived from different reference reactions (see Table 7)

As can be seen from Table 8 the charge transfer cross-section for the individual reaction varies over one order of magnitude due to the simplified theory of the charge transfer process used and the lack of experimental results in the low energy range.

The storage time of the ions in the linear RFQ trap can be express as follows:

$$T_{storage} = \frac{\ln 2}{vn\sigma} \quad (3_5)$$

where v is the impact velocity, σ is the charge transfer cross-section (Table 8) and n is the density of the target gas.

The He pressure in the RFQ is 10⁻² mbar. The impurities pressure varies from 10⁻⁵ mbar to 10⁻³ mbar. The density of He at 10⁻² mbar at 293 K is $\sim 3 \cdot 10^{14}$ 1/cm³. The storage time for the Cs⁺-ions in different gases at different pressure at 293 K calculated using Table 8 and Eq.(3_5) is given in Table 9.

reaction	T _{storage} [s]				
	10 ⁻² mbar	10 ⁻³ mbar	10 ⁻⁴ mbar	10 ⁻⁵ mbar	10 ⁻⁶ mbar
Cs ⁺ +He	10 ³ -10 ⁴	10 ⁴ -10 ⁵	10 ⁵ -10 ⁶	10 ⁶ -10 ⁷	10 ⁷ -10 ⁸
Cs ⁺ +N ₂	7*(10 ¹ -10 ²)	7*(10 ² -10 ³)	7*(10 ³ -10 ⁴)	7*(10 ⁴ -10 ⁵)	7*(10 ⁵ -10 ⁶)

$\text{Cs}^+ + \text{O}_2$	$7 \cdot (10^1 - 10^2)$	$7 \cdot (10^2 - 10^3)$	$7 \cdot (10^3 - 10^4)$	$7 \cdot (10^4 - 10^5)$	$7 \cdot (10^5 - 10^6)$
$\text{Cs}^+ + \text{H}_2\text{O}$	$5 \cdot (10^{-4} - 10^{-3})$	$5 \cdot (10^{-3} - 10^{-2})$	$5 \cdot (10^{-2} - 10^{-1})$	$5 \cdot (10^{-1} - 10^0)$	$5 \cdot (10^0 - 10^1)$

Table 9: Storage time of Cs^+ in He, N_2 , O_2 and H_2O at different pressures obtained from Eq.(3_5).

Comparing Table 9 with the measured storage time (see Fig.3-12) one can conclude that He, N_2 and O_2 can not be responsible for the limited the storage time. Only collisions of Cs^+ -ions with water molecules can cause a dramatic reduction in the storage time. In Table 10 the partial pressures of the most abundant components of the impurities at different total impurities pressure in the RFQ are listed. A RFQ residual gas analyzer was used for this measurement. The non-linear behavior of water partial pressure with respect to total pressure of impurities is explained by the presence of a residual water pressure in the RFQ at the level of 10^{-6} mbar even if no impurities are let into the RFQ. The water vapors are the most difficult to get rid of from the vacuum system without baking, whereas, N_2 and O_2 cause no problems and can be easily pumped down to the level of 10^{-8} mbar.

Component of the impurities	At total impurities pressure 10^{-3} mbar	At total impurities pressure 10^{-4} mbar	At total impurities pressure 10^{-5} mbar
Part. pressure N_2	$\sim 7.5 \cdot 10^{-4}$ mbar	$\sim 7.5 \cdot 10^{-5}$ mbar	$\sim 7.5 \cdot 10^{-6}$ mbar
Part. pressure O_2	$\sim 2.5 \cdot 10^{-4}$ mbar	$\sim 2.5 \cdot 10^{-5}$ mbar	$\sim 2.5 \cdot 10^{-6}$ mbar
Part. pressure H_2O	$\sim 5 \cdot 10^{-6}$ mbar	$\sim 2 \cdot 10^{-6}$ mbar	$\sim 1 \cdot 10^{-6}$ mbar

Table 10: Partial pressures of N_2 , O_2 and H_2O measured in the set-up at different total impurities pressure. A RFQ residual gas analyzer was used for the measurement.

In Fig.(3-13) the calculated confidence band for the storage time of the Cs^+ -ions in the RFQ , based on Tables 9 and 10, is presented as a function of the total impurities pressure in the RFQ.

As can be seen, the calculated value exceeds the measured value. As it was stated earlier this is due to the simplicity of the theory used for the calculation. For the impact velocity a constant value of 0.1eV was chosen, though the exact real impact velocity can differ by about 20% from the assumed one. Since the storage time is a function of the fifth power of impact velocity, it yields an error of about 150% for the storage time. The difference The behavior of the curves is much more important.

Comparing the experimental curve (see Fig.(3-12)) and calculated curves, one can see almost identical behavior: in both cases the storage time drops with a factor of 6 as the impurities pressure rises by a factor of 100. Thus, the losses of Cs^+ -ions in the RFQ are most probably caused by collisions with the water molecules in the RFQ.

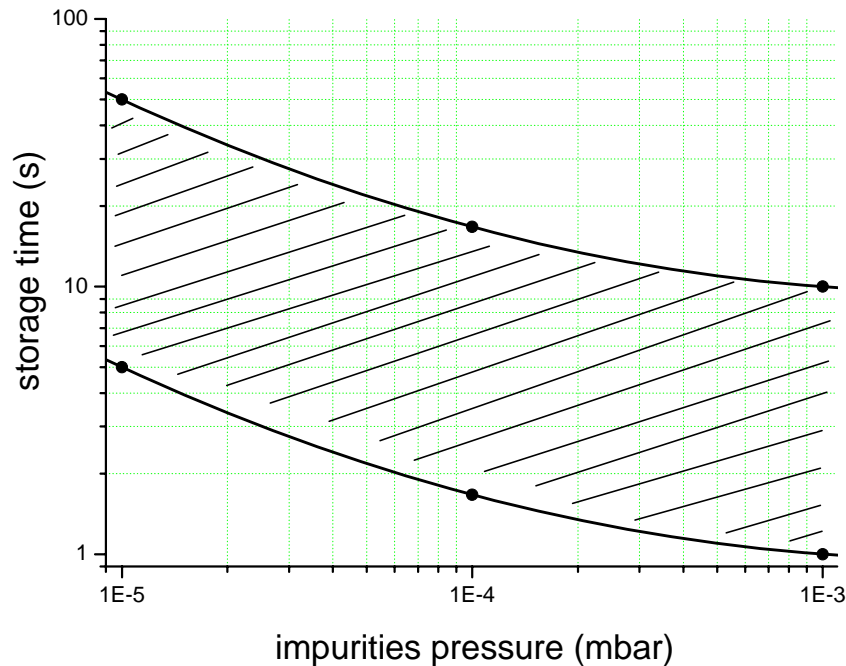


Fig.(3-13): Calculated confidence band for the storage time (see Eq.(3_5)) of the Cs^+ -ions in the linear RFQ trap vs the impurity pressure (H_2O , O_2 , N_2) in the RFQ. The storage time is limited by charge transfer reaction between Cs^+ -ions and water. The charge transfer cross-section for this reaction (see Table 8) is calculated from Eq.(3_4) for different reference reactions (see Table 7).

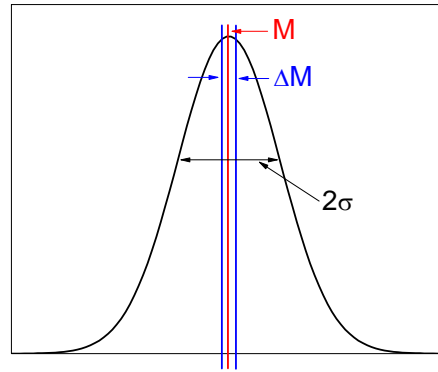
Conclusion:

The storage time of Cs^+ -ions in the RFQ at a water partial pressure of 10^{-6} mbar is more than $1s$. Cs is the best element for long storage times due to its low first ionization potential (3.89 eV). The first ionization potentials of most elements range from 3.89 eV to ~ 15 eV [Nuc00]. The storage time for an element with a high first ionization potential (~ 15 eV) reduces to a value of about 20 ms at a water partial pressure of 10^{-6} mbar. The storage time for an element with a high first ionization potential is much longer than the cooling time of the ions in the RFQ ($< 1\text{ms}$). This means that all elements can be cooled in the RFQ without significant charge exchange losses. If some applications require longer storage times, one should reduce the water partial pressure. This can be done easily down to the level of 10^{-7} mbar by purging the RFQ vacuum chamber with a dry gas like Ar. Further reduction

takes a long time for pumping of the RFQ. The process can be sped up by baking the RFQ vacuum chamber.

3.2 Precision of mass determination

The accuracy of mass determination $\Delta M/M$ and the precision of mass determination $\Delta(\Delta M/M)$ can be defined as follows:



$$\frac{\Delta M}{M} = \frac{M_{lit} - M_{mes}}{M_{lit}}$$

$$\Delta\left(\frac{\Delta M}{M}\right) = \sqrt{\left(\frac{M_{mes} \Delta M_{lit}}{M_{lit}^2}\right)^2 + \left(\frac{\Delta M_{mes}}{M_{lit}}\right)^2} \quad (3_6)$$

where M_{lit} and ΔM_{lit} are the literature value and its error of the nuclide mass, M_{mes} and ΔM_{mes} are the most probable value and standard error of the nuclide mass determination measured with the Ortho-TOF MS. Since $|\Delta M_{mes}| \gg |\Delta M_{lit}|$ for the Ortho-TOF MS, the expression for ΔA_M can be rewritten as follows:

$$\Delta\left(\frac{\Delta M}{M}\right) = |\Delta M_{mes}/M_{lit}| \quad (3_7)$$

The procedure of mass determination consists of several steps: (1) The acquisition of a TOF-spectrum, (2) the mass-calibration of the acquired TOF-spectrum and (3) the determination of the unknown masses of interest in the TOF-spectrum.

Measured TOF-spectra

A typical TOF-spectrum is shown in Fig.(3-14). After fitting with a Gaussian distribution with a small tail on the right side (see in-set in Fig.(3-14)) one obtains the following parameters:

t is the most probable value of the time-of-flight of the nuclide of a given mass

σ is its standard deviation

Δt is the standard error of t determination, which is $\sim \frac{\sigma}{\sqrt{n}}$, where n is the number of counts in the peak.

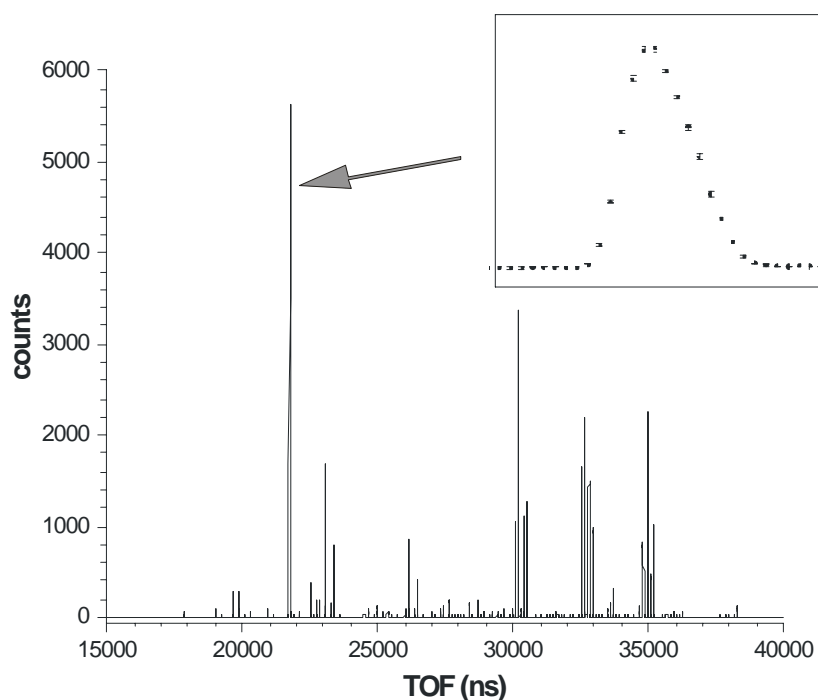


Fig. (3-14): A typical TOF-spectrum, measured with the Ortho-TOF MS. After fitting with a Gaussian distribution including a small tail on the right side one obtains the following parameters:

t is the most probable value of the time-of-flight of the nuclide of a given mass

σ is its standard deviation

Δt is the standard error of t identification, which is $\sim \frac{\sigma}{\sqrt{n}}$, where n is the number of counts in the peak.

Doing the same procedure for every peak in the spectrum one can obtain t and Δt for each peak in the spectrum:

$$\begin{aligned} t_1 \pm \Delta t_1 \\ t_2 \pm \Delta t_2 \\ \dots\dots\dots \\ t_n \pm \Delta t_n \end{aligned} \quad (3_8)$$

The mass-calibration

The next step is the mass calibration of the TOF-spectrum. The mass of the nuclide as a function of its time-of-flight can be driven from the theoretical Eq.(1_1).

$$M = At^2 \quad (3_9)$$

In Eq.(3_9) an additional parameter (B) should be added due to time delays of signals occurring in the data acquisition system. The function, which is used for the mass calibration, is given by Eq.(3_10):

$$M = A(t - B)^2 \quad (3_10)$$

For the mass calibration one chooses several reference peaks, which correspond to nuclides with known masses M_{lit} . By using a least-square fitting procedure one can get for A and B :

$$A = A^{fit} \pm \Delta A^{fit} \text{ and } B = B^{fit} \pm \Delta B^{fit} \quad (3_11)$$

Substituting A^{fit} and B^{fit} in Eq.(3_10) one can obtain the following expression for the identification of unknown masses:

$$M_{exp} = A^{fit} (t - B^{fit})^2 \quad (3_12)$$

The standard deviation and weight error of M_{exp} are functions of $t, A^{fit}, B^{fit}, \Delta A^{fit}$ and ΔB^{fit} ,

$$\begin{aligned}\Delta M_{standard} &= F_1(T, A^{fit}, B^{fit}, \Delta A^{fit}, \Delta B^{fit}) \\ \Delta M_{weight} &= F_2(T, A^{fit}, B^{fit}, \Delta A^{fit}, \Delta B^{fit})\end{aligned}\quad (3_{13})$$

and can be calculated by using the matrix method [Dge74]. As ΔM_{exp} one should take the maximal error [Dge74]:

$$\Delta M_{exp} = \max[\Delta M_{standard}, \Delta M_{weight}] \quad (3_{14})$$

Substituting M_{exp} into Eq.(3_6) and ΔM_{exp} in Eq.(3_7) one can obtain $\Delta M/M \pm \Delta(\Delta M/M)$ for the nuclide of interest.

Determination of unknown masses in the TOF-spectrum

There are two kinds of calibration: (1) External and (2) internal.

An internal calibration implies a presence of reference peaks in the recorded TOF-spectrum. But more often at *on-line* measurements there are no well-known nuclides in the TOF-spectrum. In this case one has to make a mass calibration before the *on-line* measurement (externally). An external calibration brings an additional error into the measurement. In order to overcome this problem we are planning to use a fullerene (C^{60}) laser ion source for internal calibration of the Ortho-TOF MS at *on-line* experiments. The development of this source is the subject of the doctoral thesis of Z.Wang. The source covers the whole TOF-spectrum with known masses with an interval of 12 atomic mass units, if the fullerene target is used with natural carbon isotope ratios, and with intervals of 1 atomic mass unit, if the fullerene source is enriched with ^{13}C .

Internal calibration:

An investigation of the internal calibration was performed for two extreme cases:

(1) The reference peaks are situated close to the unknown peak in the TOF-spectrum and (2) the reference peaks are situated far from the unknown peak in the TOF-spectrum.

The second case was investigated in Munich with a silver beam ($^{107}Ag^{1+}$) from the tandem. The experiment and its results are described in the following chapter. The

investigation of the first case was carried out with three isotopes of Pb ($^{206}\text{Pb}^{1+}$, $^{207}\text{Pb}^{1+}$, $^{208}\text{Pb}^{1+}$).

The source of the Pb-isotopes was the electrospray ion source. $^{207}\text{Pb}^{1+}$ was used as an unknown nuclide, and $^{206}\text{Pb}^{1+}$ and $^{208}\text{Pb}^{1+}$ were used as reference peaks. The distance between the unknown peak and the reference peaks is about 1 mass unit. The TOF-spectrum of the Pb-isotopes is shown in Fig.(3-15). In Table 11 the tabulated values of the Pb-isotopes are presented [Nuc00]. 23 spectra were acquired. For each spectrum the mass accuracy and precision $\Delta M/M \pm \Delta(\Delta M/M)$ were calculated. Fig.(3-16) is a plot of these 23 measurements where the red line is the most probable value of $\Delta M/M$ (-0.2 ppm), the blue lines represent the 67%-confidence band of $\Delta M/M$ (0.51 ppm).

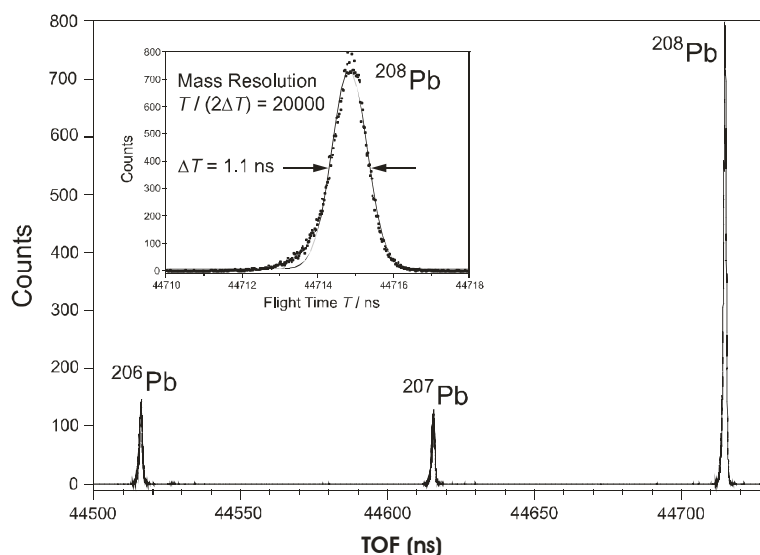


Fig.(3-15): Time-of-flight spectrum of Pb-isotopes acquired with the Ortho-TOF MS. The mass of ^{207}Pb was determined, ^{206}Pb and ^{208}Pb were used as reference peaks.

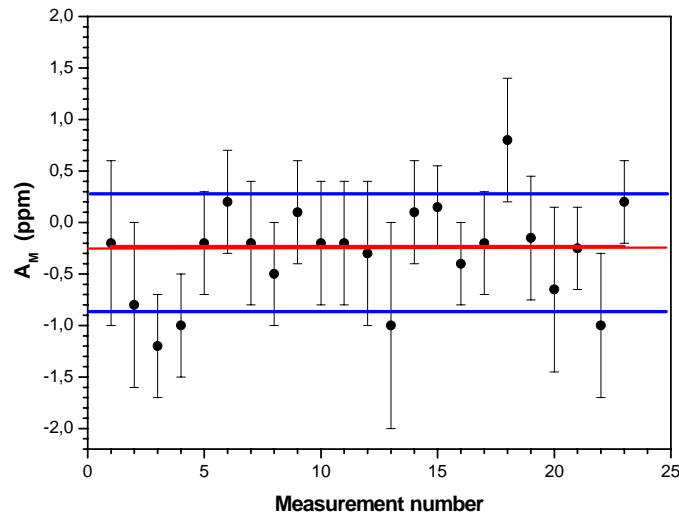


Fig.(3-16): Accuracy of mass determination of $^{207}\text{Pb}^{1+}$. It is a plot of these 23 measurements where the red line is the most probable value of $\Delta M/M$, the blue lines are a 67%-confidence band of $\Delta M/M$.

Pb- isotope	Tabulated mass in atomic units
$^{206}\text{Pb}^{1+}$	205.9738914
$^{207}\text{Pb}^{1+}$	206.9753314
$^{208}\text{Pb}^{1+}$	207.9760814

Table 11: Tabulated values of the Pb-isotopes[Nuc00]. One electron mass is subtracted.

∴

The precision of the mass determination lies below 1 ppm, that corresponds to ± 100 keV of the absolute error of the mass measurement of ^{207}Pb . The accuracy of the mass determination (systematic error) of ^{207}Pb is 40 keV.

3.3 Investigation of the Efficiency and Mass Resolving Power of the Ortho-TOF MS

3.3.1 Efficiency of the Ortho-TOF MS

In order to measure the efficiency of the Ortho-TOF MS, the Cs^+ -ion source was used. It delivers a very stable beam of Cs^+ -ions (see Fig.(2-4)). The efficiency of the Ortho-TOF MS was measured for both the continuous mode and the bunch-mode. The RFQ was adjusted to the maximum transmission of Cs^+ -ions (see Fig.(3-5)). In Fig.(3-17) the efficiency of the Ortho-TOF MS for both modes as a function of the MCP-detector voltage is presented.

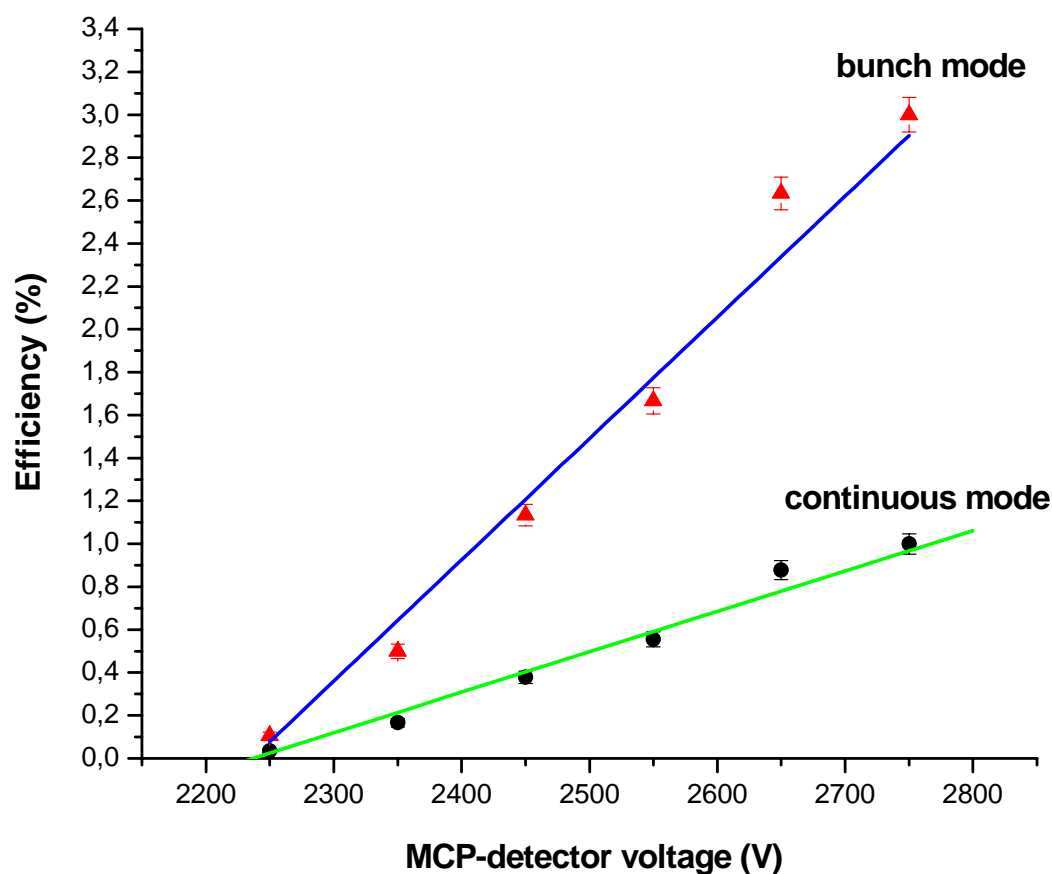


Fig. (3-17): Measured efficiency of the Ortho-TOF-MS in the bunch and continuous modes vs the MCP-detector voltage.

The maximum measured efficiency amounts to 3 % in the bunch mode and 1% in the continuous mode.

From Fig.(3-17) it can be seen that the higher the MCP-detector voltage is the higher the efficiency of the Ortho-TOF MS is. On the other hand, the higher MCP-detector voltage yields a worse ratio of signal to noise. In Fig.(3-18) the number of noise counts per second in a 10 ns interval of a TOF-spectrum is shown vs the MCP-detector voltage for different He pressure in the Ortho-TOF MS.

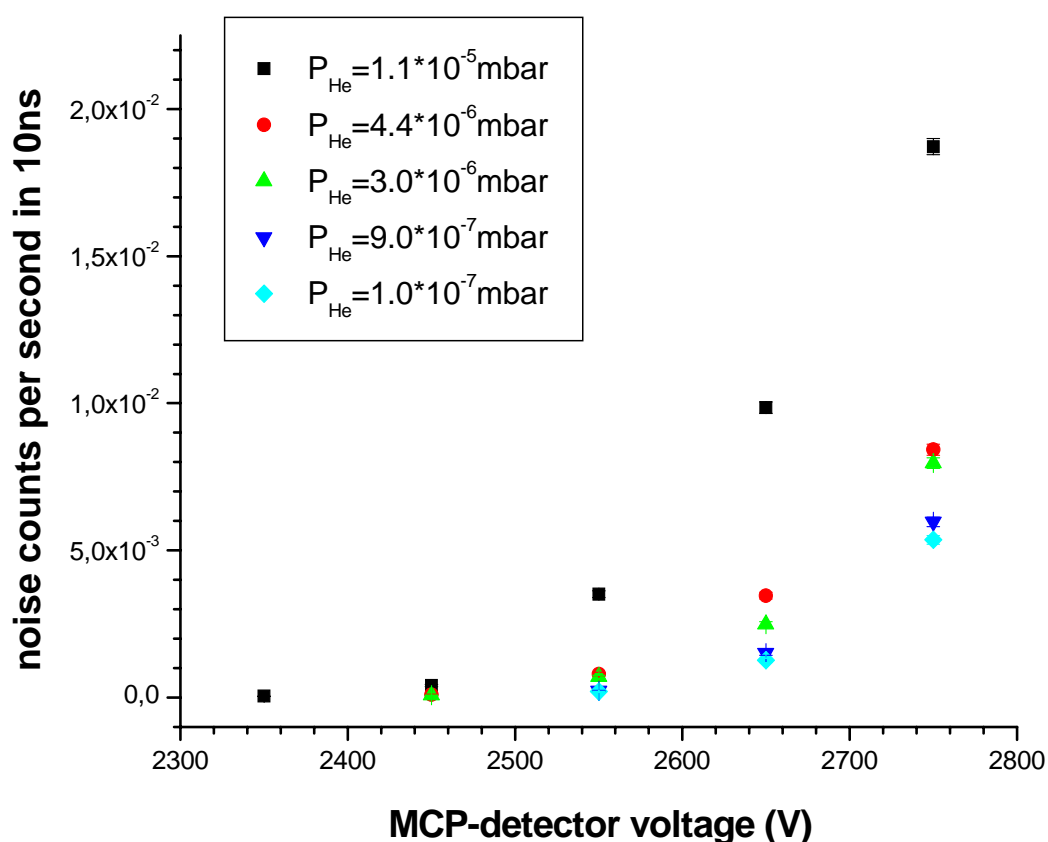


Fig.(3-18): Measured noise properties of the Ortho-TOF MS vs the MCP voltage for different He pressure.

Since a typical peak width at 1% height is around 10 ns, in Fig.(3-18) the number of noise counts per second in 10 ns (in the peak) is used as a measure for the signal-to-noise study. From Fig.(3-17) and Fig.(3-18) it can be seen that the noise counts grow exponentially with the MCP-detector voltage whereas the efficiency grows linearly. In Fig.(3-19) the measured number of noise counts per second in 10 ns is shown vs

the He pressure in the Ortho-TOF MS at the maximum efficiency of the Ortho-TOF MS, which corresponds to a MCP-detector voltage of 2750 V.

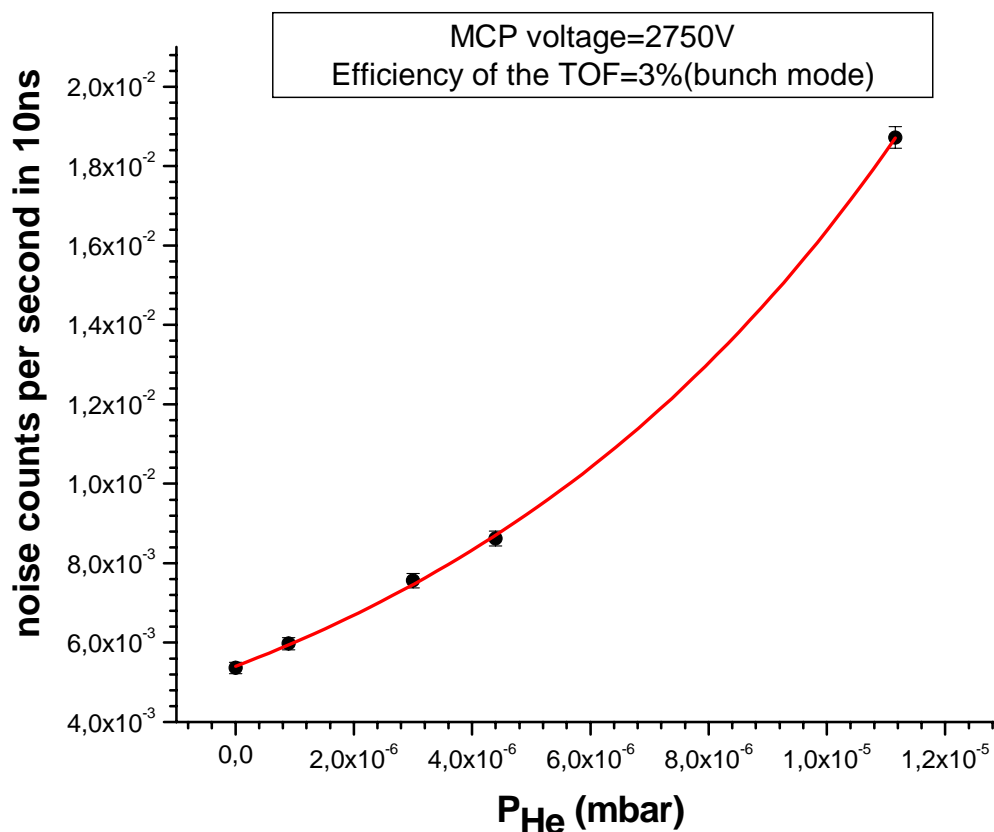


Fig.(3-19): Measured number of noise counts per second within 10 ns vs the He pressures in the Ortho-TOF MS at the condition for maximum efficiency (MCP-detector voltage of 2750 V)

One can differentiate between two cases:

1. The intensity of the ion beam of interest is so small that the Ortho-TOF MS has to be operated at the maximum efficiency. In this case in order to improve the signal-to-noise ratio one can only decrease the He pressure in the Ortho-TOF MS. The minimum noise rate in the peak which can be reached for the MCP-detector used in the Ortho-TOF MS amounts to $5 \cdot 10^{-3}$ noise counts per second within 10 ns. Taking into account the efficiency of the Ortho-TOF MS one can obtain the minimum intensity of the beam of interest entering the Ortho-TOF MS which can be handled with the Ortho-TOF MS (I_{\min}): $I_{\min} = 0.3$ ions per second.
2. The intensity of the ion beam of interest is strong, so that the efficiency of the

Ortho-TOF MS can be sacrificed in order to suppress the noise count rate. This can be achieved by decreasing the MCP voltage. The noise count rate drops exponentially whereas the efficiency comes down only linearly (see Fig.(3-17) and Fig.(3-18)).

3.3.2 Mass Resolving Power of the Ortho-TOF MS

In Fig.(3-20) the Cs⁺-ion TOF-peaks acquired in continuous mode are shown for three different MCP-detector voltages.

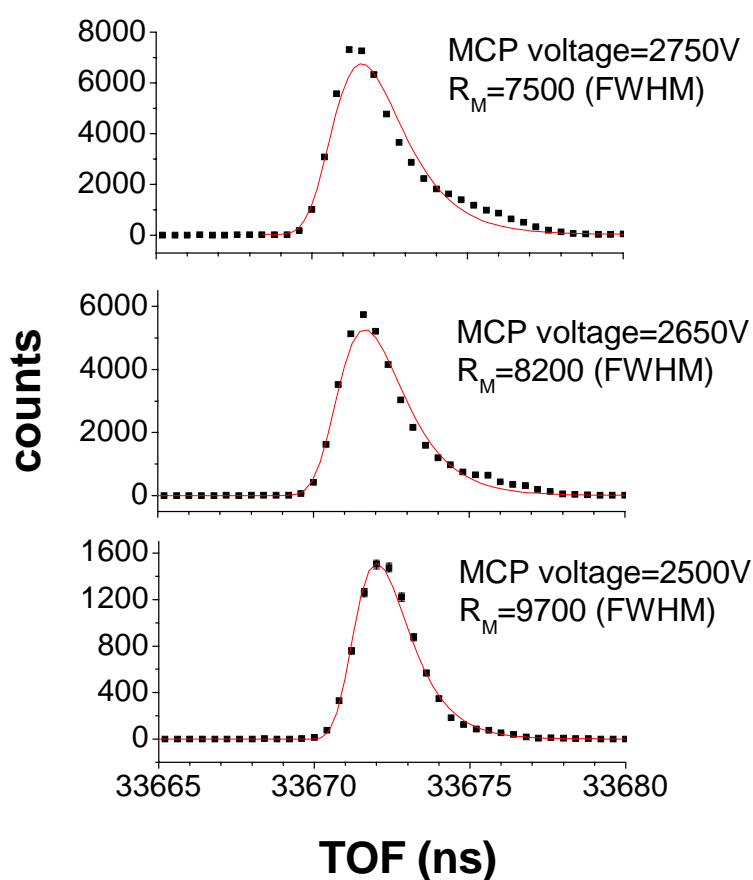


Fig.(3-20): Recorded Cs⁺-ion TOF-peaks in the continuous mode at different MCP-detector voltages.

At high MCP-detector voltage a tail on the right side of the peak becomes larger, and this deteriorates the mass resolving power R_M of the Ortho-TOF MS. This can be explained by a different behavior of the MCP-detector at different MCP-detector voltages. In Fig(3-21) the mass resolving power vs the efficiency of the Ortho-TOF MS in continuous mode is presented.

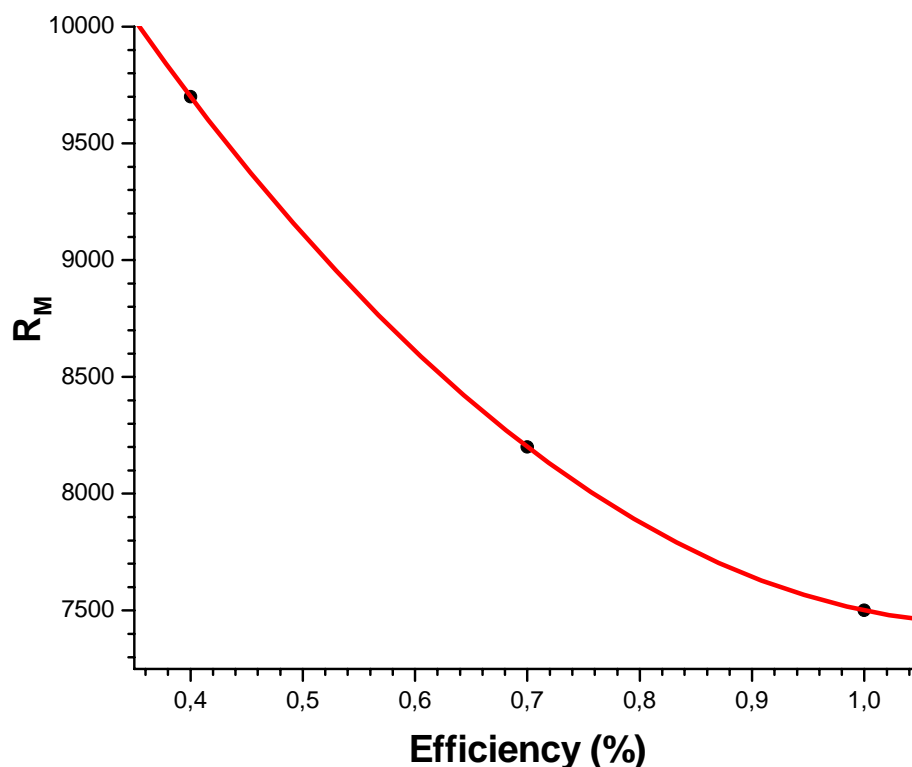


Fig.(3-21): Measured mass resolving power of the Ortho-TOF MS vs the efficiency of the Ortho-TOF MS in continuous mode. The errors of the measurements are smaller than the full circles.

When a high mass resolving power is more important than a high efficiency of the Ortho-TOF MS, the efficiency can be sacrificed in order to reach the maximum R_M equal to 20000 measured for Pb-isotopes as shown in Fig(3-15). When the efficiency is maximized R_M amounts to 7500.

Conclusion:

The maximum efficiency of the Ortho-TOF MS amounts to 3% in the bunch mode and 1% in continuous mode. Under these conditions, a mass resolving power of 8000 can be obtained. The maximum efficiency achieved for the Ortho-TOF MS is about 20000 (see Fig.(3-15)).

The minimum intensity of the beam of interest entering the Ortho-TOF MS which can be handled with the Ortho-TOF MS (I_{min}) is estimated to be 0.3 ions per second. An increase in the mass resolving power leads to smaller efficiency of the Ortho-TOF MS.

Chapter 4

Theoretical investigation of the properties of the built Ortho-TOF MS

The Ortho-TOF MS is characterized by three main properties: (1) Mass resolving power, (2) overall efficiency and (3) accuracy of mass determination .

4.1 Mass resolving power

The theoretical mass resolving power of the Ortho-TOF MS R_{M_ideal} is defined as the mass resolving power of the Ortho-TOF MS due only to a spatial spread of the ions in the modulator. The theoretical mass resolving power of the Ortho-TOF MS was calculated analytically using Eqs.(A1_10,A1_15) and Fig.(A1-3) (see Appendix1). The Mathematica 3.0 code was used to solve these equations. The mass resolving power as a function of the beam width in the modulator is presented in Fig.(A1_3) (see Appendix 1).

Taking a realistic spatial spread of the beam in the modulator of 2 mm one can receive an ideal mass resolving power of $R_{M_ideal} = 130000$.

However, such a high mass resolving power can not be achieved in the Ortho-TOF MS in reality. Additional factors that limit the mass resolving power are (1) the turn-around time R_{M_turn} , (2) the mass resolving power limitation imposed by the MCP-detector (R_{M_MCP}), (3) Stability of HV-power supplies ($R_{M_p.s.}$) and (4) the mass resolving power limitation due to the separating grids(R_{M_grids}).

Assuming that all limitations listed above are independent from each other the overall R_{M_real} can be expressed by

$$\frac{1}{R_{M_real}} = \sqrt{\left(\frac{1}{R_{M_ideal}}\right)^2 + \left(\frac{1}{R_{M_turn}}\right)^2 + \left(\frac{1}{R_{M_MCP}}\right)^2 + \left(\frac{1}{R_{M_p.s}}\right)^2 + \left(\frac{1}{R_{M_grids}}\right)^2} \quad (4_1)$$

The mass resolving power limit due to the turn-around time R_{M_turn} can be expressed as follows (see Eq.(1_12)):

$$R_{M_turn} = \frac{t(z_0)}{2\Delta t_{turn}} = \frac{t(z_0)QE_1}{4M\Delta v_z} \quad (4_2)$$

where $t(z_0)$ is the time-of-flight which corresponds to a reference start position of the ion z_0 in the modulator. All other parameters in Eq.(4_2) are defined in Eq.(1_12). The velocity spread of the ions in the modulator in z-direction Δv_z can be expressed through the kinetic energy of the ions in the modulator and the ion beam angular divergence in the modulator in the direction perpendicular to z-direction α :

$$\Delta v_z = \sqrt{\frac{2}{M}} K * \sin\alpha$$

$$(4_3)$$

Since for $\alpha \ll 1$ $\sin\alpha \approx \alpha$, therefore, $K \approx K_x$, so one can get the following formula for Δv_z :

$$\Delta v_z = \alpha \sqrt{\frac{2}{M}} K_x \quad (4_4)$$

Combining Eq.(4_2) and Eq.(4_4) together one obtains:

$$R_{M_turn} = \frac{t(z_0)QE_I}{4\sqrt{2MK_x}} * \frac{1}{\alpha} \tag{4_5}$$

For typical values used in this work, for Cs⁺-ions $t(z_0) = 33700$ ns, $K_x = 12$ eV , $M = 132.9$ amu , $Q = 1.6 * 10^{-19}$ As, $E_I = 166.67$ V/mm, one has

$$R_{M_turn} = 1040 * \frac{1}{\alpha[\text{rad}]} \tag{4_6}$$

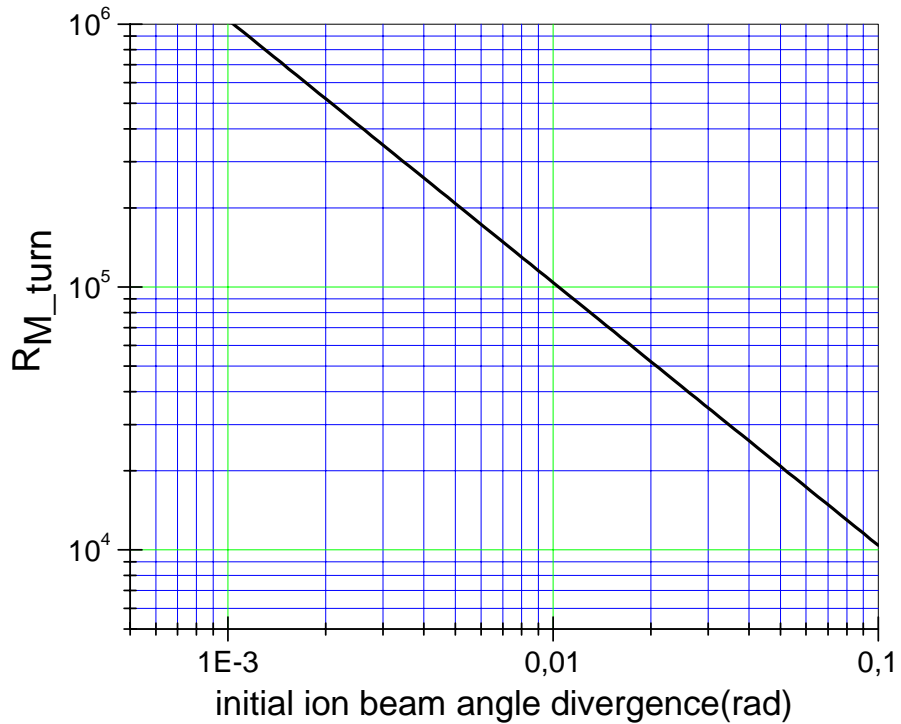


Fig.(4-1): Calculation of the mass resolving power limit R_{M_turn} (Eq.(4_5) and Eq.(4_6)) caused by the initial velocity spread of the ions in the modulator (see Fig.(1_3(c)))

Ions that have been cooled in the RF-quadrupole have a quasi-thermal distribution with a mean kinetic energy of about 0.1 eV, and they are extracted from the RF-quadrupole with a mean energy of $K_x = 12$ eV. Thus, right behind the RF-quadrupole the ions have a kinetic energy in the z -direction of $K_z = 0.1$ eV and a kinetic energy in the direction perpendicular to z -direction $K_x = 12$ eV. Thus, one can obtain for a given ion beam angular divergence α :

$$\alpha = \sqrt{\frac{K_z}{K_x}} \approx 0.1 [\text{rad}] \quad (4_7)$$

According to Fig.(4-1) this value corresponds to a mass resolving power limit R_{M_turn} of 10000. In order to increase R_{M_turn} , an einzel lens (see Fig.(2-1)) is placed between the RF-quadrupole and the modulator. The einzel lens converts the z-component of the ion beam velocity into a spatial spread which can be compensated to some extent (see Fig.(A1_3)). A schematic view of the einzel lens and the modulator is shown in Fig.(4-2).

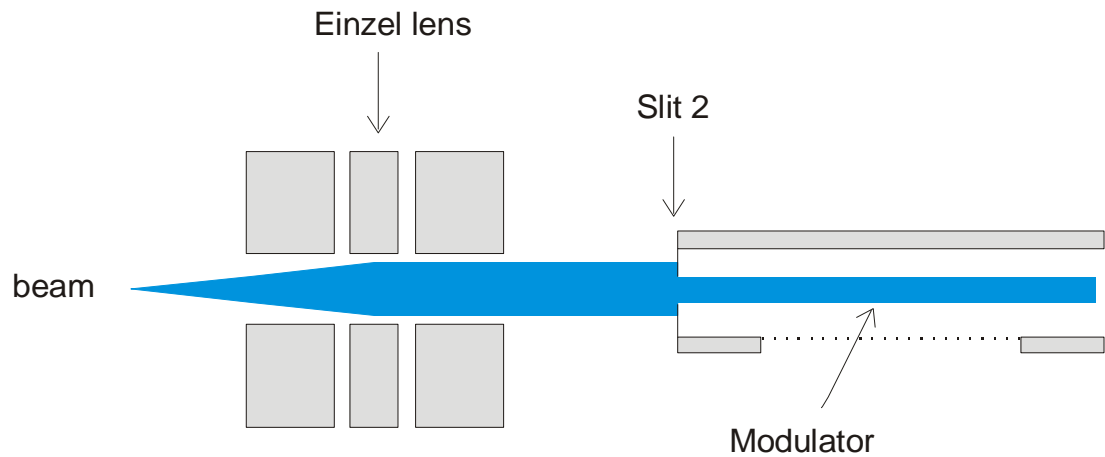


Fig.(4-2): Schematic view of the einzel lens and the modulator of the Ortho-TOF MS. An einzel lens can be described in first approximation as a thin lens. The einzel lens converts the z-component of the ion beam velocity into a spatial spread which can be to some extent compensated (see Fig.(A1_3)).

From ion optics [Wol87] it is well known that an einzel lens can be described in first approximation as a thin lens. The focus point for a thin lens can be calculated from [Wol87]

$$\frac{1}{f} = \frac{1}{l_1} + \frac{1}{l_2} \quad (4_8)$$

Where f is the focal length of the lens, l_1 is the distance between the object and the lens, and l_2 is the distance between the image and the lens. A detailed calculation of the beam diameter D and the divergence of the beam a_2 at the entrance of the modulator is given in Appendix 2. The longer the focal length of the einzel lens, the

smaller the divergence of the ion beam behind the einzel lens. The diameter of the beam at the entrance of the modulator as a function of α_2 is shown in Fig.(A2_2) (see Appendix 2).

From Eq.(4_6) it can be seen that $R_{M_turn} \geq 20000$ when $\alpha_2 \leq 0.05$ rad.

In this case the beam width is larger than 5 mm and the ideal mass resolving Power is lower than 2500. In order to keep the diameter of the beam small enough a slit (slit2) is placed on the way of the beam. The slit (slit2) has a width of 2 mm, so it cuts the ion beam and behind slit2 (in the modulator) the beam has a width of 2 mm. The higher R_{M_turn} is, the more beam is cut, so the poorer the efficiency of the Ortho-TOF MS. Thus, a compromise between the efficiency and R_{M_turn} has to be found. This efficiency is covered in subchapter 4.2.

MCP-detector:

In the Ortho-TOF MS a chevron type MCP-detector is used (see chapter 2.5). Such a detector consists of two micro-channel plates (MCPs). The MCP is characterized by two main geometrical properties: (1) The diameter of the micro-channels D and (2) the bias angle of the micro-channels Θ .

A schematic view of a single channel is shown in Fig.(4-3).

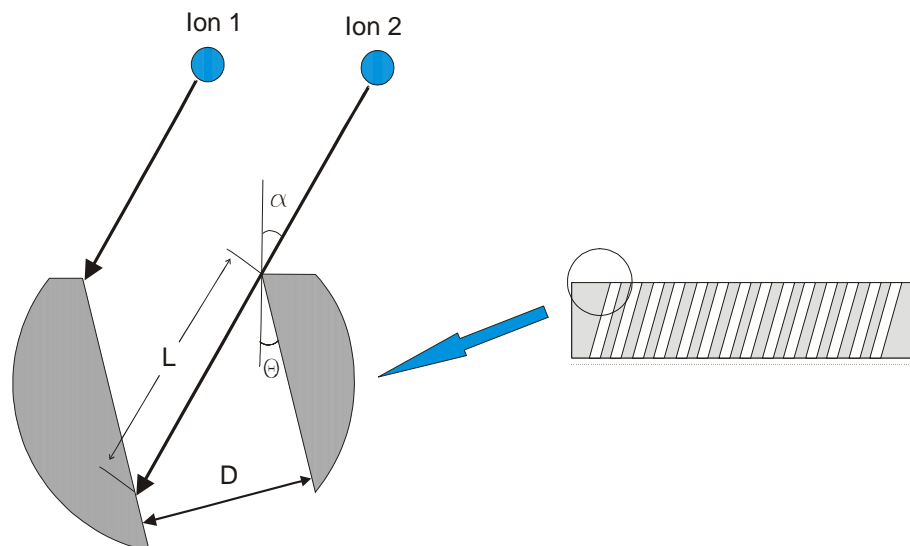


Fig.(4-3): A schematic view of a single channel of the MCP. The MCP is characterized by two main geometrical properties: (1) The diameter of the micro-channels D and (2) the bias angle of the micro-channels Θ . The mass resolving power limit caused by the MCP detector is due to different positions, and hence different times, at which ions strike the detector.

In order to derive the mass resolving power limit caused by the MCP detector, consider two ions, that strike the detector at different positions (Fig.(4-3)), and hence at different times. This time difference Δt_{MCP} can be expressed as follows (see Fig.(4-3)):

$$\Delta t_{MCP} = \frac{D}{\sin(\alpha + \Theta)} * \sqrt{\frac{M}{2K_{ion}}} \quad (4_9)$$

where α is the ion beam incident angle, K_{ion} is the energy of the ions at the MCP and M is the mass of the ions.

The ions hit the MCP-detector at an angle α of about 0.045 Rad.

The bias angle Θ and diameter of the channels D for commercial MCPs range from 5 to 15⁰ and 5 to 15 μm , correspondingly [Pro00,Del00].

The mass resolving power limit due to the MCP-detector can be expressed as follows:

$$R_{M_MCP} = \frac{t}{2\Delta t_{MCP}} \quad (4_{10})$$

Both t and Δt_{MCP} are proportional to \sqrt{M} . Therefore R_{M_MCP} does not depend on the mass of the ion, and remains constant over whole mass range. In Fig.(4-4) the calculated dependence of the limitation imposed by the detector R_{M_MCP} is a function of three parameters: Θ , D and K_{ion} .

For the present Ortho-TOF MS MCPs with the following parameters are used:

$$\Theta = 8^0, D=10 \mu\text{m}, K_{ion}=6000\text{eV}$$

Substituting these values into Eq.(4_9) one obtains a mass resolving power limit imposed by the MCP-detector of 30000.

There are three ways to increase R_{M_MCP} : (1) Choosing of a MCP with a smaller diameter of a micro-channel, (2) choosing of a MCP with a larger bias angle of a micro-channel and (3) increasing the ion energy at the MCP.

In the present Ortho-TOF MS, large rectangular MCPs are used. The assortment of such MCPs on the market is limited to $\Theta = 8-12^0$ and $D=10-15 \mu\text{m}$. The only way to

increase the R_{M_MCP} for these MCPs is to increase the energy of the ions at the MCP. For $K_{ion}=20000\text{eV}$ this gives the limit for the R_{M_MCP} of 65000.

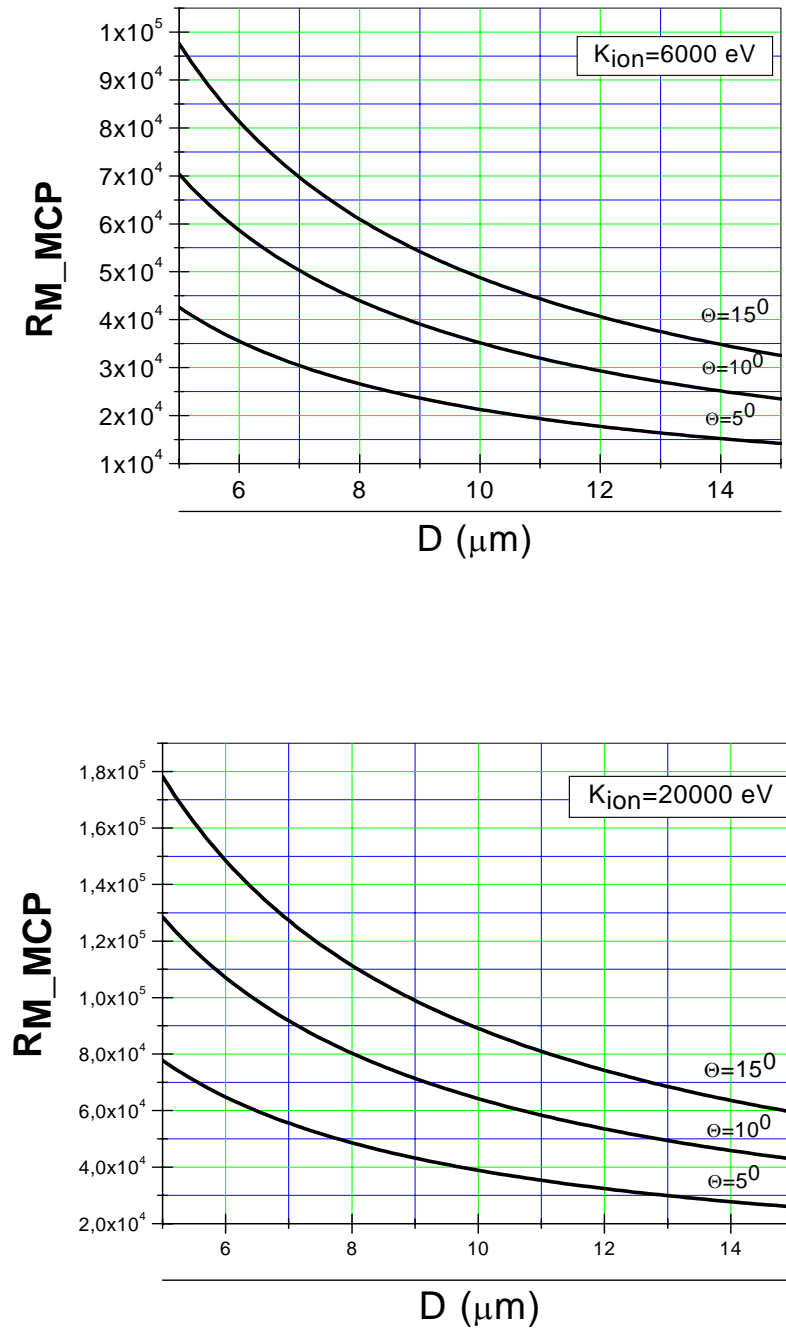


Fig.(4-4): Calculated mass resolving power limit of the Ortho-TOF MS due to the MCP-detector (see Eq.(4_9) and Eq.(4_10)) vs the kinetic energy of the ions K_{ions} . The diameter of the channels and the bias angle of the MCP are D and θ , respectively.

Stability of HV-power supplies:

According to Eq.(1_13) the time-of-flight of the ions in the analyzer depends on the potentials applied to the electrodes of the modulator, accelerating region and reflector. A temporal instability of these potentials causes a time-of-flight spread for ions started at different times and, thus, limits the mass resolving power of the Ortho-TOF MS. The variation of the electrical fields E_1, E_2, E_3, E_4 in Eq.(1_13) gives us the mass resolving power limit $R_{M_p.s.}$ as a function of the voltages U_1, U_2, U_3 and U_4 ($U_1=l_1 E_1, U_2=l_2 E_2, U_3=l_3 E_3$ and $U_4=l_4 E_4$). The mass resolving power limit $R_{M_p.s.}$ is plotted as a function of stability of the potentials in Fig.(4-5) [Zhe00]. One finds that

$$R_{M_p.s.} \cong \frac{U_k}{\Delta U_k} \tag{4_11}$$

where $k=2,3$ or 4 , and

$$R_{M_p.s.} \cong 40 \frac{U_1}{\Delta U_1} \tag{4_12}$$

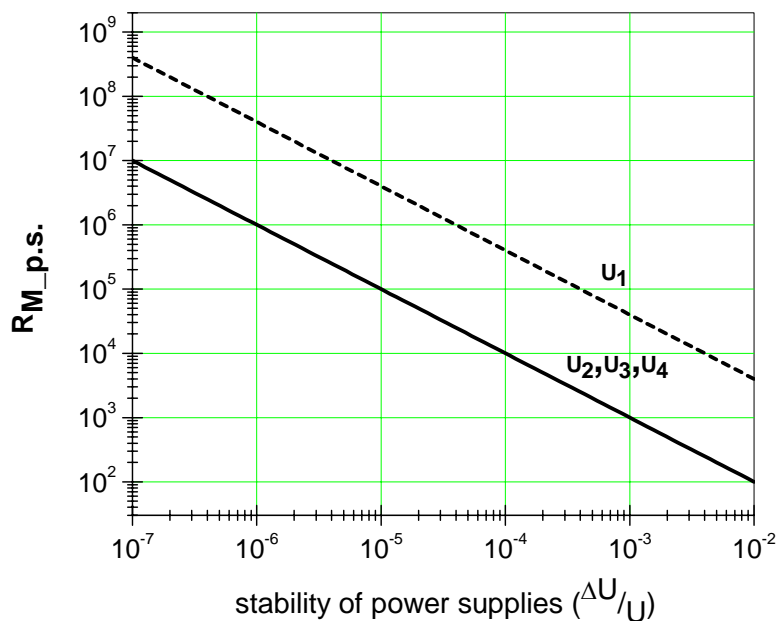


Fig.(4-5): Calculated mass resolving power limit caused by the instability of the power supplies as a function of stability of the potentials of the time-of-flight analyzer of the Ortho-TOF MS [Zhe00]

From Eqs.(4_11) and (4_12) it can be seen that the stability of the power supplies for the pulse extraction voltage U_1 can be 40 times worse than the stability of the power supplies for the accelerating and reflecting voltages U_2 , U_3 and U_4 . The power supplies used presently have the stability about $2 \cdot 10^{-5}$. This value corresponds to a mass resolving power limit $R_{M_p.s}$ of 50000.

Grids:

As has already been mentioned, the time-of-flight analyzer of the Ortho-TOF MS consists of five zones of homogenous field, separated by grids [Zhe00]. From ion optics [Sta59] it is known that the individual cell of such a grid behaves as a lens with a focal length given by

$$f = \frac{2K_0}{E_2 - E_1} \quad (4_13)$$

where K_0 is the kinetic energy of the ion crossing the grid cell, E_1 and E_2 are the electrical field strengths on both sides of the grid. Thus, the grid disturbs the movement of the ions causing a spread in the time-of-flight of the ions. Intensive Monte-Carlo simulation were performed in the work [Zhe00]. In the Monte-Carlo simulation it was assumed that the grids act like an einzel lens with a focus described by Eq.(4_13).

The mass resolving power limit R_{M_grids} is plotted as a function of the grid wire separation in Fig.(4-6).

In the present Ortho-TOF MS grids with a separation of 0,5 mm are used. According to Fig.(4-6) the calculation yields a mass resolving power limit R_{M_grids} of 240000.

In Table 6 a summary of the individual mass resolving power limits described above are presented.

Substituting the values from Table 6 into Eq.(4_1) one can get for R_{M_real} :

$R_{M_real} = 19000$. The measurement performed with lead isotopes (see Fig.(3-15)) gives 20000 for the mass resolving power of the Ortho-TOF MS. The calculated and measured values are in agreement.

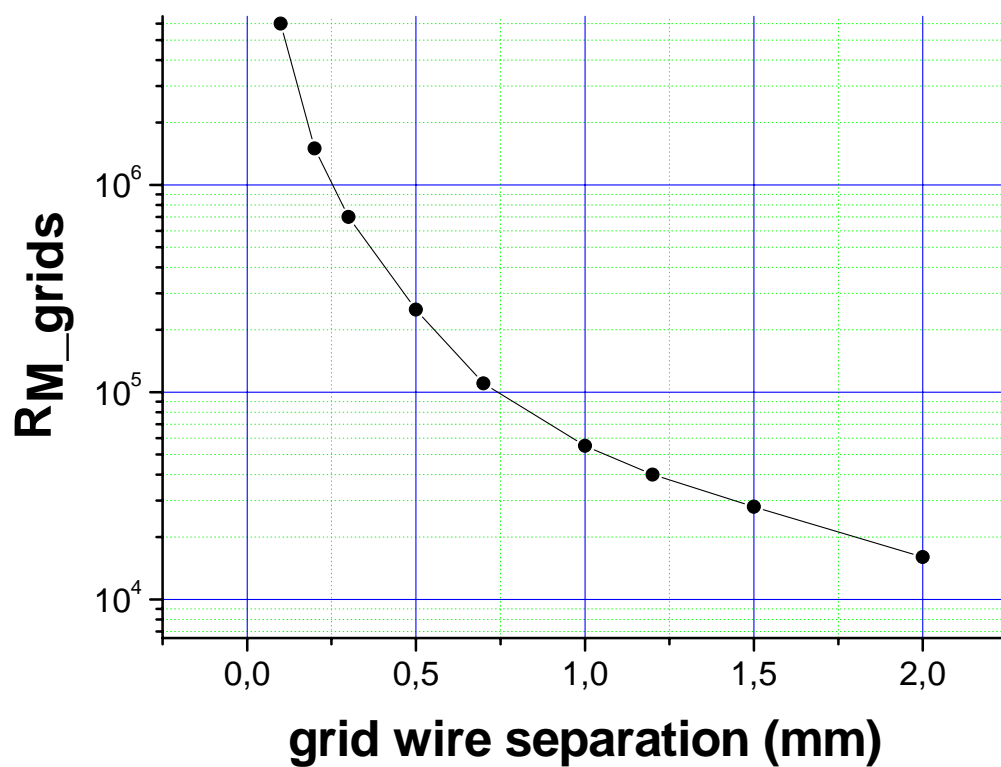


Fig.(4-6): Calculated mass resolving power limit caused by the separation grids vs wire separation. The grid disturbs the movement of the ions causing a spread in the time-of-flight. Intensive Monte-Carlo simulation were performed in the work [Zhe00]. In the Monte-Carlo simulation it was assumed that the grids act like an einzel lens with a focus described by Eq.(4_13).

RM_ideal	RM_turn	RM_MCP	RM_p.s	RM_grids
130000	30000	30000	50000	240000

Table 12: Calculated mass resolving power limitations of the Ortho-TOF MS

4.2 Efficiency

The efficiency of the complete Ortho-TOF MS system can be defined as a ratio of the number of ions, which reach the MCP-detector, to the number of ions, which enter the radio-frequency quadrupole.

The expected efficiency of the complete Ortho-TOF MS system can be calculated as follows:

$$\varepsilon_{exp} = \varepsilon_{RFQ} * \varepsilon_{MCP} * \varepsilon_{grids} * \varepsilon_{inj} \quad (4_14)$$

where ε_{RFQ} is the transmission efficiency of the RFQ, ε_{MCP} is the efficiency of the MCP, ε_{grids} is the transparency of the time-of-flight analyzer (see Fig.(2-8)) and ε_{inj} is the efficiency of the injection of the ions into the modulator (see Fig.(2-10)). A measured ε_{RFQ} amounts to 33%, ε_{MCP} amounts to about 50 % (see Table 4), ε_{grids} can be estimated as $0.9^8 \sim 0.4$ (40%), where 8 in power is the number of the separating grids with the transparency 0.9 (see Fig.(2-8)), ε_{inj} is about 50% (It comes from the geometry of the einzel lens-modulator region). Substituting these values in ε_{exp} one can obtain 3% for ε_{exp} .

4.3 Further improvement of the Ortho-TOF MS

Further improvements of the Ortho-TOF MS lie in increasing the mass resolving power and efficiency of the Ortho-TOF MS.

The main factors limiting the mass resolving power are the turn-around-time, MCP-detector and stability of the power supplies. The stability of the power supplies is the easiest factor to be improved. High voltage power supplies with stability of 2ppm and computer control are available on market. It corresponds to the mass resolving power limit due to instability of the power supplies of about 500000 (see Fig.(4-5)). The increase of the mass resolving power limit due to the turn-around-time can be done by increasing the extraction electric field in the modulator (It leads to reduction of the turn-around-time) or/and by increasing the time-of-flight of the ions. The increase of the time-of-flight of the ions can be realized by lengthening the time-of-flight path (It is not relevant from the point of view of mobility of the Ortho-TOF MS) or by reducing the kinetic energy of the ions in the TOF-analyser. From the practical point of view one can double the extraction field in the modulator and

reduce the kinetic energy of the ions to the half of their present value. It will double the time-of-flight of the ions and increase the mass resolving power limit due to the turn-around-time to 60000. The decrease of the kinetic energy of the ions leads to decrease of the mass resolving power limit due to the MCP-detector to about 21000 (see Eq.(4-9) and Eq.(4-10)). In order to prevent it one should do a post-acceleration of the ions at the MCP-detector. From the practical point of view one can not go higher than 20 eV for the kinetic energy of the ions. It leads to the mass resolving power limit due to the MCP-detector of 46000. These improvements raise the real mass resolving power of the Ortho-TOF MS up to 30000. Further improvements of the mass resolving power require the implementation of MCPs with a smaller diameter of the micro-channel and large bias angle as well as the reduction of the He temperature in the RFQ down to liquid nitrogen temperature. Hence, the maximum reachable mass resolving power of the Ortho-TOF MS amounts to about 37000.

Current efficiency of the Ortho-TOF MS is ~3% (bunch mode). By increasing the transmission of the RFQ one can obtain ~8%. Further increase of the efficiency can be due to increasing the effective surface of the MCPs by utilization of the electrons kicked out from the dead surface of the MCP by the impinging ions (from present 50% up to 70%). The injection efficiency of the ions into the modulator (see Fig.(2-10)) can be also optimized from the present 50% to about 80-90% by implementation of an einzel lens that is able to affect the ion movement in either plane. Thus, 13-15% of total efficiency of the Ortho-TOF MS can be reached at the same mass resolving power.

Chapter 5

Experiment to characterize the SHIPTRAP gas cell with the Ortho-TOF MS

The Ortho-TOF MS is designed to be used for direct mass measurements of short-lived nuclides with half-lives amounting to a few 10 ms. The *on-line* mass measurement of radioactive nuclides is planned to take place at the SHIPTRAP facility at GSI [Dil00,Dil01]. A schematic view of a planned set-up is shown in Fig.(5-1) [Gsi01].

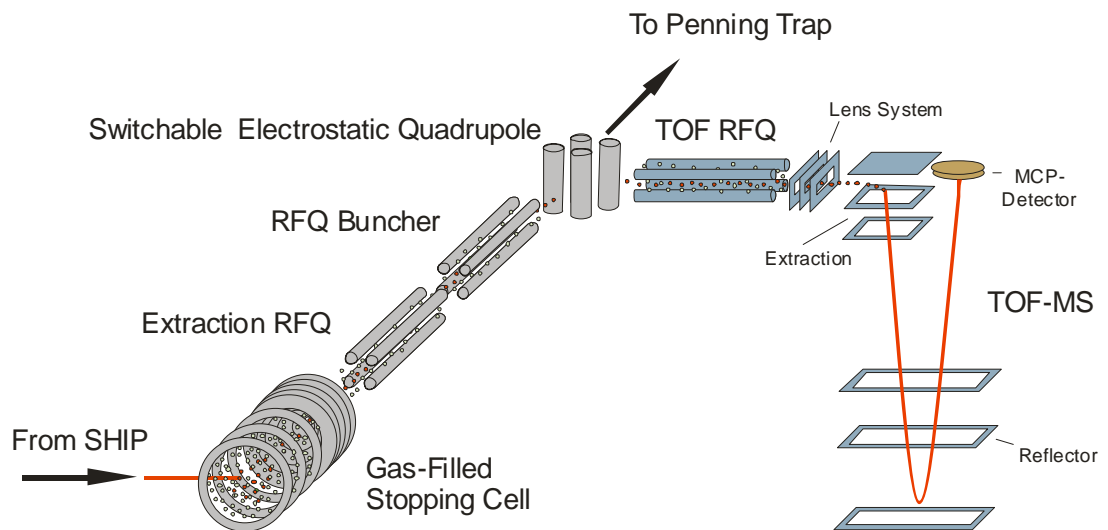


Fig.(5-1): The planned set-up of the coupling of the Ortho-TOF MS to the SHIPTRAP facility. The products of a chosen fusion-evaporation reaction with the kinetic energy ranging from a few 10 MeV/u to a few 100 MeV come from the SHIP [Mün79] into the SHIPTRAP gas cell [Neu]. In the gas cell they are slowed down to the thermal energy of the buffer gas (He). After thermalization they are extracted as singly charged ions from the gas cell and injected into the RFQ buncher. The switchable electrostatic quadrupole can direct the ions either towards the Penning Trap or towards the Ortho-TOF MS [Gsi01].

The fusion-evaporation products from the SHIP [Mün79] enter the SHIPTRAP gas cell [Neu]. In the gas cell they are slowed down to the thermal energy of the buffer gas (He). After thermalization they are extracted out of the gas cell as singly charged ions and injected into the RFQ buncher. A switchable electrostatic quadrupole can direct the ions either towards the Penning Trap or towards the Ortho-TOF MS. The key component of the set-up is the gas cell. The gas cell is subject of the PhD thesis of J. Neumayr (LMU München) [Neu]. The gas cell can be an origin of various positively charged compounds due to the interaction of the incoming products with the buffer gas and the impurities present in the gas cell. Thus, a detailed investigation of the parameters of the gas cell and the chemical processes in the gas cell should be carried out. An experiment dedicated to such an investigation was performed in September 2003 in Garching. It was a joint experiment of our group and a group of Prof. Habs from Garching. The goals of the experiment were:

1. Test the coupling of the Ortho-TOF MS to the SHIPTRAP gas cell
2. Characterization of the gas cell with the Ortho-TOF MS:
 - a. Measurement of the efficiency of the gas cell
 - b. Study of the chemical reactions occurring in the gas cell

The schematic view of the experimental set-up is shown in Fig.(5-2). A photo of the experimental set-up is presented in Fig.(5-3).

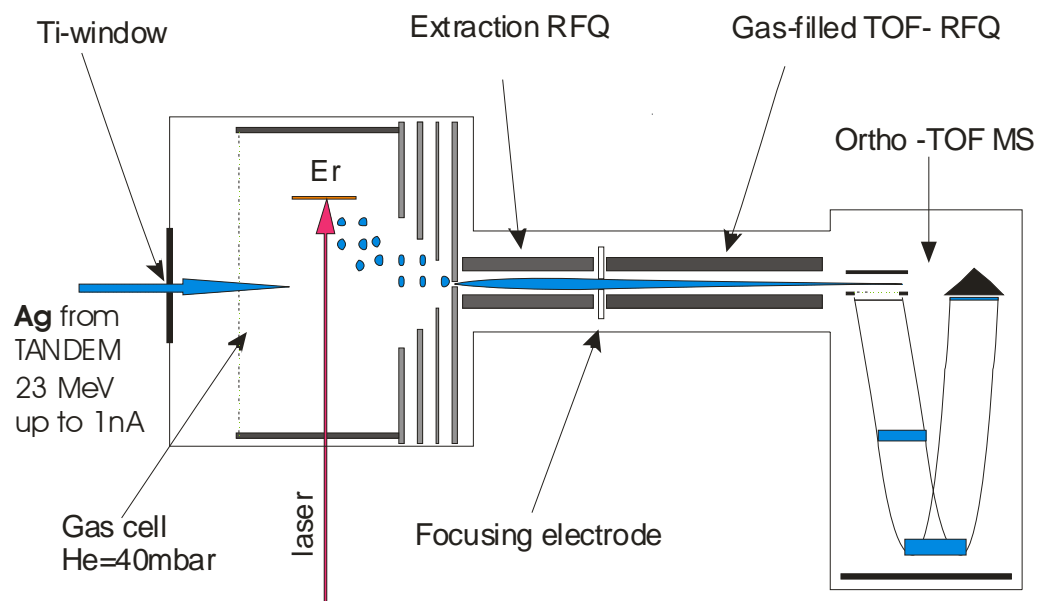


Fig.(5-2): The set-up used for a characterization of the SHIPTRAP gas cell. The experiment was divided into two parts: (1) *off-line* test with the Er-laser source and (2) *on-line* test with a primary Ag-beam. The beam current was varied up to 1 nA.

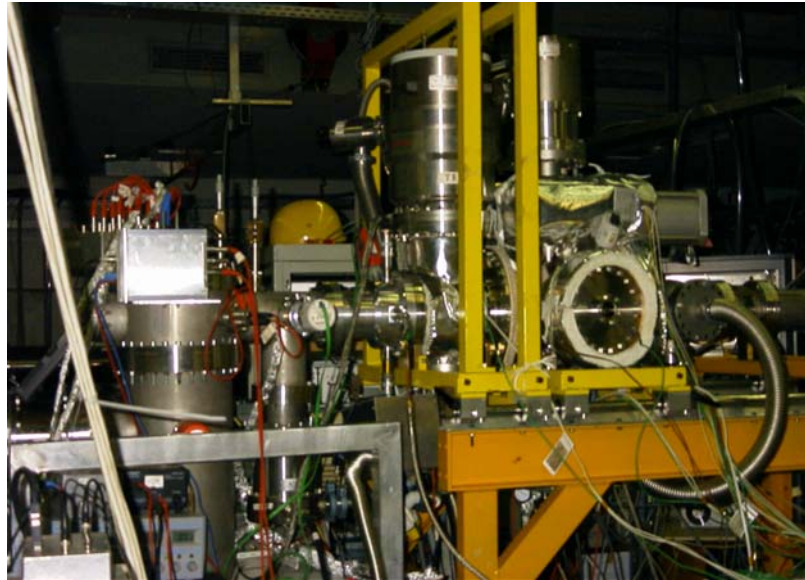


Fig.(5-3): A photo of the experimental set-up used for the characterization of the SHIPTRAP gas cell

The experiment consisted of two parts: (1) *off-line* test with the Er-laser source and (2) *on-line* test with a primary Ag-beam.

5.1 Experiment with the Er-laser source

The goal of this part was a test of the coupling of the Ortho-TOF MS to the gas cell. A thin foil of Er with natural isotope ratios was placed in the gas cell. A laser beam was shot onto the foil, evaporating Er. The Er got ionized, extracted out of the gas cell and injected into the Ortho-TOF MS and mass-analyzed. The He pressure in the gas cell was maintained at 40 mbar. Two different mass spectra were acquired:

1. before cleaning of the gas cell
2. after 30 minute cleaning of the gas cell with a getter element placed in the gas cell

These two spectra are shown in Fig.(5-4) and Fig.(5-5).

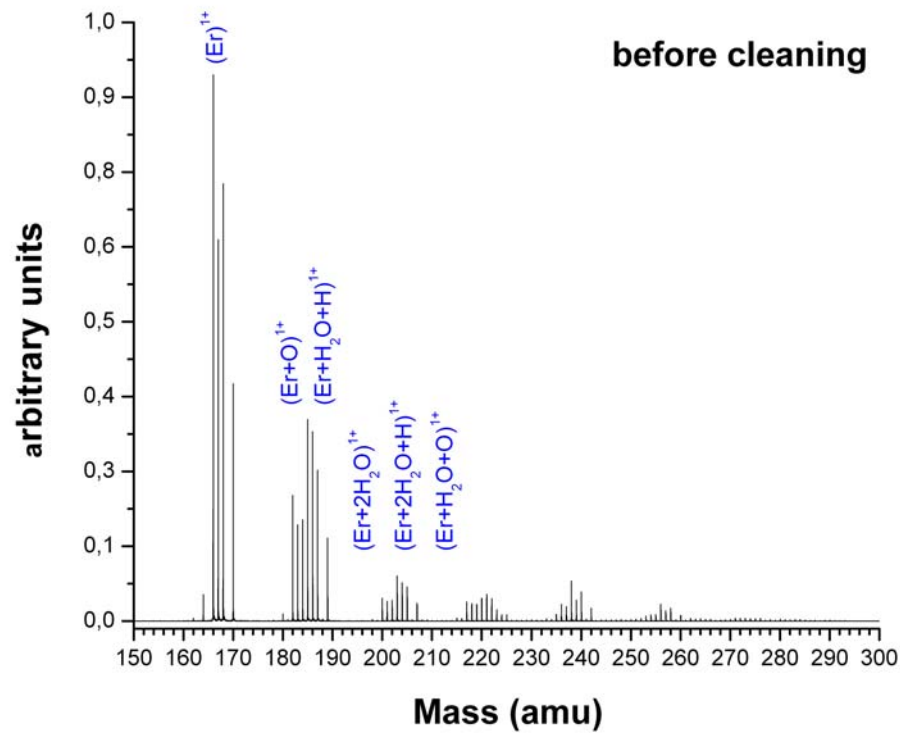


Fig.(5-4): Mass spectrum of Er ions and compounds acquired before the cleaning of the gas cell with a getter element placed in the gas cell.

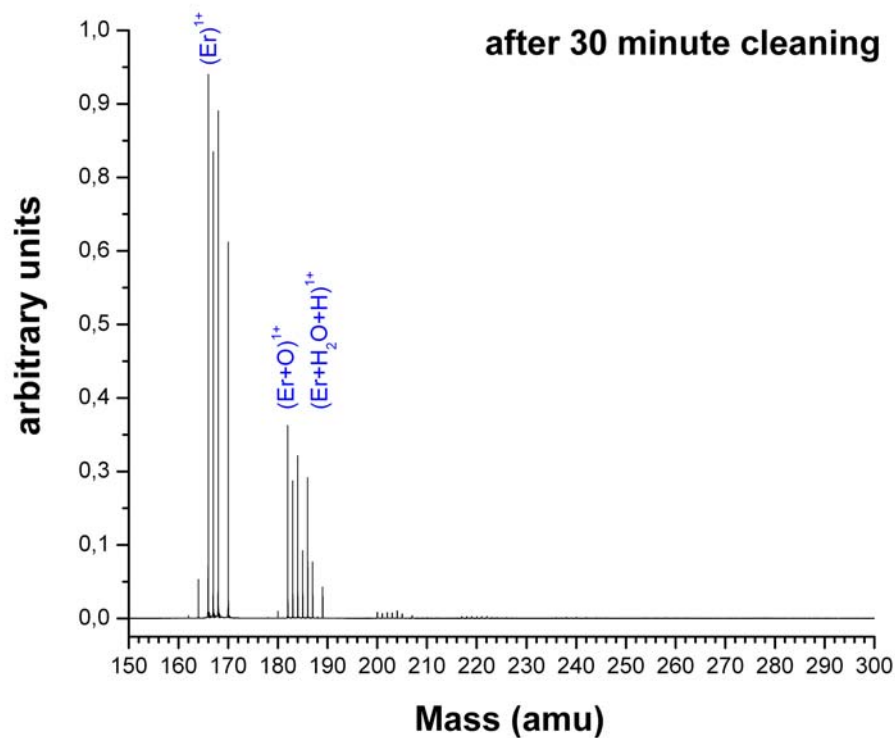


Fig.(5-5): Mass spectrum of Er acquired after the 30 min. cleaning of the gas cell with a getter element placed in the gas cell

As can be seen from Fig.(5-4) there is much water in the uncleaned gas cell. The water reacts with the Er-ions and forms cluster ions. In Fig.(5-4) six water groups are present:

Group 1: bare Er-isotopes ($^{162}\text{Er}^{1+}$, $^{164}\text{Er}^{1+}$, $^{166}\text{Er}^{1+}$, $^{167}\text{Er}^{1+}$, $^{168}\text{Er}^{1+}$, $^{170}\text{Er}^{1+}$)

the abundance of the isotopes is consistent with the natural abundance.

Group 2: $(\text{Er}+\text{O})^+$ and $(\text{Er}+\text{H}_2\text{O}+\text{H})^+$

Group 3: $(\text{Er}+\text{H}_2\text{O}+\text{O})^+$, $(\text{Er}+2\text{H}_2\text{O}+\text{H})^+$, $(\text{Er}+2\text{H}_2\text{O})^+$

.....

Group 6: $(\text{Er}+5\text{H}_2\text{O}+\text{H})^+$, $(\text{Er}+5\text{H}_2\text{O})^+$ and $(\text{Er}+4\text{H}_2\text{O}+\text{O})^+$

The fraction of pure Er-isotopes to the fraction of the Er-isotopes bound with the water is measured to be around 0.8. About 45% of Er is extracted from the gas cell as monoatomic ions whereas 55% of it reacts with the water.

After 30 minute of cleaning of the gas cell with a getter element all water groups, except for group 2, vanished, and only 30% of Er reacts with water.

This means that the gas cell should be cleaned from the water before it is used at *on-line* measurement. Otherwise, water molecules in the gas cell react with the ions of interest and the efficiency of the gas cell for monoatomic ions of interest drops.

A getter element is a very efficient tool for the cleaning of the gas cell from water. It takes only a couple of hours in order to reduce the water concentration in the buffer gas down to an acceptable level.

5.2 On-line experiment with $^{107}\text{Ag}^{17+}$ -beam provided from a tandem accelerator

5.2.1 Efficiency of the gas cell vs the intensity of the Ag-beam

A primary beam of $^{107}\text{Ag}^{17+}$ ions with kinetic energies ranging from 20 MeV to 30 MeV provided by the tandem accelerator entered the gas cell through a 3,5 μm Ti-window, was stopped in the gas cell, extracted from the gas cell and injected into the Ortho-TOF MS (Fig.(5-2)). The TOF-spectra of Ag ions were acquired. The number of the ions injected into the gas cell (up to $6 \cdot 10^9$) (see the in-set in Fig.(5-7)) was measured with a Si-detector placed in front of the gas cell. The number of the ions extracted from the gas cell (see in-set in Fig.(5-7)) was measured with the Ortho-TOF MS.

The number of the $^{107}\text{Ag}^{1+}$ -ions extracted from the gas cell and detected by the MCP-detector of the Ortho-TOF MS vs the number of the $^{107}\text{Ag}^{17+}$ -ions entering the gas cell is shown in Fig.(5-6). The absolute efficiency of the gas cell is a ratio of the number of the ions extracted from the gas cell to the number of the ions entering the gas cell (see Fig.(5-7)). If the absolute efficiency of the gas cell did not depend on the number of $^{107}\text{Ag}^{17+}$ -ions entering the gas cell the measured curve in Fig.(5-6) would be a straight line (blue line in Fig.(5-6)). But it because of space charge effects comes to saturation. The absolute efficiency of the gas cell as a function of the number of the incoming $^{107}\text{Ag}^{17+}$ -ions is presented in Fig.(5-7).

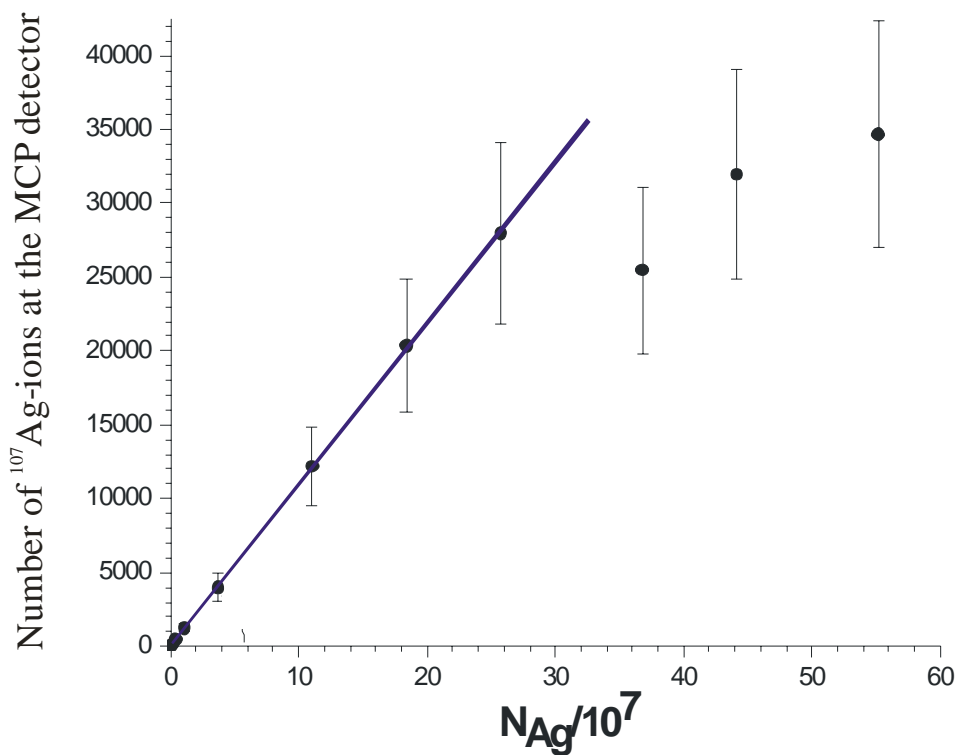


Fig.(5-6): Measured number of the $^{107}\text{Ag}^{1+}$ -ions extracted from the gas cell and detected by the MCP-detector of the Ortho-TOF MS vs the number of the $^{107}\text{Ag}^{17+}$ -ions entering the gas cell. If the absolute efficiency of the gas cell did not depend on the number of $^{107}\text{Ag}^{17+}$ -ions entering the gas cell the measured curve would be a straight line (blue curve in the Figure).

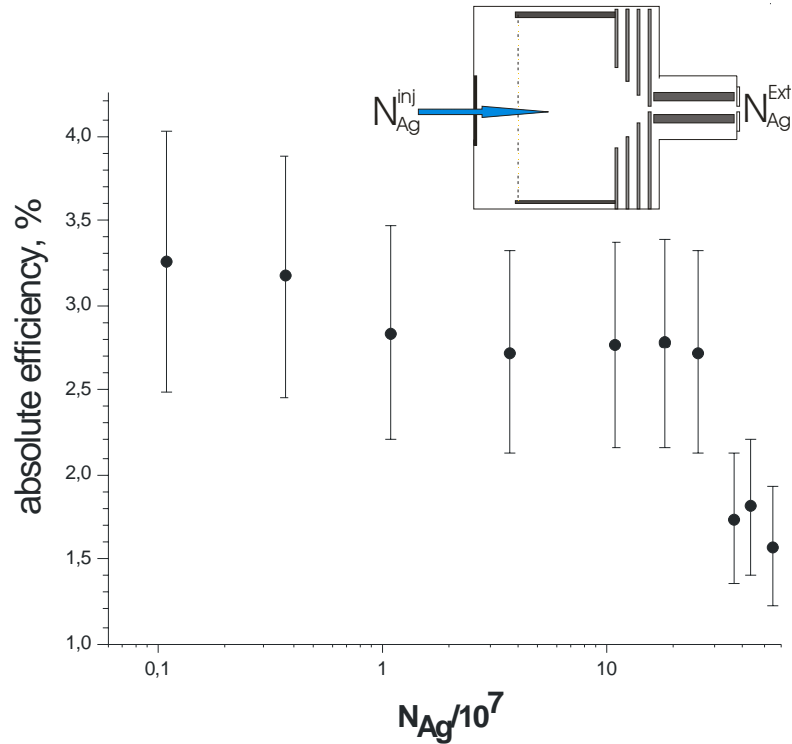


Fig.(5-7): Measured absolute efficiency of the gas cell as a function of the number of the $^{107}\text{Ag}^{17+}$ -ions entering the gas cell. The absolute efficiency of the gas cell amounts to 3% at low intensity of the Ag-beam. At $N_{Ag} \sim 3 \cdot 10^8$ ions per second the absolute efficiency decreases by a factor of 2.

It can be seen that the absolute efficiency of the gas cell amounts to 3% at low intensity of the Ag-beam. From N_{Ag} of about $3 \cdot 10^8$ ions per second the absolute efficiency starts to decrease. Further optimizations lead to the absolute efficiency of about 4%.

The following effects can limit the absolute efficiency of the gas cell: (1) Space charge of Ag-ions in the TOF-RFQ, (2) Space charge of Ag-ions in the extraction-RFQ, (3) space charge of He-ions, created in the stopping volume of the gas cell during the stopping of the primary beam (see Fig.(5-9)) and (4) space charge of Ag-ions in the funnel structure of the gas cell (see Fig.(5-9)). The different contributions will be discussed further.

Space charge of Ag-ions in the TOF-RFQ

In the TOF-RFQ two forces affect the motion of the ions: (1) Pseudo-potential U_{eff} (see subchapter 1.2.2) that pushes the ions toward the axis of the TOF-RFQ and (2) the Coulomb force, occurring due to space charge of the ions, which tends to push the ions away from the axis of the TOF-RFQ.

In Fig.(5-8) a schematic view of the Ag-beam in the TOF-RFQ is shown. The RFQ-rods and the Skimmer 1 are omitted.

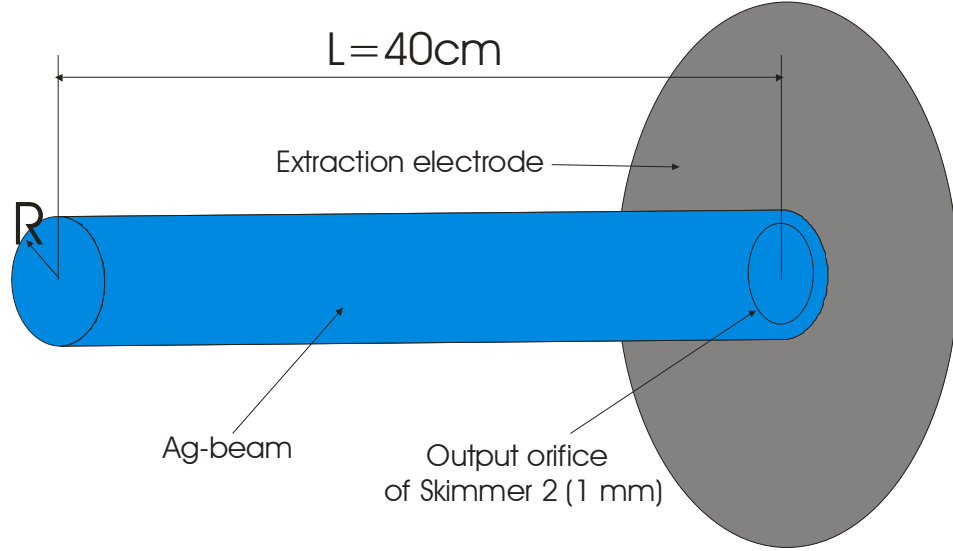


Fig.(5-8): Schematic drawing of the Ag-beam in the TOF-RFQ. The RFQ-rods and the Skimmer 1 are omitted. In the TOF-RFQ two forces affect the ions: (1) Pseudo-potential U_{eff} (see chapter 1.2.2) that pushes the ions toward the axis of the TOF-RFQ and (2) the Coulomb force, occurring due to space charge of the ions, which tends to push the ions away from the axis of the TOF-RFQ.

In this drawing, L is the length of the RFQ, R is the radius of the Ag-beam in the RFQ. The radius of the output orifice r is equal to 1mm. The condition for the limit of the RFQ-transmission can be derived as follows: The radius of the Ag-beam R should be larger than the radius r of the output orifice, in other words, $R > 1\text{mm}$. The pseudo-potential U_{eff} is expressed by Eq.(1_22). Taking into account that $\Omega^2 r^2 \gg 1$ for 10^{-2} mbar of He-pressure in the RFQ, $V_{rf} = 160\text{V}$, $M = 1,6 \cdot 10^{-25}\text{kg}$, $Q = 1,6 \cdot 10^{-19}\text{As}$, $\Omega = 10^7\text{s}^{-1}$, $R_0 = 3,65 \cdot 10^{-3}\text{m}$, $L = 0,4\text{m}$ one gets

$$U_{eff} = 1,4 \cdot 10^6 R^2 [\text{V}] \quad (5_1)$$

where R is measured in m . The potential U_{space_charge} , created by space charge of the Ag-ions can be expressed as follows (Gauss theorem for electrostatic field; cylinder case; the charge is distributed homogeneously in the cylinder [Tol00]):

$$U_{space\ charge} = -\frac{nQ}{4\epsilon_0\pi L} = 3,6 \cdot 10^{-9} n [\text{V}] \quad (5_2)$$

where n is the number of the Ag-ions in the RFQ, ϵ_0 is the permittivity of vacuum.

n can be obtained from the following expression:

$$U_{eff} = U_{space\ charge} \Big|_{R=10^{-3}\ m} \quad n = 3.8 * 10^8\ ions \quad (5_3)$$

where $R=10^{-3}\ m$ is the diameter of Skimmer 2 of the TOF-RFQ. Taking into account that the time-of-flight of the Ag-ions through the TOF-RFQ amounts to 2 ms one can obtain the following limit for the number of Ag-ions entering the gas cell (N_{Ag}):

$$N_{Ag} = n \left[\frac{ions}{2ms} \right] * \frac{1000[ms]}{2[ms]} = 2 * 10^{11} \frac{ions}{s} \quad (5_4)$$

From Fig.(5-7) it can be seen that the TOF-RFQ limit for the intensity of the Ag-beam lies much higher than the limit measured in the experiment.

Space charge of Ag-ions in the extraction-RFQ

The calculation of the space charge effect for the extraction-RFQ is similar to that for the TOF-RFQ. With the appropriate parameters $V_{rf} = 75V$, $R_0=5*10^{-3}\ m$, $\Omega=6*10^6s^{-1}$, $R=2*10^{-3}m$ (aperture of the Skimmer1), $L=0,1m$ one obtains from Eq.(1_22) for the pseudo-potential (U_{eff}):

$$U_{eff} = 1V \quad (5_5)$$

The potential U_{space_charge} , created by space charge of the Ag-ions can be derived from Eq.(5_2):

$$U_{space_charge}=1,44*10^{-8}\ n\ [V] \quad (5_6)$$

The length of the extraction-RFQ is four times shorter than that of the TOF-RFQ. Taking into account that the gas pressure in both RFQs was almost equal, the time-of-flight through the extraction-RFQ can be estimated to be around 0.5 ms. Thus, one can obtain the following limit for the number of Ag-ions entering the gas cell (N_{Ag}):

$$N_{Ag} = 1.4 * 10^{11} \frac{ions}{s} \quad (5_7)$$

This is much larger than the measured quantity.

Space charge of He-ions, created in the stopping volume of the gas cell during the stopping of the primary beam

The Ag-ions entering the gas cell ionize the buffer gas, creating pairs of electrons and He-ions along the stopping path. An external electrical field E_{ext} is applied along the axis of the gas cell in order to drag the Ag-ions towards the nozzle of the gas cell (see Fig.(5-9)). Since the electrons are much lighter than the He-ions they reach the entrance electrode of the gas cell much faster than the He-ions reach the first funnel electrode. Thus, in the volume of the gas cell a cloud of space charge of He-ions is formed that give rise to an electrical field $E_{space\ charge}$ directed oppositely to the applied field E_{ext} . The higher the intensity of the Ag beam the stronger this field $E_{space\ charge}$. At a certain Ag beam intensity the field $E_{space\ charge}$ completely compensates the field E_{ext} , and the extraction time of the Ag-ions becomes much longer. The probability for ions of interest to be neutralized becomes higher. As a result, the efficiency of the gas cell drops. Quantitative calculation of the field $E_{space\ charge}$ at which the compensation takes place is based on [Huy02].

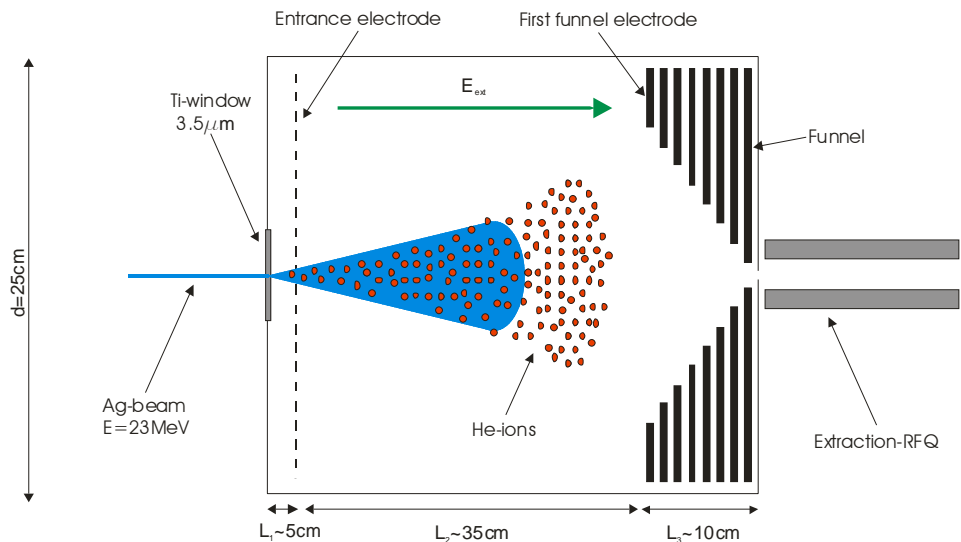


Fig.(5-9): Stopping of the Ag beam in the gas cell. The Ag ions entering the gas cell ionize the buffer gas creating pairs of electrons-He-ions along the stopping path. An external electrical field E_{ext} is applied along the gas cell in order to drag the Ag-ions towards the nozzle of the gas cell. In the volume of the gas cell occurs a cloud of space charge due to He ions that creates an electrical field $E_{space\ charge}$ oppositely directed to E_{ext} . At a certain Ag beam intensity the $E_{space\ charge}$ can compensate the E_{ext} , the extraction time of the Ag-ions becomes much longer.

Let L_1 , L_2 and L_3 be the distances between the Ti-window and the entrance electrode, the length of the stopping volume of the gas cell, the length of the funnel, respectively, d is the diameter of the gas cell. The electric field strength $E_{space\ charge}$ can be obtained from the following formula (see Appendix 4):

$$E_{space\ charge} = 1.8 * 10^{-2} (N_{Ag})^{\frac{1}{3}} \left[\frac{V}{m} \right] \quad (5_8)$$

where N_{Ag} is the number of the ions of the incoming beam.

In the on-line test a field strength E_{ext} of 500 V/m was used. Making E_{ext} equal to $E_{space\ charge}$ (mutual compensation of both fields) one can obtain the number of the Ag^{1+} -ions N_{Ag}^{comp} needed for creating the compensating field:

$$N_{Ag}^{comp} = 2 * 10^{13} \left[\frac{ions}{s} \right] \quad (5_9)$$

The obtained value is much larger than the measured one (see Fig.(5-7)) which amounts to $\sim 10^9$ Ag-ions per second. It can be concluded that the space charge due to the ionization of He in the gas cell does not constrain the efficiency of the gas cell.

Space charge of Ag-ions in the funnel structure of the gas cell

The funnel with the nozzle and a part of the extraction-RFQ is shown schematically in Fig.(5-10).

The aperture of the funnel electrodes amounts to 20 cm at the beginning of the funnel and to 0.1 cm at the end of the funnel. The diameter of the nozzle d is equal to 0.6 mm, L_3 is the length of the funnel and equal to 10 cm, D is the distance between two adjacent rings of the funnel. The funnel region can be divided into two regions with respect to the ion movement. In [Neu] a velocity distribution of the He gas in the funnel region is presented. It can be seen that over almost the full funnel length the ions are dragged towards the nozzle by the DC-electrical field applied along the funnel rings. Only at a distance of 3-4 mm from the nozzle the velocity of the He-flow becomes high enough in order to speed up the ions significantly and extract them through the nozzle out of the gas cell into the extraction-RFQ.

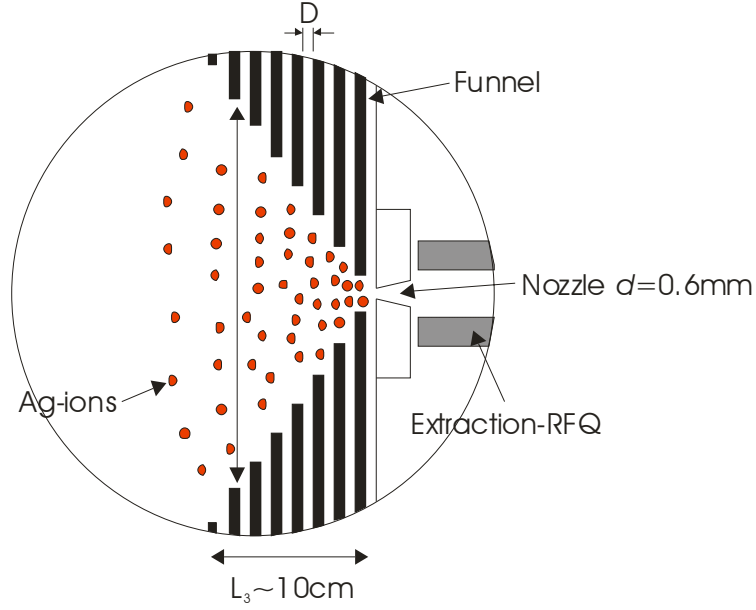


Fig.(5-10): Schematic figure of the funnel structure of the gas cell with the nozzle and a part of the extraction-RFQ. The aperture of the funnel electrodes amounts to 20 cm at the beginning of the funnel and to 0.1 cm at the end of the funnel. The diameter of the nozzle d is equal to 0.6 mm, L_3 is the length of the funnel and equal to 10 cm, D is the distance between two adjacent rings of the funnel.

There are two “bottle necks” for the Ag-ions with respect to space charge effects. The first one is the region at the end of the funnel where the density of the Ag-ions is the highest in the funnel. The aperture R in this region amounts to ~ 1.5 mm. The second one is the region at the beginning of the nozzle where the He flow takes the Ag-ions and guides them through the nozzle. The space charge effect of the Ag-ions in the first region is estimated similarly to that of the extraction- and TOF- RFQs.

$$U_{eff} = U_{space\ charge} \quad (5_{-10})$$

The pseudo-potential U_{eff} for a funnel structure without gas is taken from [Tol00], the correction for a funnel structure with gas is performed in [Koz99].

$$U_{eff} = \frac{QV_{rf}^2}{16Mf^2D^2} * \frac{4\pi^2 f^2 \tau^2}{1 + 4\pi^2 f^2 \tau^2} \quad (5_{-11})$$

Definition of the parameters in Eq.(5_11) is given in chapter 1.2.2 and in Fig.(5-14). Values describing the conditions in the on-line experiment are $V_{rf}=80V$, $f=700kHz$, $M \approx 1.7 \cdot 10^{-25} kg$, $\tau = M \cdot k / Q$, where k is the mobility of the Ag-ions. For He at 40 mbar

$k \approx 0,057 \text{ m}^2/(\text{Vs})$. Thus, $\tau = 5,7 * 10^{-8} \text{ s}$, $4\pi^2 f^2 \tau^2 = 0,06$. Substituting the numerical values of the parameters in Eq.(5_11) one obtains the following for the U_{eff} :

$$U_{eff} = 46V \tag{5_12}$$

From Eq.(5_2), by substituting numerical values for ϵ_0 , π , Q and proper numerical value for L , and designating n as N_{Ag} , $U_{space\ charge}$ is obtained:

$$U_{space\ charge} = 7,2 * 10^{-10} N_{Ag} \text{ [V]} \tag{5_13}$$

Setting Eq.(5_12) equal to Eq.(5_13) one can obtain $N_{Ag} = 6,4 * 10^{10}$ ions per second. This is the maximum number of the Ag-ions that can be guided through the funnel per second.

In the nozzle region (see Fig.(5-11)) the Ag-ions are not confined by the pseudo-potential any longer. Due to the space charge repulsion the Ag-ions gain a velocity component in the direction perpendicular to the axis of the nozzle. If the time-of-flight of the Ag-ions through the nozzle, which is defined by the velocity of the He flow in the nozzle, is longer than the time-of-flight of the Ag-ions from the axis towards the wall of the nozzle, the Ag-ions will hit the wall and get lost. In the following treatment, the collisions with the He molecules are not taken into account. The collisions decrease the transverse velocity of the Ag-ions ($V_{space\ charge}$) that weakens the effect of the space charge.

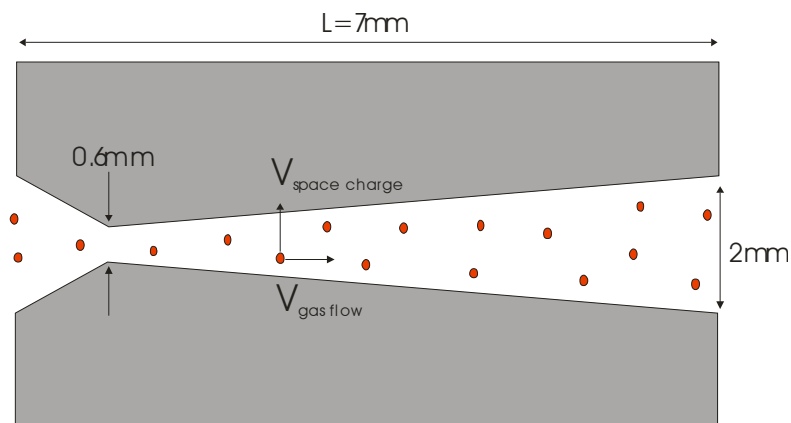


Fig.(5-11): Movement of the Ag-ions through the nozzle of the gas cell. the Ag-ions are not confined by the pseudo-potential U_{eff} any longer. Due to the space charge repulsion the Ag-ions gain a velocity component in the direction perpendicular to the axis of the nozzle. If the time-of-flight of the Ag-ions through the nozzle is longer than the time-of-flight of the Ag-ions from the axis towards the wall of the nozzle, the Ag-ions will hit the wall and get lost.

The time-of-flight of the Ag-ions through the nozzle t_1 can be estimated as follows:

$$t_1 = \frac{L}{V_{gas\ flow}} = \frac{7 * 10^{-3} [m]}{1000 [m/s]} = 7 * 10^{-6} s \quad (5_14)$$

Since the Ag-ions are spread out over the whole width of the nozzle and, therefore, gain different velocities due to space charge repulsion, an estimation of the time-of-flight towards the wall of the nozzle t_2 can be made only roughly. The flight path towards the wall L_{wall} can be estimated to be approximately 0,5 mm. The space charge potential $U_{space\ charge}$ created by the Ag-ions moving with the velocity of He-flow is derived from Eq.(5_2).

$$U_{space\ charge} \approx 10^{-12} N_{Ag} \text{ [V]} \quad (5_15)$$

t_2 can be expressed as follows:

$$t_2 = \frac{2L_{wall}}{v_{space}} = \frac{2L_{wall}}{\sqrt{\frac{2QU_{space\ charge}}{M}}} \approx \frac{1}{\sqrt{N_{Ag}}} \text{ [s]} \quad (5_16)$$

where v_{space} is the transverse velocity gained by the ions at the wall of the nozzle due to space charge repulsion. Making t_1 equal to t_2 one obtains $N_{Ag}=2*10^{13}$ Ag-ions per second, at which a drop in the efficiency occurs. This estimate of N_{Ag} is very rough. The number could differ from the obtained result by one order of magnitude in each direction. In order not to underestimate the result $N_{Ag}>10^{12}$ is taken as the output of the calculation. In Table 13 the results of the calculation of N_{Ag} for the four cases considered in this chapter are shown.

Possible limit of the efficiency	The maximum transmission capacity
Space charge of He-ions in the stopping volume of the gas cell	$\sim 2 * 10^{13}$
Space charge of the Ag-ions in the funnel structure	$\sim 6.4 * 10^{10}$
Space charge of the Ag-ions in the nozzle	$> 10^{12}$

Transmission limit of the extraction-RFQ	$\sim 1.4 \cdot 10^{11}$
Transmission limit of the TOF-RFQ	$\sim 2 \cdot 10^{11}$

Table 13: Calculated maximum transmission capacity of the components of the set-up. all considered causes of the efficiency limitation lie above the measured value, which amounts to a few 10^9 Ag-ions/s entering the gas cell. Since such calculations are not of high accuracy (especially for the nozzle and stopping region), one can not say unambiguously which considered component of the gas cell limits the efficiency. The most probable origin of the efficiency limit seems to be the funnel-extraction-RFQ tandem.

From Table 13 it can be seen that all considered causes of the efficiency limitation lie above the measured value, which amounts to a few 10^9 Ag-ions/s entering the gas cell (see Fig.(5-7)). The efficiency limit due to space charge of He-ions in the stopping volume of the gas cell is by four order of magnitude larger than the measured one. Thus, this is hardly a cause of the efficiency limit. The TOF-RFQ is the least probable cause of the efficiency limit because it is situated behind all components considered in Table 14. The most probable origin of the efficiency limit seems to be the funnel-extraction-RFQ tandem.

5.2.2 Study of the chemical reactions, occurring in the gas cell

An interaction of the ions of the primary beam with the neutrals and ions of different species (further impurities) present in the buffer gas can lead to a substantial decrease in the efficiency of the gas cell. From the knowledge of the impurities one can make a conclusion on the origin of the impurities as well as how important each particular kind of impurity is for the efficiency of the gas cell. Since the impurities are mainly neutral, they should be ionized in order to investigate them with the Ortho-TOF MS. In this experiment a discharge source, which was placed in the gas cell, was used. A mass-spectrum acquired in a presence of the primary beam and the discharge source is shown in Fig.(5-12).

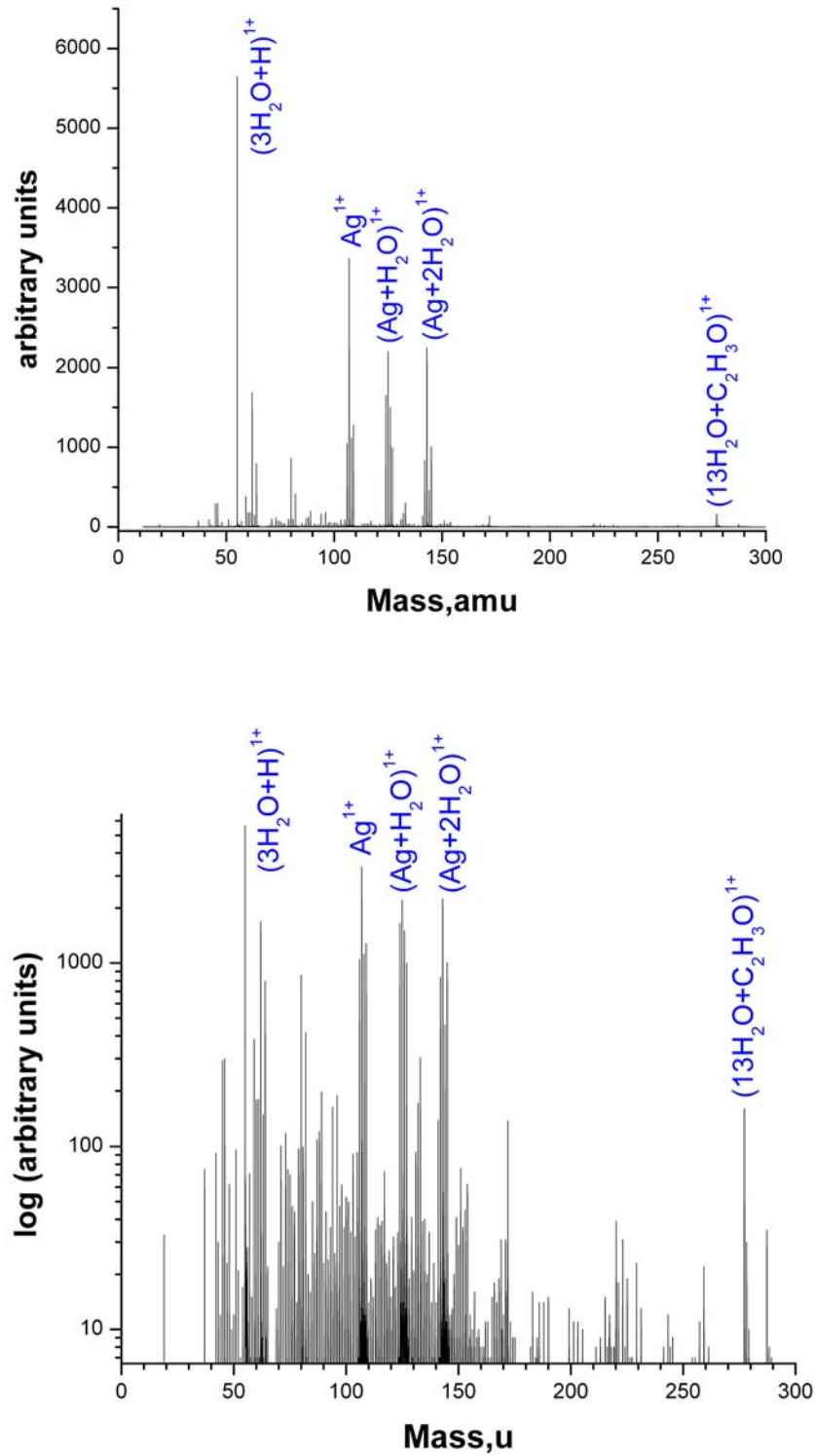


Fig.(5-12): A measured mass-spectrum of the ^{107}Ag - beam acquired in a presence of the discharge source

The nuclides present in the mass-spectrum are listed in Table 14. The assignment of the compounds in the Table was made from the determination of their exact masses, as well as from the isotopic abundances of the compound constituents.

Nuclide	Measured mass, amu	Table mass[Nuc00], amu
$(\text{H}_2\text{O}+\text{H})^+$	19.0198(33)	19.0178404
$(2\text{H}_2\text{O}+\text{H})^+$	37.0289(29)	37.0284044
$(\text{C}_3\text{H}_6)^+$	42.0420(27)	42.0464014
$(\text{C}_2\text{H}_3\text{O})^+$	43.0195(27)	43.0178404
$(\text{C}_2\text{H}_3\text{O}+\text{H})^+$	44.0210(33)	44.0256654
$(\text{C}_2\text{H}_3\text{O}+2\text{H})^+$	45.0337(25)	45.0334904
$(\text{CO}+\text{H}_2\text{O})^+$	46.0035(25)	46.0049294
$(\text{CNH}+\text{H}_2\text{O}+\text{H})^+$	46.0295(25)	46.0287384
$(\text{N}+2\text{OH})^+$	48.0080(24)	48.0080024
$(\text{O}_2+\text{H}_2\text{O})^+$	50.001(2)	49.9998434
$(3\text{OH})^+$	50.9998(23)	51.0076684
$(\text{CH}_3+2\text{H}_2\text{O})^+$	51.0445(23)	51.0440544
$(3\text{OH}+\text{H})^+$	52.0091(23)	52.0154934
$(3\text{H}_2\text{O}+\text{H})^+$	55.039(2)	55.0389684
$(\text{C}_3\text{H}_6+\text{OH})^+$	59.0487(17)	59.0491404
$(\text{CO}+\text{O}_2)^+$	59.9838(18)	59.9841934
$(\text{C}_3\text{H}_6+\text{H}_2\text{O})^+$	60.0597(17)	60.0569654
$(\text{C}_2\text{H}_3\text{O}+\text{H}_2\text{O})^+$	61.0287(16)	61.0284044
$(\text{CO}_2+\text{H}_2\text{O})^+$	61.9950(15)	61.9998434
$(\text{C}_2\text{H}_3\text{O}+\text{H}_2\text{O}+\text{H})^+$	62.0416(16)	62.0362294
$(\text{CO}_2+\text{H}_2\text{O}+\text{H})^+$	62.9976(20)	63.0076684
$(\text{C}_2\text{H}_3\text{O}+\text{H}_2\text{O}+2\text{H})^+$	63.0438(15)	63.0440544
$(\text{CO}_2+\text{H}_2\text{O}+2\text{H})^+$	63.9950(14)	64.0154934
$(3\text{H}_2\text{O}+\text{OH})^+$	71.0438(15)	71.0338824
$(4\text{H}_2\text{O}+\text{H})^+$	73.0553(20)	73.0495324
$(\text{CO}_2+\text{O}+\text{OH})^+$	76.9898(15)	76.9869324
$(\text{C}_3\text{H}_6+\text{H}_2\text{O}+\text{OH})^+$	77.0588(6)	77.0597044
$(\text{C}_3\text{H}_6+2\text{H}_2\text{O})^+$	78.0474(20)	78.0675294
$(\text{Br}^{79})^+$	78.9177(4)	78.918337
$(\text{C}_2\text{H}_3\text{O}+2\text{H}_2\text{O})^+$	79.0400(8)	79.0389684

$(\text{CO}_2+2\text{H}_2\text{O})^+$	79.9894(2)	80.0104074
$(\text{C}_2\text{H}_3\text{O}+2\text{H}_2\text{O}+\text{H})^+$	80.0339(5)	80.0467934
$(\text{Br}^{81})^+$	80.9155(3)	80.916291
$(\text{CO}+2\text{CNH})^+$	82.0108(5)	82.0161614
$(\text{CH}_3\text{O}+2\text{CNH})^+$	85.0402(8)	85.0396364
$(\text{CO}_2+\text{C}_3\text{H}_6+\text{H})^+$	87.0449(6)	87.0440544
$(3\text{H}_2\text{O}+2\text{OH})^+$	88.0388(8)	88.0366214
$(\text{CO}_2+\text{C}_2\text{H}_5\text{O})^+$	89.0244(6)	89.0233184
$(\text{Br}^{79}+\text{CH}_3)^+$	93.9402(10)	93.941812
$(\text{Br}^{81}+\text{CH}_3)^+$	95.9391(11)	95.939766
$(\text{C}_2\text{H}_3\text{O}+3\text{H}_2\text{O})^+$	97.0462(20)	97.0495324
$(\text{Br}^{79}+\text{CNH})^+$	105.9276(20)	105.9286864
$(\text{Ag}^{107})^+$	106.9045(21)	106.90509
$(\text{Br}^{81}+\text{CNH})^+$	107.9256(22)	107.927189
$(\text{Ag}^{109})^+$	108.9044(23)	108.90475
$(\text{Br}^{79}+\text{CNH}+\text{H}_2\text{O})^+$	123.9360(37)	123.9392504
$(\text{Ag}^{107}+\text{H}_2\text{O})^+$	124.9144(38)	124.915654
$(\text{Br}^{81}+\text{CNH}+\text{H}_2\text{O})^+$	125.935(4)	125.937753
$(\text{Ag}^{109}+\text{H}_2\text{O})^+$	126.9141(39)	126.915314
$(\text{Br}^{79}+\text{CNH}+2\text{H}_2\text{O})^+$	141.9388(54)	141.9498144
$(\text{Ag}^{107}+2\text{H}_2\text{O})^+$	142.9248(55)	142.926218
$(\text{Br}^{81}+\text{CNH}+2\text{H}_2\text{O})^+$	143.9427(56)	143.948317
$(\text{Ag}^{109}+2\text{H}_2\text{O})^+$	144.9237(57)	144.925878
$(\text{C}_2\text{H}_3\text{O}+13\text{H}_2\text{O})^+$	277.121(20)	277.1551724
$(\text{C}_2\text{H}_3\text{O}+13\text{H}_2\text{O}+\text{H})^+$	278.123(20)	278.1629974
$(\text{C}_2\text{H}_3\text{O}+13\text{H}_2\text{O}+2\text{H})^+$	279.138(21)	279.1708224
$(15\text{H}_2\text{O}+\text{OH})^+$	287.213(21)	287.1606504

Table 14: The nuclides present in the mass-spectrum of the primary beam acquired in the presence of the discharge source. In the first column the nuclides present in the mass-spectrum are shown. The nuclides shown in blue have very low intensity. In the third column the table mass values of the nuclides are presented. In the second column the measured mass values and standard error (in brackets) are shown. The measured mass values in black agree with the table mass values within two standard errors (95%-confidence). The measured mass values in blue agree with the table mass values within three standard errors. The measured values in red do not agree within three standard error interval.

In the first column the nuclides present in the mass-spectrum are shown. The nuclides shown in blue have very low intensity (below 20 ions in the peak) . In the third column the table mass values of the nuclides [Nuc00] with a subtracted electron mass are presented. In the second column the measured mass values and standard deviation (in brackets) are shown. The measured mass values in black agree with the table mass values within two standard deviations (95%-confidence). The measured mass values in blue agree with the table mass values within three standard deviations. The measured values in red do not fit into three standard deviation interval. All peaks present in the mass-spectrum can be ordered in seven groups:

1. $(n\text{H}_2\text{O}+m\text{H}+k\text{OH})^{1+}$, $n=1-16$, $k=0,1$, $m=0,1$
2. $(\text{C}_2\text{H}_3\text{O}+m\text{H}+k\text{H}_2\text{O})^{1+}$, $k=0-13$, $m=0-2$
3. $(\text{C}_3\text{H}_6+m\text{OH}+k\text{H}_2\text{O})^{1+}$, $k=0-2$, $m=0,1$
4. $(\text{CO}+\text{H}_2\text{O})^{1+}$, $(\text{CO}_2+\text{H}_2\text{O})^{1+}$, $(\text{N}_2+\text{H}_2\text{O})^{1+}$, $(\text{O}_2+\text{H}_2\text{O})^{1+}$
5. Clusters, which contain CNH-group
6. $(^{107,109}\text{Ag}+n\text{H}_2\text{O})^{1+}$, $n=0-2$
7. $(^{79,81}\text{Br}+n\text{H}_2\text{O}+m\text{CNH})^{1+}$, $n=0-2$, $m=0,1$

From the analysis of these groups one can make the following conclusions:

1. The gas cell contains much water that reacts with all nuclides and compounds present in the gas cell. This reduces the efficiency of the gas cell. In order to reduce the concentration of the water in the gas cell, the gas cell has to be baked out several days.
2. There is a carbon contamination of the gas cell. Since only UHV-materials are used for the gas cell, the origin is probably external. In the present set-up the purification system or pumping system can be such an origin. In the purification system activated carbon is used as an absorber. In the pumping system pump oil is used as working material.
3. In the buffer gas (He) a concentration of noble gases (Ar, Kr, Xe) should be much higher than that of O_2 , N_2 , CO_2 . It follows from the principle of the purification of the He. In the mass-spectrum the concentration of O_2 , N_2 , CO_2 is much higher than that of noble gases. It can be concluded that the gas cell was not fully vacuum tight and there was a weak leak of atmospheric air. The leak was found after the experiment.
4. The origin of Br isotopes can not be easily explained. It can be contained in the materials used for the discharge source or ceramic components.

Chapter 6

On-line mass measurement of ^{107}Ag

The Ortho-TOF MS is designed to be used for direct mass measurements of short-lived nuclides with half-lives down to a few ms. The first *on-line* mass measurement of radioactive nuclides is planned to take place at SHIPTRAP facility[Dil00,Dil01] at GSI. During the experiment described in Chapter 5 an *on-line* mass measurement of the stable isotope ^{107}Ag from the tandem was performed.

$^{107}\text{Ag}^{1+}$ was used as a “unknown” mass, as reference peaks the following nuclides present were used:

four Kr-isotopes ($^{82}\text{Kr}^{1+}$, $^{83}\text{Kr}^{1+}$, $^{84}\text{Kr}^{1+}$, $^{86}\text{Kr}^{1+}$)

six Xe-isotopes ($^{129}\text{Xe}^{1+}$, $^{130}\text{Xe}^{1+}$, $^{131}\text{Xe}^{1+}$, $^{132}\text{Xe}^{1+}$, $^{134}\text{Xe}^{1+}$, $^{136}\text{Xe}^{1+}$)

The measured TOF-spectrum is shown in Fig.(6-1).

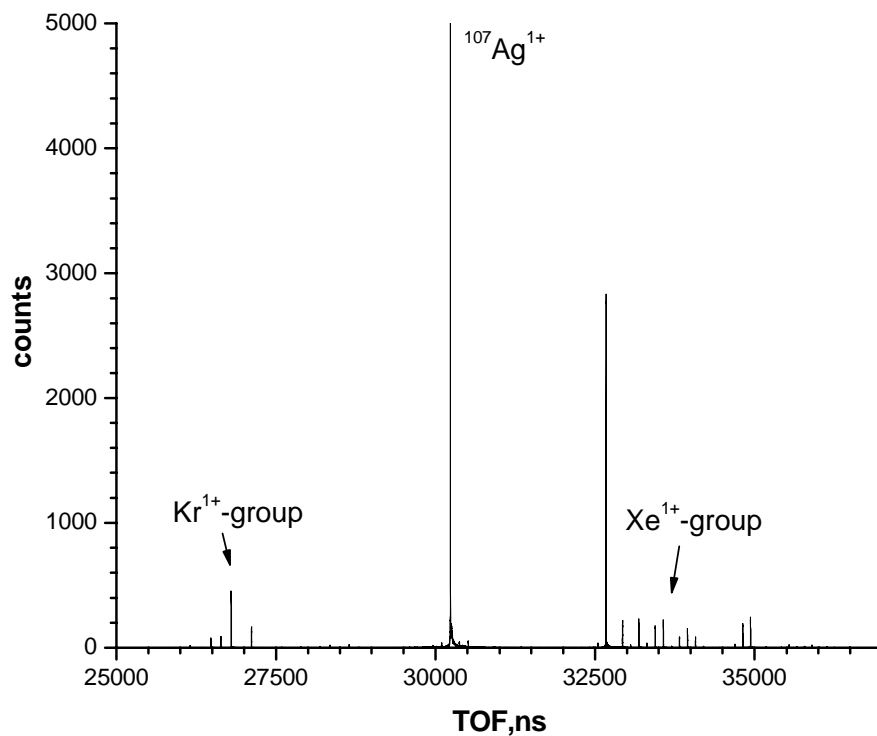


Fig.(6-1): Measured TOF-spectrum of a stable isotope ^{107}Ag extracted from the gas cell measured with the Ortho-TOF MS. The intensity of the Ag beam was 100pA. The kinetic energy of the Ag beam was 23 MeV.

In Table 15 the tabulated values of the reference nuclides with a subtracted electron mass are presented [Nuc00]. The errors of the tabulated masses are omitted because the error of mass identification in the described experiment is much larger.

Reference isotope	Tabulated mass in atomic units
$^{82}\text{Kr}^{1+}$	81,912935420
$^{83}\text{Kr}^{1+}$	82,913587420
$^{84}\text{Kr}^{1+}$	83,910958420
$^{86}\text{Kr}^{1+}$	85,910066420
$^{129}\text{Xe}^{1+}$	128,90422142
$^{130}\text{Xe}^{1+}$	129,90295142
$^{131}\text{Xe}^{1+}$	130,90453142
$^{132}\text{Xe}^{1+}$	131,90360142
$^{134}\text{Xe}^{1+}$	133,90484142
$^{136}\text{Xe}^{1+}$	135,90667142

Table 15: Tabulated values of the reference nuclides used for calibration of the TOF-spectrum of a stable isotope of silver ^{107}Ag from the tandem accelerator

The distance between the reference peaks and the ^{107}Ag is about 25 atomic mass units. Eight spectra were acquired, for each spectrum $\Delta M/M \pm \Delta(\Delta M/M)$ was calculated.

Fig.(6-2) is a plot of these 8 measurements. The red line is the most probable value of $\Delta M/M$, the blue lines are a 67%-confidence band of $\Delta M/M$. The precision of mass determination $\Delta(\Delta M/M)$ is measured to be 1.3 ppm. This corresponds to error of mass determination of 130 keV. From Fig.(6-2) a presence of the systematic error of 170 keV can be seen. The implementation of a calibration ion source with C^{60} will allow to get rid of the systematic error and to increase the precision of mass determination.

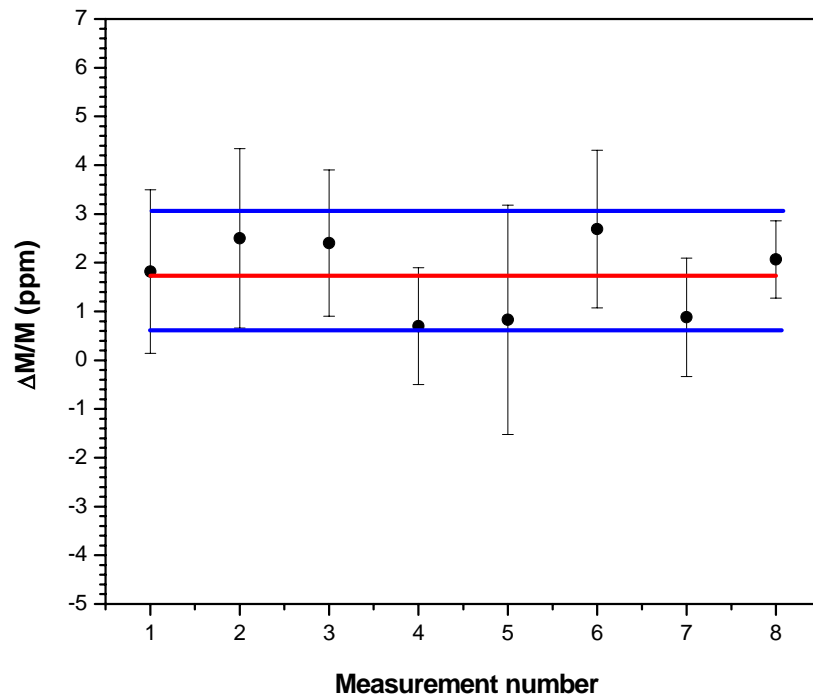


Fig.(6-2): Accuracy and precision of mass determination of $^{107}\text{Ag}^{1+}$. The red line is the most probable value of the accuracy of mass determination, the blue lines are a 67%-confidence band of the accuracy of mass determination (precision). The precision of mass determination is measured to be 1.3 ppm. This corresponds to error of mass determination of 130 keV. The implementation of a calibration ion source with C^{60} will allow to get rid of the systematic error and to increase the precision of mass determination.

Summary and outlook

Results obtained in the thesis

A time-of-flight mass spectrometer with an orthogonal extraction (Ortho-TOF MS) was assembled. A comprehensive experimental investigation of the parameters of the Ortho-TOF MS, such as efficiency, mass resolving power and accuracy of the mass determination in different modes was performed.

The maximum efficiency of the Ortho-TOF MS was measured to be 1% and 3% for the continuous and bunch mode, respectively. This result perfectly agrees with the theoretical estimations.

The achieved maximum experimental mass resolving power of 20000 is also in a good agreement with the presented theoretical investigation.

It was shown that the mass resolving power and the efficiency are two counteracting parameters of the Ortho-TOF MS, which one receives the priority is determined by the goal of the measurements.

The maximum measured precision of mass determination amounts to about 0,51ppm. This corresponding to 100 keV for ^{207}Pb .

A detailed study of cooling and storage properties of the RF-quadrupole was carried out. The importance of this study is determined by the key role played by the RF-quadrupole in the Ortho-TOF MS.

The Ortho-TOF MS was for the first time used as a diagnostic tool for the characterization of the SHIPTRAP gas cell. The Ortho-TOF MS has proved to be very important especially for the study of chemical reactions, taking place in the SHIPTRAP gas cell.

On-line mass measurements of stable ^{107}Ag ions were also performed at the Munich tandem accelerator.. The mass of ^{107}Ag was measured with a precision of 1.3 ppm corresponding to an absolute error in mass determination of about 130 keV.

It was a first successful step for the preparation of an *on-line* mass measurements of short-lived nuclides at SHIP at GSI.

Improvements of the Ortho-TOF MS

Further improvements of the Ortho-TOF MS are an increased mass resolving power and efficiency. As was shown in chapter 4 that the main factors limiting the mass resolving power are the turn-around-time, MCP-detector and stability of the power supplies. High voltage power supplies with higher stability are by now available on market. Recently, high voltage power supplies from ISEQ with stability of 2 ppm and computer control appeared on market. The implementation of such power supplies will increase the mass resolving power limit due to instability of the power supplies up to about 500000 (see Fig.(4-5)). The increase of the mass resolving power limited by the turn-around-time can be done by increasing the extraction electric field in the modulator or/and by increasing the time-of-flight of the ions. The increase of the time-of-flight of the ions can be realized by enlargement of the time-of-flight path (at the expense of the efficiency) or by reducing the kinetic energy of the ions in the TOF-analyser. From the practical point of view one can double the extraction field in the modulator and reduce the kinetic energy of the ions to half of their present value. It will double the time-of-flight of the ions and increase the mass resolving power to 60000. The decrease of the kinetic energy of the ions leads to a decrease of the mass resolving power limited by the MCP-detector to about 21000 (see Eq.(4-9) and Eq.(4-10)). In order to prevent this, one should do a post-acceleration of the ions at the MCP-detector. From the practical point of view one can not go higher than 20 eV for the kinetic energy of the ions. These improvements raise the real mass resolving power of the Ortho-TOF MS up to 30000. Further improvements of the mass resolving power require the implementation of MCPs with a smaller diameter of the micro-channel and a larger bias angle at the same size of the MCP as well as the reduction of the He temperature in the RFQ down to liquid nitrogen temperature (the mass resolving power limit due to the turn-around time is inversely proportional to a square root of the temperature of the buffer gas). Large MCPs with needed dimensions of $40 \times 60 \text{ mm}^2$ and a smaller diameter of the micro-channel and a larger bias angle have not been available on market so far. The implementation of the RFQ cooling with liquid nitrogen requires a new design for

the Ortho-TOF MS. Hence, the maximum reachable mass resolving power of the Ortho-TOF MS amounts to about 37000 (for the maximum achieved efficiency).

Current efficiency of the Ortho-TOF MS is about 3% in the bunch mode. The RFQ transmission can be improved by optimizing the extraction of ions from the RFQ. Increasing the transmission of the RFQ one can obtain ~8%. Further increase of the efficiency can be achieved by increasing the effective surface of the MCPs. This can be done by utilization of the electrons kicked out from the dead surface of the MCP (from present 50% up to 70%). The injection efficiency of the ions into the modulator (see Fig.(2-10)) can be also optimized from the present 50% to the calculated 80-90% by an implementation of an einzel lens which is able to control the ion movement in each coordinate-plane. Thus, a total efficiency of 13-15% can be reached.

Short-lived transuranium nuclides whose unknown masses can be measured by SHIPTRAP-Ortho-TOF MS installation

The efficiency, mass resolving power and precision of mass determination of the Ortho-TOF MS define the application for nuclear reaction products.

The mass resolving power of 20000 corresponds to a peak width ΔM of about 10 MeV for $A=250$ amu. Thus, different isobars or isomer and ground state of a nuclide can not be resolved. Therefore, only well separated masses can be measured with the Ortho-TOF MS. The SHIP at GSI is suitable for it. The SHIP already separates quite well the nuclides produced in the cold fusion-evaporation reaction and one can expect a strong suppression of any proton evaporation channel, i.e. contribution of isobaric chain nuclides.

The total efficiency of ~1% (8% for the Ortho-TOF MS and ~10% for the SHIPTRAP gas cell) puts a restriction for measurements of very exotic nuclei. Table C_1 presents a list of nuclides which masses are unknown [Aud03] and which can be at the SHIPTRAP-Ortho-TOF MS installation. For production of nuclides (indicated in column 1 of table) with half-lives (column 2) one can propose to use the fusion-evaporation reactions listed in column 3. The beam energies (column 4) correspond to the expected maximum in the production cross-sections. From all possible reactions, which can be used for the production, one should choose those which are “symmetric” in beam-target mass composition. This choice guarantees

suitable recoil energies (column 5) which allow to penetrate the entrance-window, separating the SHIP high vacuum from the helium pressure in the gas cell. The excitation energies of the compound nuclides (in the next frame) E_{CN}^* are presented in the 6-th column. As it is very important to suppress as much as possible the evaporation channel which includes protons originating the background isobaric masses, the excitation energies of compound states should be less than the sum of separation energy and Coulomb barrier for proton. For nuclides presented in Table C_1 the Coulomb barrier for proton decay Q is typically from 18 to 20 MeV. The separation energies for proton, proton and neutron and for proton and two neutrons are $S_p = 1-4$ MeV, $S_{pn} = 7-11$ MeV and $S_{p2n} = 15-18$ MeV. Since for many nuclides the sum $S_x + Q$ is much less than excitation energy E_{CN}^* , the proton channel must be considerably suppressed. The production cross-sections known from experiments or expected from extrapolations are shown in column 7. Using these values one can estimate the yields of nuclides which are expected in MCP of TOF-system. A typical primary beam intensity of $0.4 \mu\text{A}$, the number of atoms in the target as 10^{18} , the transmission of SHIP and SHIPTRAP-Ortho-TOF MS as 40% and 1% are assumed. The yields per hour are given in column 8. As can be seen from this column the measurements of masses are feasible for the most of the nuclides listed in Table C_1. Only for Lr, Rf and Db-nuclides to get enough statistic can be problematic.

On the bottom part of Table C_1 some examples of transuranium nuclides are given whose masses are known from indirect mass determination via alpha-decay chains [Aud03]. These cases can be used for pilot experiments. Besides them, the best nuclides with unknown masses which one can start with are ^{251}No , ^{254}Lr and ^{226}Np .

Nuclide	$T_{1/2}$ (s)	Reaction	E_{beam} (MeV)	E_{recoil} (keV)	E_{CN}^* (MeV)	σ (nb)	Yield (h^{-1})
^{226}Np	0.031	$^{181}\text{Ta} (^{48}\text{Ca}, 3\text{n})$	200	180	32	$\approx 100^*$	≈ 3
^{238}Cf	0.02	$^{192}\text{Os} (^{48}\text{Ti}, 2\text{n})$	200	167	17.5		
^{237}Cf	2.1	$^{190}\text{Os} (^{48}\text{Ti}, 1\text{n})$	200	170	15		
$^{240}\text{Es}^\#$	(≈ 5)	$^{197}\text{Au} (^{44}\text{Ca}, 1\text{n})$	195	147	22.8		
^{245}Fm	4.2	$^{196}\text{Pt} (^{50}\text{Ti}, 1\text{n})$	210	170	13.5		
^{243}Fm	0.18	$^{196}\text{Pt} (^{48}\text{Ti}, 1\text{n})$	210	170	18.5		
^{246}Md	1.0	$^{197}\text{Au} (^{50}\text{Ti}, 1\text{n})$	220	180	16.7		
$^{245\text{m}}\text{Md}$	0.4	$^{197}\text{Au} (^{50}\text{Ti}, 2\text{n})$	220	180	16.7		
^{251}No	0.75	$^{206}\text{Pb} (^{48}\text{Ca}, 3\text{n})$	220	160	26	$\approx 100^*$	≈ 3
$^{249}\text{No}^\#$	≈ 0.5	$^{206}\text{Pb} (^{44}\text{Ca}, 1\text{n})$ $^{196}\text{Pt} (^{54}\text{Cr}, 1\text{n})$	210 240	150 208	26.5 17.1		

^{254}Lr	13	^{209}Bi ($^{48}\text{Ca},3\text{n}$) ^{205}Tl ($^{50}\text{Ti},1\text{n}$)	230 220	170 170	29 11.2	40 (12) ^{a,b} $\approx 10^*$	1 ≈ 0.3
^{252}Lr	0.36	^{205}Tl ($^{48}\text{Ti},1\text{n}$) ^{203}Tl ($^{50}\text{Ti},1\text{n}$)	220 230	160 180	17.2 17.5	$\approx 10^*$ $\approx 10^*$	≈ 0.3 ≈ 0.3
$^{251}\text{Lr}^\#$	≈ 0.5	^{205}Tl ($^{48}\text{Ti},2\text{n}$)	220	160	17.2	$\approx 10^*$	≈ 0.3
^{255}Rf	1.64	^{206}Pb ($^{50}\text{Ti},1\text{n}$) ^{208}Pb ($^{48}\text{Ti},1\text{n}$) ^{207}Pb ($^{50}\text{Ti},2\text{n}$)	230 230 230	180 170 170	15.7 22.5 15.2	10^b $\approx 10^*$ $10^{c,d}$	0.3 ≈ 0.3 0.3
^{258}Db	4.4	^{205}Tl ($^{54}\text{Cr},1\text{n}$) ^{209}Bi ($^{50}\text{Ti},1\text{n}$)	250 230	200 170	15 15.7	$4.3(4)^c$	0.1
^{256}Db	1.9	^{209}Bi ($^{48}\text{Ti},1\text{n}$) ^{205}Tl ($^{52}\text{Cr},1\text{n}$)	230 240	170 190	19.8 11.7	$\approx 4^*$	≈ 0.1
^{255}Db	≈ 1.6	^{209}Bi ($^{48}\text{Ti},2\text{n}$)	230	170	19.8	$\approx 2^*$	≈ 0.05
Nuclides with known masses							
^{227}Np	0.51	^{181}Ta ($^{48}\text{Ca},2\text{n}$)	190	174	23.8		
^{225}U	0.095	^{180}Hf ($^{48}\text{Ca},3\text{n}$)	200	185	35	$130(60)^b$	4
^{246}Fm	1.1	^{198}Pt ($^{50}\text{Ti},2\text{n}$)	220	180	22.4		
^{252}No	2.3	^{206}Pb ($^{48}\text{Ca},2\text{n}$)	220	160	26	500^e	15

Table C_1: Short-lived transuranium nuclides with unknown masses which can be measured with the SHIPTRAP-Ortho-TOF MS installation. A typical primary beam intensity of 0.4 μA , the number of atoms in the target as 10^{18} , the transmission of SHIP and SHIPTRAP-Ortho-TOF MS as 40% and 1% are assumed.

- unknown nuclide,

*- expected (extrapolated) value,

a) Yu. Lazarev et al. Nucl.Phys. **A580**, 113 (1994).

b) H. Gaeggeler et al., GSI annual rep. 1989, p.22 (1990).

c) F. Hessberger et al., Eur.Phys.J. **A12**, 57 (2001).

d) Yu. Oganessian et al., Nucl.Phys. **A239**, 157 (1975).

e) Yu.Oganessian et al.,Phys.Rev. **C64**, 054606 (2001).

Appendix 1

Principle of a time-of-flight mass spectrometer

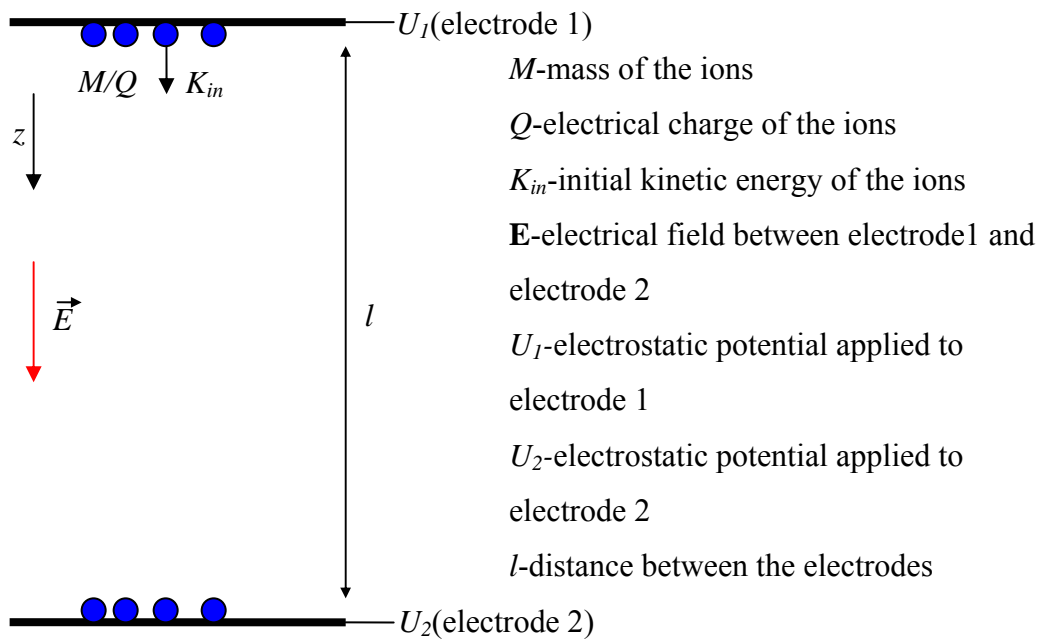


Fig.(A1-1): Basic principle of time-of-flight mass spectrometry. Ions with different mass to charge (M/Q) ratios have different time-of-flights along path l . Not being spatially separated at the initial position (electrode 1), the ions with different M/Q get separated in space at electrode 2 (detector)

The time-of-flight t of an ion with mass M and electrical charge Q between two electrode 1 and 2 (see Fig. A1-1) can be derived from the following general formula:

$$t = \int_0^l \frac{dz}{v(z)} \tag{A1_1}$$

where z is the coordinate along which the ion moves between the electrodes. The initial position of the ion at electrode 1 corresponds to $z=0$, the final position of the ion at electrode 2 corresponds to $z=l$. $v(z)$ is the velocity of the ion at the position z .

From the energy conservation law the following expression for $v(z)$ can be obtained (non-relativistic approach):

$$v(z) = \sqrt{\frac{2}{M}(K_{in} + QEz)} \quad (A1_2)$$

where the quantities in the equation are defined in Fig.(A1-1). Substituting Eq.(A1_2) in Eq.(A1_1) the following expression can be obtained for t :

$$t = \int_0^l \frac{dz}{\sqrt{\frac{2}{M}(K_{in} + QEz)}} \quad (A1_3)$$

Integration of Eq.(A1_3) yields:

$$t = \frac{1}{E} \sqrt{\frac{2M}{Q}} \left(\sqrt{\frac{K_{in}}{Q} + lE} - \sqrt{\frac{K_{in}}{Q}} \right) \quad (A1_4)$$

Rearrangement of Eq.(A1_4) leads to the following expression:

$$t = \frac{2l}{\sqrt{\frac{2Q}{M}} \left(\sqrt{\frac{K_{in}}{Q} + lE} + \sqrt{\frac{K_{in}}{Q}} \right)} \quad (A1_5)$$

Substituting $K_{in}=0$ in Eq.(A1_5) one can get the time of flight of the ions in the time-of-flight mass spectrometer shown in Fig.(1-1) of Chapter 1 (see Eq.(1_1)):

$$t = \sqrt{\frac{M}{Q}} \sqrt{\frac{2l}{E}} \quad (A1_6)$$

Eqs.(1_3,1_4,1_5) of chapter 1 are obtained from Eq.(A1_5) in a similar way.

The time of flight of ions in a reflection time-of-flight mass spectrometer (see Fig.(1-4)) can be expressed as follows:

$$t(z) = t_1 + t_2 + 2(t_3 + t_4 + t_5) \quad (\text{A1-7})$$

where t_1, t_2, t_3, t_4, t_5 are the time-of-flight of ions in the modulator, acceleration region, drift space, the first stage of the reflector and the last stage of the reflector, respectively (see Fig(1-4)). From Eq.(A1_4) one obtains

$$\begin{aligned} t_1 &= \frac{1}{E_1} \sqrt{\frac{2M}{Q}} (\sqrt{zE_1}) \\ t_2 &= \frac{1}{E_2} \sqrt{\frac{2M}{Q}} (\sqrt{zE_1 + l_2E_2} - \sqrt{zE_1}) \\ t_3 &= \sqrt{\frac{2M}{Q}} \frac{l/2}{\sqrt{zE_1 + l_2E_2}} \\ t_4 &= \frac{1}{E_3} \sqrt{\frac{2M}{Q}} (\sqrt{zE_1 + l_2E_2 + l_3E_3} - \sqrt{zE_1 + l_2E_2}) \\ t_5 &= -\frac{1}{E_4} \sqrt{\frac{2M}{Q}} (\sqrt{zE_1 + l_2E_2 + l_3E_3}) \end{aligned} \quad (\text{A1-8})$$

All parameters in Eqs.(A1_8) are defined in Fig.(1-4) and Eq.(1_13). Substituting Eqs.(A1_8) in Eq.(A1_7) one gets

$$\begin{aligned} t(z) &= \sqrt{\frac{2M}{Q}} \left[\frac{1}{E_1} (\sqrt{zE_1}) + \frac{1}{E_2} (\sqrt{zE_1 + l_2E_2} - \sqrt{zE_1}) + \frac{l}{\sqrt{zE_1 + l_2E_2}} \right] + \\ &+ \sqrt{\frac{2M}{Q}} \left[\frac{2}{E_3} (\sqrt{zE_1 + l_2E_2 + l_3E_3} - \sqrt{zE_1 + l_2E_2}) - \frac{2}{E_4} (\sqrt{zE_1 + l_2E_2 + l_3E_3}) \right] \end{aligned} \quad (\text{A1-9})$$

After a rearrangement of Eq.(A1_9) one obtains Eq.(1_13) of Chapter 1:

$$\begin{aligned} t(z) &= \sqrt{\frac{2M}{QE_1}} \left[\left(1 - \frac{E_1}{E_2}\right) \sqrt{z} + \left(\frac{E_1}{E_2} - 2\frac{E_1}{E_3}\right) \sqrt{z + \frac{l_2E_2}{E_1}} + \frac{l}{\sqrt{z + \frac{l_2E_2}{E_1}}} + \right. \\ &\left. + 2\left(\frac{E_1}{E_3} - \frac{E_1}{E_4}\right) \sqrt{z + \frac{l_2E_2}{E_1} + \frac{l_3E_3}{E_1}} \right] \end{aligned} \quad (\text{A1-10})$$

The total time of flight $t(z)$ can be expanded in Taylor-series relative to the average ion start position z_0 :

$$t(z) = t_0 + \frac{1}{1!} \left[\frac{\partial t(z)}{\partial z} \right]_{z=z_0} \Delta z + \frac{1}{2!} \left[\frac{\partial^2 t(z)}{\partial z^2} \right]_{z=z_0} \Delta z^2 + \dots \quad (\text{A1}_{-11})$$

Postulating the condition for the second order focusing

$$\begin{aligned} \left[\frac{\partial t(z)}{\partial z} \right]_{z=z_0} &= 0 \\ \left[\frac{\partial^2 t(z)}{\partial z^2} \right]_{z=z_0} &= 0 \end{aligned} \quad (\text{A1}_{-12})$$

one obtains the following system of two equations(A1_13):

$$\begin{aligned} & \left[\frac{1}{2\sqrt{z_0}} \left(1 - \frac{E_1}{E_2} \right) + \left(\frac{E_1}{2E_2} - \frac{E_1}{E_3} \right) \frac{1}{\sqrt{z_0 + \frac{l_2 E_2}{E_1}}} - \frac{1}{2} \frac{l}{\sqrt{\left(z_0 + \frac{l_2 E_2}{E_1} \right)^3}} + \right. \\ & \left. + \left(\frac{E_1}{E_3} - \frac{E_1}{E_4} \right) \frac{1}{\sqrt{z_0 + \frac{l_2 E_2}{E_1} + \frac{l_3 E_3}{E_1}}} \right] = 0 \\ & \left[\frac{1}{2\sqrt{z_0^3}} \left(\frac{E_1}{E_2} - 1 \right) + \left(\frac{E_1}{E_3} - \frac{E_1}{2E_2} \right) \frac{1}{\sqrt{\left(z_0 + \frac{l_2 E_2}{E_1} \right)^3}} + \frac{3}{2} \frac{l}{\sqrt{\left(z_0 + \frac{l_2 E_2}{E_1} \right)^5}} + \right. \\ & \left. + \left(\frac{E_1}{E_4} - \frac{E_1}{E_3} \right) \frac{1}{\sqrt{\left(z_0 + \frac{l_2 E_2}{E_1} + \frac{l_3 E_3}{E_1} \right)^3}} \right] = 0 \end{aligned}$$

From this system E_3 and E_4 can be found:

$$E_3 = f_1(E_1, E_2, l_1, l_2, l, l_3, l_4) \quad (\text{A1}_{-14})$$

$$E_4=f_2(E_1, E_2, l_1, l_2, l_3, l_4)$$

Time resolving power R_t of the reflecting time-of-flight mass spectrometer in a second order focusing mode can be expressed as follows:

$$R_t = \frac{t_0}{\frac{1}{3!} \left[\frac{\partial^3 t(z)}{\partial z^3} \right]_{z=z_0} \Delta z^3} \quad (\text{A1}_{15})$$

For the calculation of the second order focusing mode a script file for the Mathematica 3.0 software package was used. $E_1, E_2, l_1, l_2, l_3, l_4, M, Q, z_0$ are input parameters. This script uses Eqs.(A1_11, A1_13, A1_15) in order to calculate $E_3, E_4, t(z_0)$ and R_t .

From Eqs.(A1_13) it can be seen that the condition of second order focusing can be fulfilled only if the following expressions are valid:

$$\begin{aligned} z_0 + \frac{l_2 E_2}{E_1} &> 0 \\ z_0 + \frac{l_2 E_2}{E_1} + \frac{l_3 E_3}{E_1} &> 0 \end{aligned} \quad (\text{A1}_{16})$$

If the first derivative (see Eq.(A1_12)) slightly differs from 0 the mode is called distorted second order focusing mode.

In Fig.(A1_2) a difference between the time-of-flight of an ion of mass 133 amu and single charge state with the start position z and the time-of-flight of an identical ion with the reference start position z_0 is plotted as a function of $(z-z_0)$. The values that have been used for the input parameters ($E_1, E_2, l_1, l_2, l_3, l_4, M, Q, z_0$) are given in Appendix 6. The blue curve corresponds to the second order focusing mode. The red curve corresponds to a distorted second order focusing mode (the first derivative is equal to $-0,0012 \mu\text{s/cm}$).

The mass resolving power for the second order focusing mode (blue curve) and distorted second order focusing mode (red curve) is plotted as a function of the beam spatial spread in Fig.(A1_3).

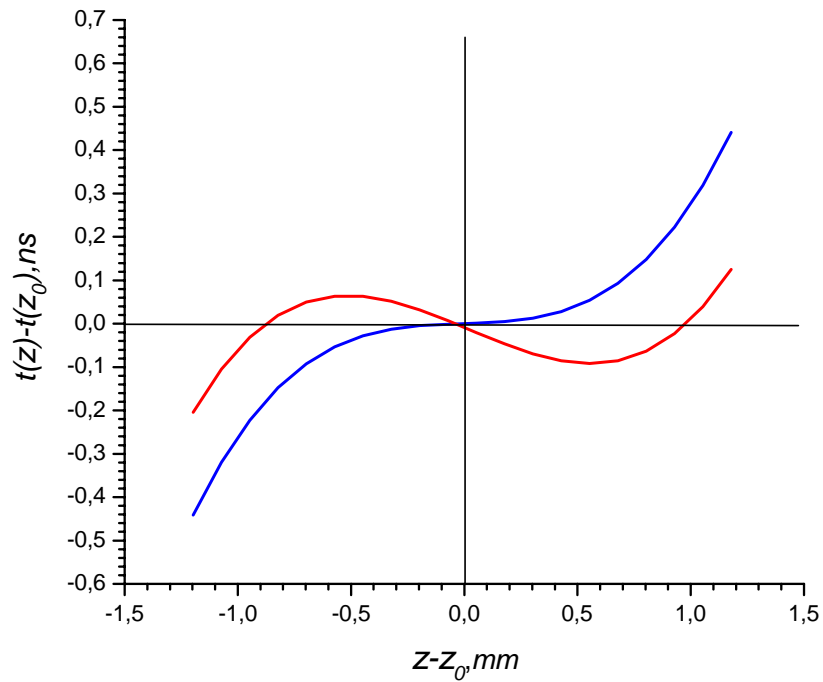


Fig.(A1_2): Difference between the time-of-flight of an ion of mass 133 amu with the start position z and the time-of-flight of an identical ion with the reference start position z_0 as a function of $(z-z_0)$. The blue curve corresponds to the second order focusing mode (Eq.(A1_11) and Eq.(A1_12)). The red curve corresponds to the distorted second order focusing mode (the first derivative is equal to $-0,0012 \mu\text{s}/\text{cm}$) (Eq.(A1_11) and Eq.(A1_12)).

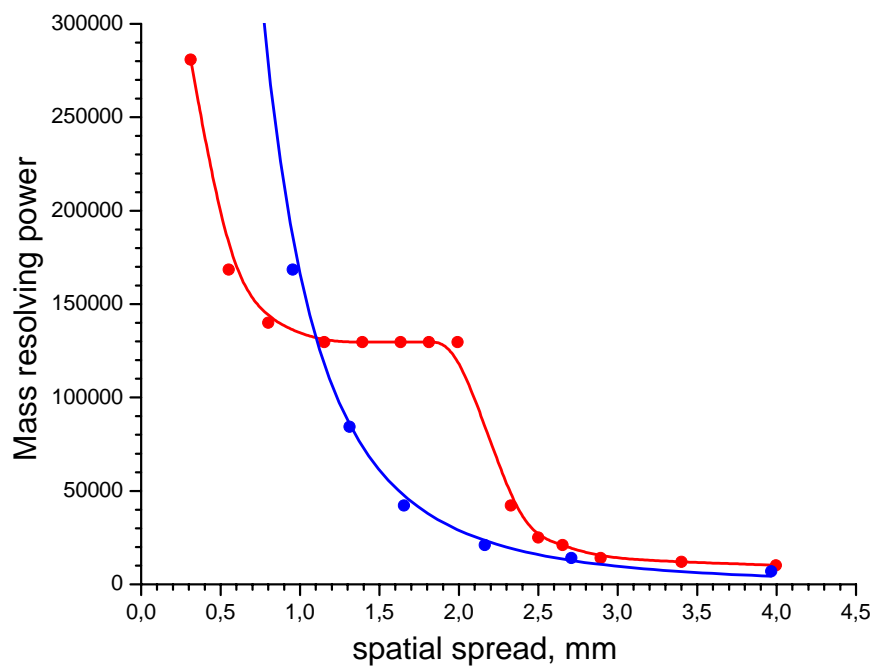


Fig.(A1_3): Mass resolving power for the second order focusing mode (blue curve) and distorted second order focusing mode (red curve) as a function of the beam spatial spread (see Fig.(A1_2))

While the mass resolving power in the distorted second order focusing mode is much lower than in the second order focusing mode for a narrow beam (spatial spread < 1mm), it becomes higher for a broad beam (spatial spread ~ 2mm) (see Fig.(A1_3)).

Appendix 2

Einzel lens

A schematic view of the einzel lens used in the Ortho-TOF-MS is presented in Fig.(2-9(a,b)) of chapter 2. From the ion optics [Wol87] it is well known that an einzel lens can be described in the first approximation as a thin lens. The focus length for a thin lens can be calculated from [Wol87] (see Eq.(4_8)).

The focus length of the einzel lens for $K_{ions}=11.5$ eV as a function of the focusing potential applied to the einzel lens is presented in Fig.(A2-1). The calculation was performed in SIMION [Sim00].

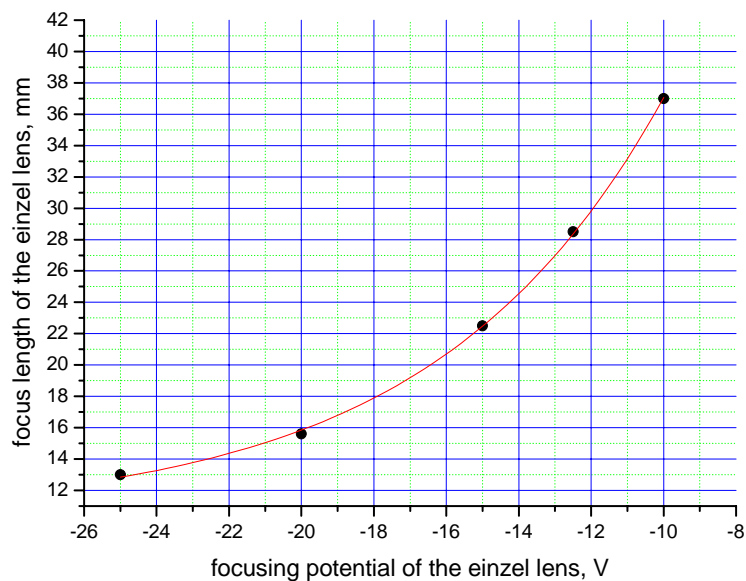


Fig.(A2-1): The focus length of the einzel lens for kinetic energy of ions $K_{ions}=11.5$ eV as a function of the focusing potential applied to the einzel lens

The longer the focus length of the einzel lens, the smaller the divergence of the ion beam after the einzel lens. In order to understand how the angular spread of the beam depends on the width of the beam in the accumulation region let us consider the ion optical properties of the einzel lens in more details. There are four cases which are of interest for an application in the Ortho-TOF MS. They are listed below and schematic diagrams of these cases are shown in Fig.(A2-3(a, b, c and d)): (1) The

source (the orifice of Slit 1; see Fig.(2-1)) is situated between the focus and the lens. (Fig.(A2-3(a))), (2) the source coincides with the focus. (Fig.(A2-3(b))), (3) the focus is situated between the source and the lens, the image is situated before Slit2 (Fig.(A2-3(c))) and (4) the focus is situated between the source and the lens, the image is situated after Slit2 (Fig(A2-3(d))).

The designations in Fig.(A2-3) mean the following:

l_1 is the distance between the source and the einzel lens. In the present Ortho-TOF MS it is fixed and equals 37 mm.

l_2 is the distance between the image and the einzel lens.

f is the focus of the einzel lens.

d is the distance between the einzel lens and Slit2. In the present Ortho-TOF MS it is fixed and equals 24 mm.

α_1 is the divergence of the beam before the einzel lens. In the present Ortho-TOF MS it is estimated to be 0.1 rad (the velocity spread of cooled ions in the RFQ over the axial velocity gained by ions after their extraction from the RFQ).

α_2 is the divergence of the beam after the einzel lens(in the modulator).

In case b the beam after the einzel lens is parallel and has the following diameter:

$$D = 2y_2 = 2 \tan \alpha_1 * l_1 \approx \alpha_1 * l_1 \quad (\text{A2}_1)$$

Substituting values for α_1 and l_1 into Eq.(A2_1) one can get for the diameter of the beam the following value:

$$D = 7.4 \text{ mm} \quad (\text{A2}_2)$$

This corresponds to a mass resolving power of 900. From this result it is seen that a smaller beam width and, thus, higher mass resolving power can be reached when either case c or d is realized.

The diameter of the beam at Slit2 can be expressed as follows:

$$\alpha_2 = \alpha_1 \frac{l_1}{l_2}$$

$$c: D = 2y_2 = 2(d - l_2)\alpha_2 \quad (\text{A2}_3)$$

$$d: D = 2y_2 = 2(l_2 - d)\alpha_2$$

The diameter of the beam at Slit2 as a function of α_2 is shown in Fig.(A2-2).

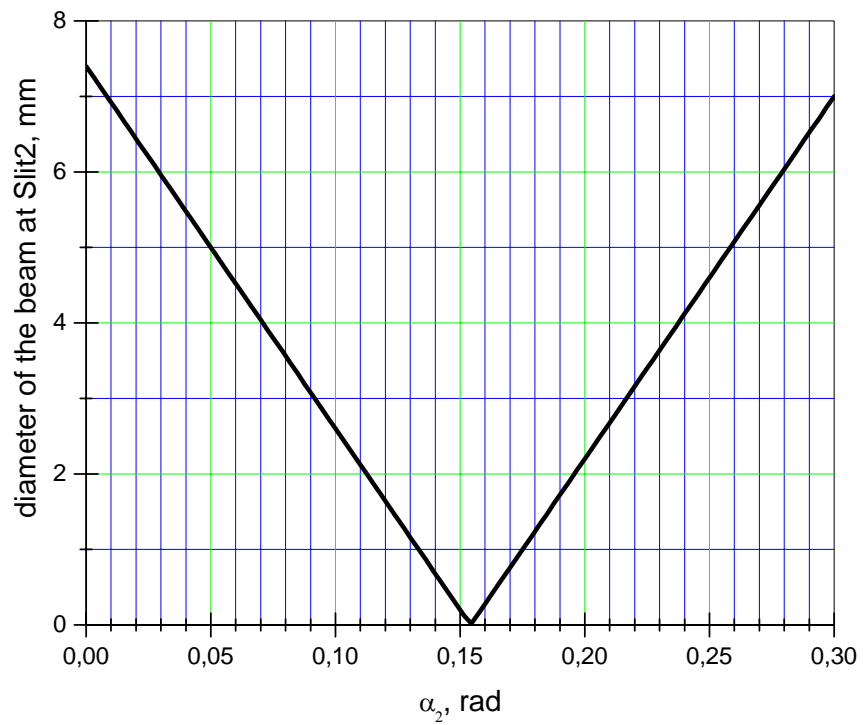


Fig.(A2-2): The diameter of the beam at Slit2 as a function of the divergence of the beam behind the einzel lens (in the modulator) α_2

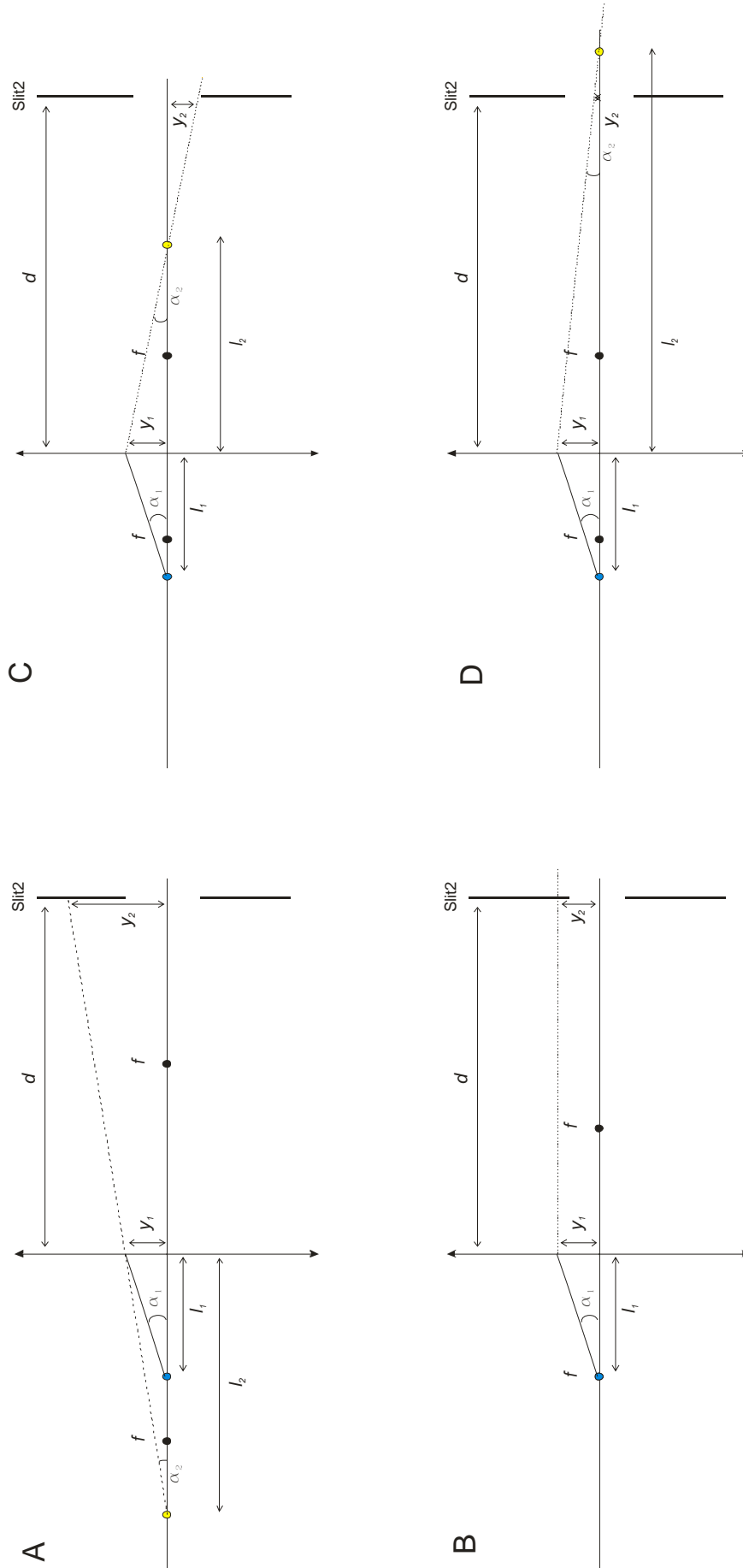


Fig.(A2-3): Four regimes of the einzel lens operation. From the ion optics [Wol87] it is well known that an einzel lens can be described in the first approximation as a thin lens. f is the focus length of the thin lens, l_1 is the distance between the object and the thin lens, l_2 is the distance between the image and the thin lens. A: the source is situated between the focus and the thin lens; B: the source coincides with the focus; C: the source is situated between the focus and the thin lens, the image is situated before Slit 2; D: the source is situated between the focus and the thin lens, the image is situated after Slit 2.

Appendix 3

Space charge effect on an ion capacity of the linear RFQ trap

In Fig.(A3-1(a,b)) the potential well depth of the linear RFQ-trap is shown as a function of the axial coordinate X, as calculated with the program SIMION.

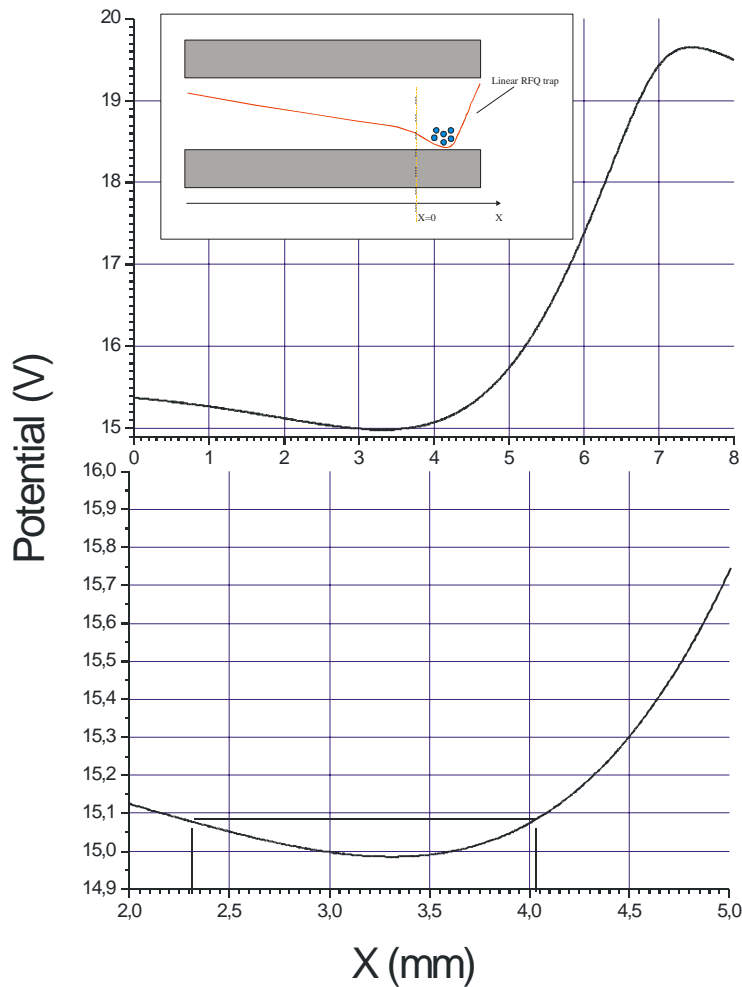


Fig.(A3-1(a,b)): The profile of the linear RFQ trap, simulated in SIMION. Along axis X a spatial dimension of the linear RFQ trap is presented, along axis Y a depth of the linear RFQ trap in Volts is shown. Fig.(A3-1(b)) is a scaled plot of Fig.(A3-1(a)). The zero-reference point of axis X is chosen arbitrarily.

App. 3 Space charge effect on an ion capacity of the RFQ trap XIII

Cooled ions have a mean kinetic energy of the order of 0.1 eV (see Fig.(3-5(b))). Thus, when there are only few ions in the linear RFQ trap (i.e. if space charge effects can be neglected) they occupy the linear RFQ trap from the bottom (15V level) up to a level of 15.1V, which corresponds to the mean energy of the ions of 0.1 eV. Thus, under these conditions, geometrical dimension of the linear RFQ-trap can be estimated as 1.5-2 mm. Let us now consider a case with a large number of the ions in the linear RFQ-trap. In this case space charge effects start to play a significant role. An illustration of the competition between the confinement of the ions due to the RF pseudo-potential of the linear RFQ trap (green arrows) and the repulsing effect due to the space charge of the ions in the linear RFQ trap (red arrows) is shown in Fig.(A3-2).

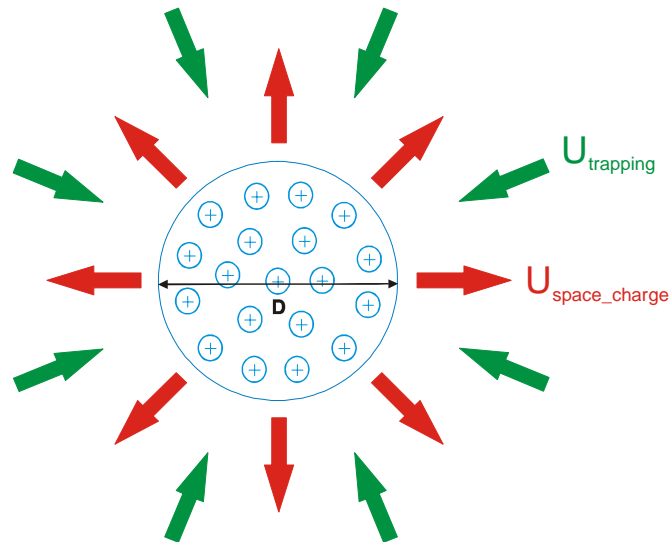


Fig.(A3-2): An illustration of a competition between the confinement of the ions due to the potential profile of the linear RFQ trap (green arrows) and repulsing effect due to space charge of the ions in the linear RFQ trap

The ions are confined to a cylinder. Since the height and the radius of the cylinder are almost equal (~ 1.8 mm), for the simplicity of further calculation we can assume, that the ions are confined to a sphere with a diameter D . The balance Eq.(A3_1) gives a value for D , and therefore, the spatial dimension of the linear RFQ trap.

$$U_{trapping} = U_{space_charge} \quad (A3_1)$$

App. 3 Space charge effect on an ion capacity of the RFQ trap XIV

$U_{trapping}$ and the D , corresponding to $U_{trapping}$, can be derived from fig.(A3-1).

U_{space_charge} can be expressed from the Gauss theorem for electrostatic field (sphere case; the charge distribution in the trap is homogeneous [Tol00]):

$$U_{space_charge} = \frac{1}{4\pi\epsilon_0} \frac{nQ}{R} \quad (A3_2)$$

where n is the number of the ions in the linear RFQ trap, Q is the charge of the single ion (positive e), R is the radius of the ions cloud ($R = D/2$), ϵ_0 is the permittivity of vacuum. Substituting Eq.(A3_2) into Eq.(A3_1) one obtains for the number of ions in the trap:

$$n = \frac{2\pi\epsilon_0 U_{trapping} D}{Q} \quad (A3_3)$$

Substituting numerical values for ϵ_0 , π and Q one gets the following expression:

$$n = 3.47 * 10^8 D U_{trapping} \text{ [ions]} \quad (A3_4)$$

where D is in mm and $U_{trapping}$ is in Volts. For few ions in the linear RFQ trap when there is no charge effect ions occupy a sphere with $D \sim 1.8 \text{ mm}$ and $U_{trapping} = 0.1 \text{ V}$. Substituting it into Eq.(A3_4) one can get:

$$n_{no_charge_effect} \cong 5 * 10^4 \text{ [ions]} \quad (A3_5)$$

Further increase of the ion number will increase the ion cloud diameter D and require a deeper $U_{trapping}$. Since D is a function of $U_{trapping}$, one can rewrite Eq.(A3_4) as follows:

$$n = 3.47 * 10^8 f(U_{trapping}) U_{trapping} \text{ [ions]} \quad (A3_6)$$

App. 3 Space charge effect on an ion capacity of the RFQ trap XV

where $f(U_{trapping}) = D$. In order to determine $f(U_{trapping})$ one can make a SIMION simulation of the linear RFQ trap in the storage and extraction regimes. In Fig.(A3-3) results of such a simulation are shown.

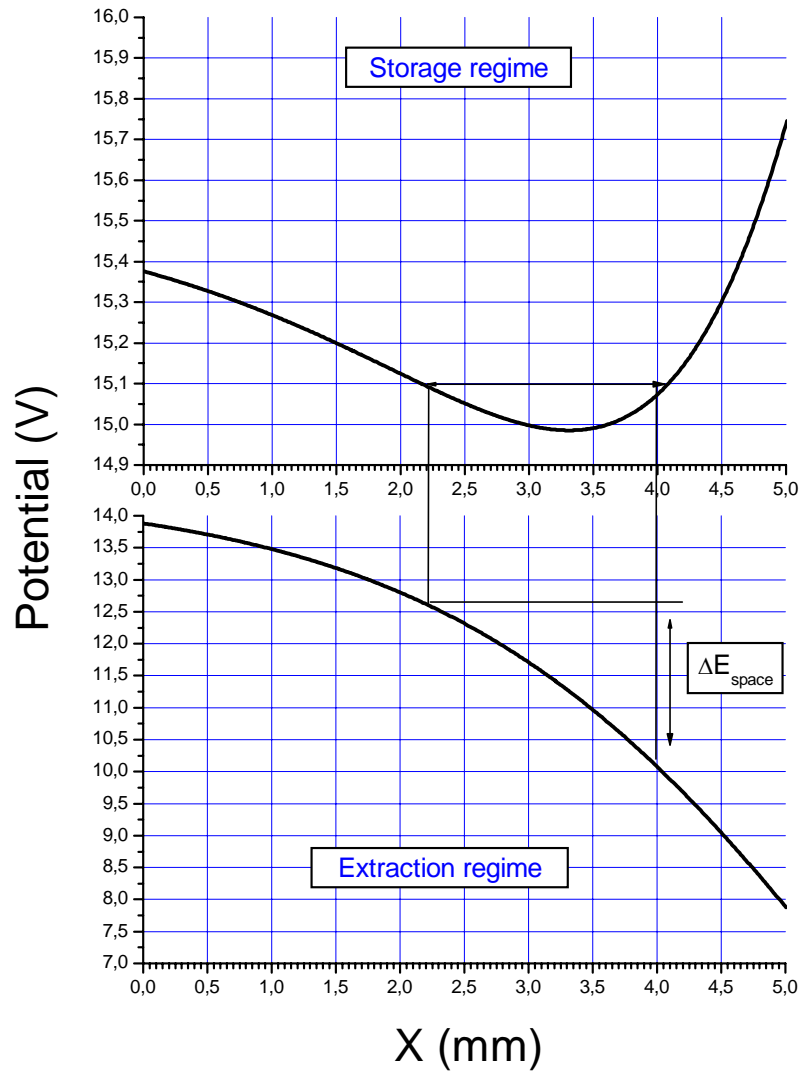


Fig.(A3-3): SIMION simulation of the linear RFQ trap in a storage and extraction regimes. Along axis X a spatial dimension of the linear RFQ trap is presented, along axis Y a depth of the linear RFQ trap in Volts is shown. The zero-reference point of axis X is chosen arbitrarily.

From the figure for the storage regime one can derive the following dependence of D on $U_{trapping}$ (Fig.(A3-4)).

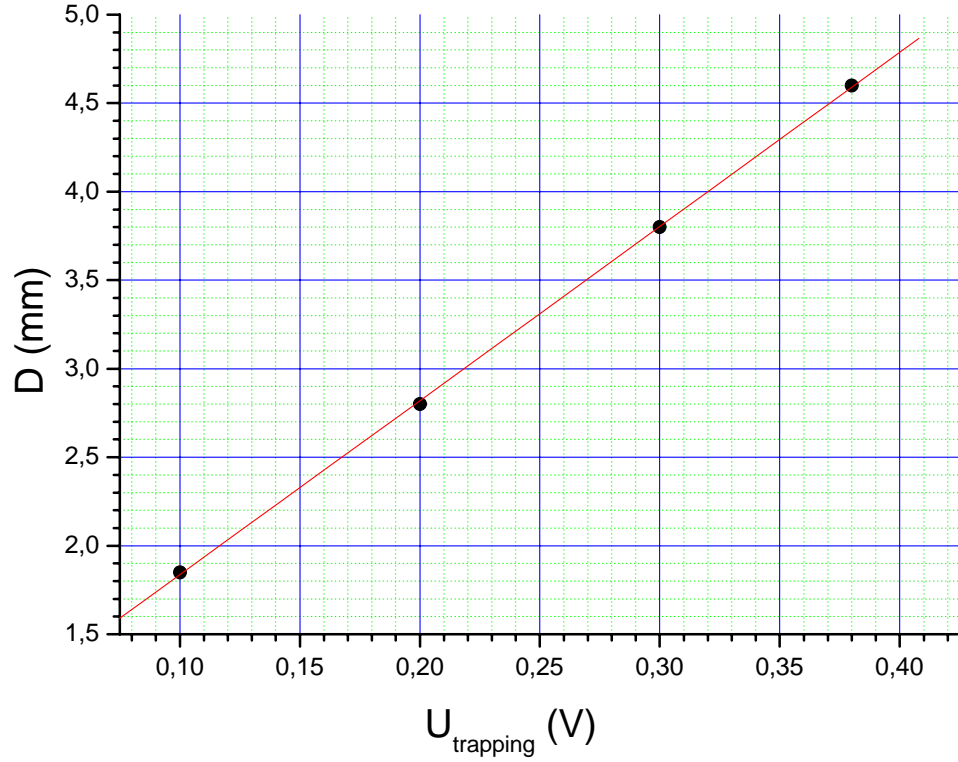


Fig.(A3-4): SIMION simulation of the diameter D of the ion cloud in the linear RFQ trap vs the trapping potential $U_{trapping}$

The linear dependence is valid for $U_{trapping}$ up to 0.5 V. For this range one can derive the following expression for D from Fig. (A3-3):

$$D = 0.01U_{trapping} + 0.0008 \text{ [m]} \quad (\text{A3}_7)$$

where $U_{trapping}$ is in Volts. Substituting this expression into Eq.(A3_6) one can obtain the number of ions in the linear RFQ-trap n in case if $n > n_{no_charge_effect} \cong 5 * 10^4$ and $0.1\text{V} < U_{trapping} < 0.5\text{V}$:

$$n = 3.47 * 10^8 U_{trapping} (0.01U_{trapping} + 0.0008) \text{ [ions]} \quad (\text{A3}_8)$$

where $U_{trapping}$ is in Volts. In graphical form this result is presented in Fig.(A3-5):

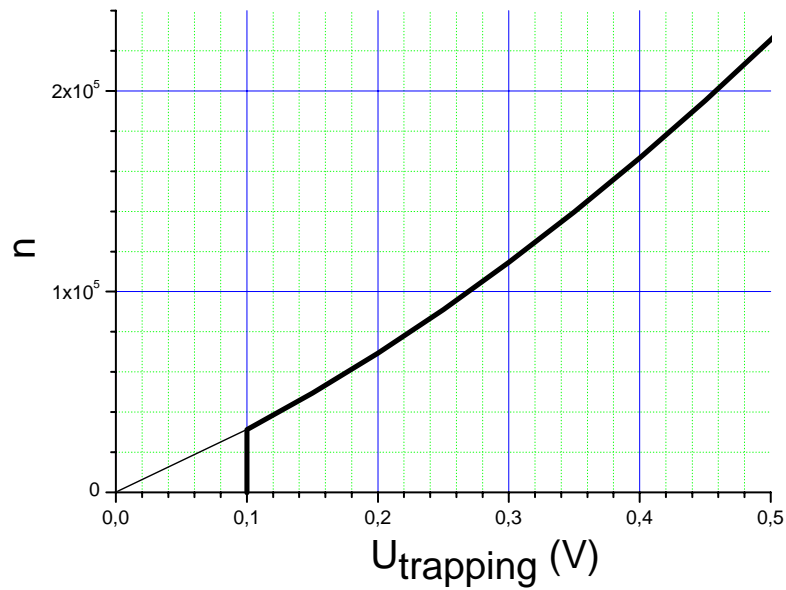


Fig.(A3-5):SIMION simulation of number of ions n stored in the linear RFQ trap vs trapping potential $U_{trapping}$

Higher than $U_{trapping} = 0.5V$ the ion cloud expands drastically. Thus, this region does not belong to the linear RFQ-trap, though the ions are still trapped in the RFQ. A scaled version of the Fig.(A3-3) is presented in Fig.(A3-6) in order to illustrate this expansion.

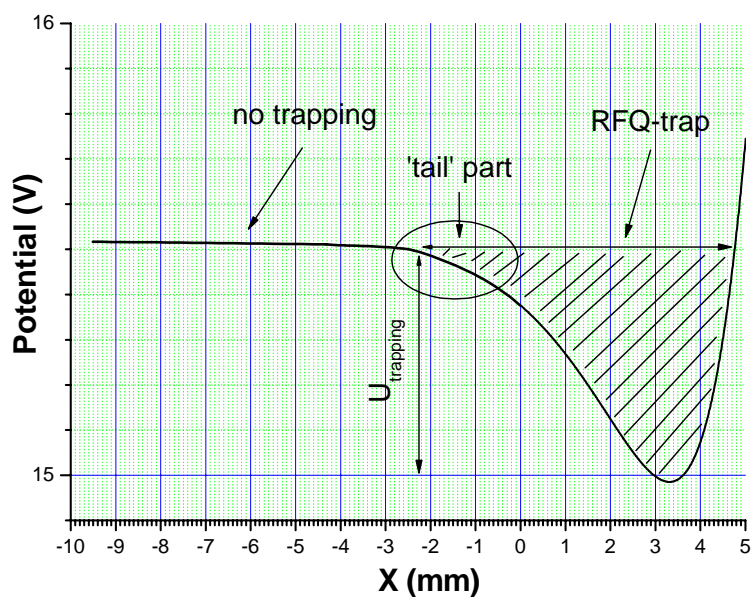


Fig.(A3-6): A magnified version of Fig.(A4-3) (storage regime). Along axis X a spatial dimension of the linear RFQ trap is presented, along axis Y a depth of the linear RFQ trap in Volts is shown. The zero-reference point of axis X is chosen arbitrarily.

Appendix 4

Space charge of He-ions, created in the stopping volume of the gas cell during the stopping of the primary beam

Let us consider stopping of ions of interest in a gas. The ions slowing down in the gas ionize the gas creating pairs of electrons and positively charged ions along the stopping path. Usually an external electrical field E_{ext} is applied along the gas in order to drag the ions of interest in a chosen direction. Due to this field the electrons being much lighter than the positively charged ions leave the stopping volume much faster than the positively charged ions. Thus, in the stopping volume a cloud of space charge of positively charged ions occurs. This cloud creates an electrical field $E_{space\ charge}$ directed oppositely to E_{ext} . The larger the number of ions of interest entering the stopping volume the stronger the $E_{space\ charge}$. At some intensity of ions of interest the $E_{space\ charge}$ can compensate the E_{ext} . This results in a much longer evacuation time of ions of interest from the stopping volume. Quantitative calculation of the $E_{space\ charge}$ at which the compensation takes place is based on [Huy02]. This calculation was applied to the experiment with the SHIPTRAP gas cell taken place in Garching. As ions of interest a $^{107}\text{Ag}^{17+}$ -beam from a tandem accelerator was used. The beam entered the gas cell with a kinetic energy of 23 MeV and was stopped in He maintained at 30 mbar. A schematic view of the SHIPTRAP gas cell is presented in Fig.(A4-1).

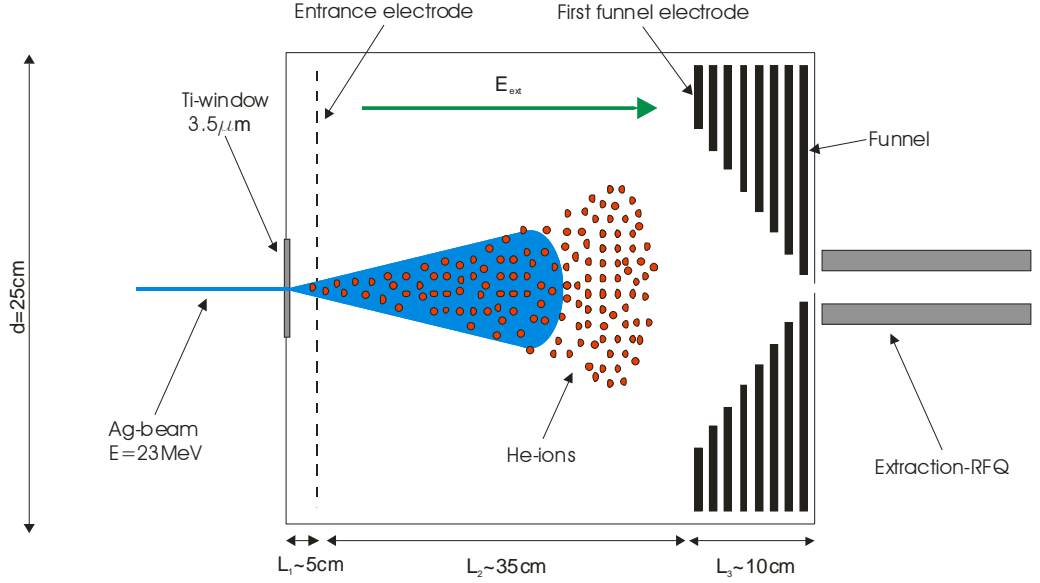


Fig.(A4-1): Stopping of the Ag-beam in the gas cell. The Ag-ions entering the gas cell ionize the buffer gas creating pairs of electrons-He-ions along the stopping path. An external electrical field E_{ext} is applied along the gas cell in order to drag the Ag-ions towards the nozzle of the gas cell.

L_1 , L_2 and L_3 are the distance between the Ti-window and the entrance electrode, the length of the stopping volume of the gas cell, the length of the funnel correspondently, d is the diameter of the gas cell. $E_{space\ charge}$ can be obtained from the following formula [Huy02]:

$$E_{space\ charge} = \frac{e}{4\pi\epsilon_0} (s_i)^{\frac{2}{3}} \quad (\text{A4}_1)$$

where e is the charge of the electron, ϵ_0 is the permittivity of vacuum, s_i is the space charge of the He-ions in the equilibrium. The s_i can be obtained from the following expression [Huy02]:

$$s_i = \sqrt{\frac{B}{\alpha}} \quad (\text{A4}_2)$$

where B is the number of He-ion-electron pairs created in an unit volume per second (ionization rate), α is recombination coefficient, which can be derived from the experimental formula [Way73] : $\alpha = 1,15 * 10^{-8} + 3,86 * 10^{-10} P \left[\frac{cm^3}{s} \right]$, where P is the He pressure in the gas cell in Torr. For $P = 30$ mbar α amounts to $1,3 * 10^{-8} cm^3/s$.

Substituting Eq.(A4_2) into Eq.(A4_1) the following expression for $E_{space\ charge}$ is obtained:

$$E_{space\ charge} = \frac{e}{4\pi\epsilon_0} \left(\frac{B}{\alpha} \right)^{\frac{1}{3}} \quad (A4_3)$$

Substituting the numerical values for $e, \pi, \epsilon_0, \alpha$ one has

$$E_{space\ charge} = 6.1 * 10^{-5} B^{\frac{1}{3}} \left[\frac{V}{m} \right] \quad (A4_4)$$

where B is in $1/(\text{cm}^3\text{s})$. The variable B is a function of several parameters:

$$B = f(L, R, \epsilon, N_{Ag}) \quad (A4_5)$$

where L, R are the longitudinal and radial coordinates of the gas cell (see Fig.(A4-2)), ϵ is the energy losses of the incoming beam per length unit, N_{Ag} is the number of the ions of the incoming beam.

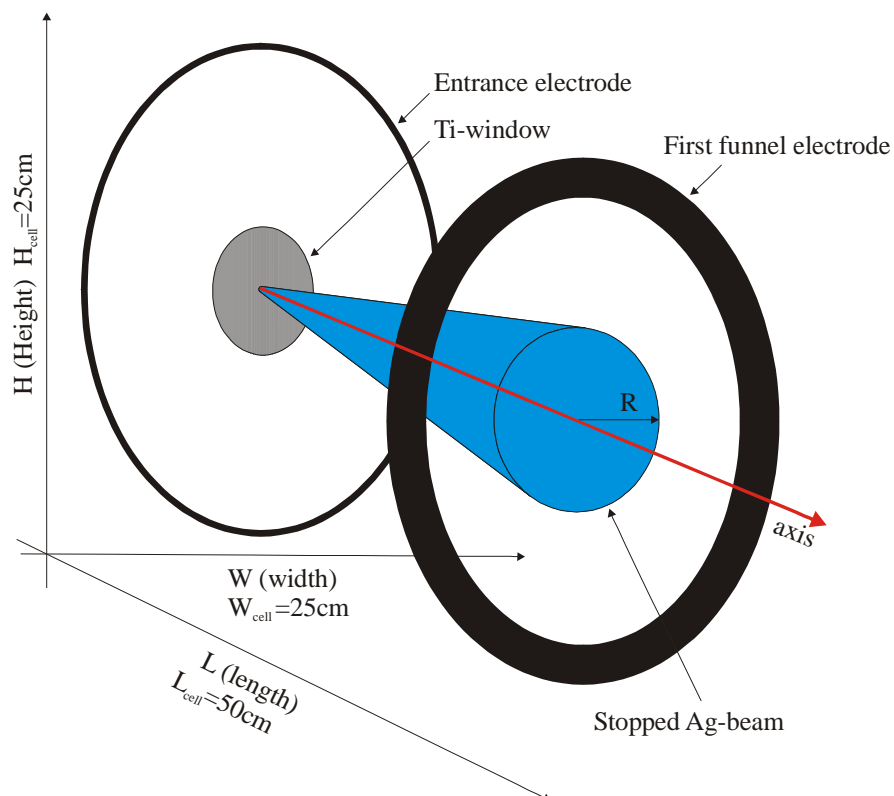


Fig.(A4-2): Stopping of the Ag-ions in the gas cell. L, R are the longitudinal and radial coordinates of the gas cell

In order to determine the function $f(L,R,\varepsilon,N_{Ag})$ a SRIM[Sri00]-simulation was performed. The following input parameters were taken:

The thickness of the Ti-window is 3.5 μm , the He pressure in the gas cell is 30 mbar, the initial kinetic energy of the ^{107}Ag -beam is 23 MeV, the number of ^{107}Ag -ions is 5000.

As a result, the longitudinal distribution of stopped ions, the radial distribution of stopped ions at different L, and the energy losses of ^{107}Ag -ions as a function of their kinetic energy were calculated.

The longitudinal distribution of stopped ions is shown in Fig.(A4-3).

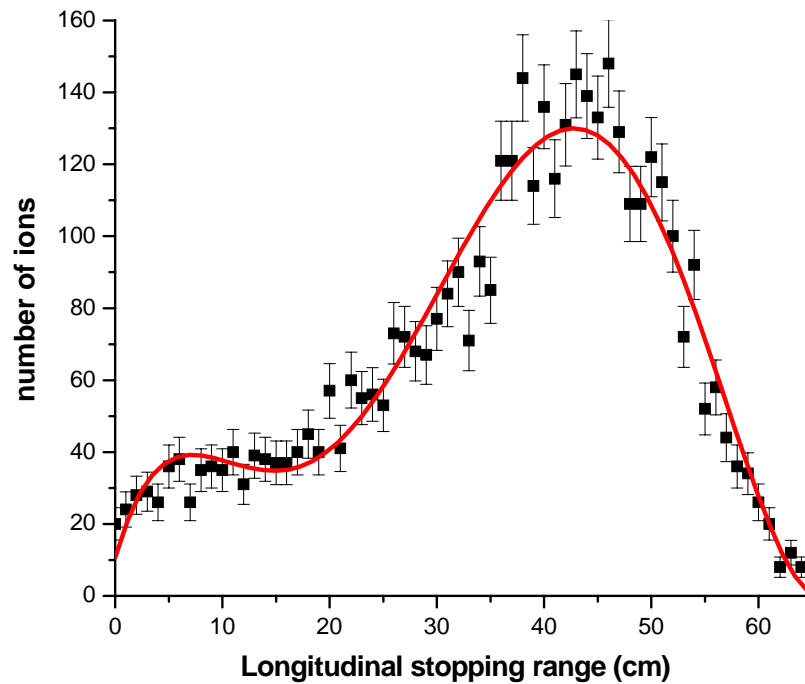


Fig.(A4-3): Longitudinal range distribution of stopped ^{107}Ag -ions with initial kinetic energy of 23 MeV in the gas cell at 30 mbar He-pressure [Sri00]

A polynomial of order 5 was fitted into the experimental data (red curve in Fig.(A4-3)). Dividing the fitting curve by the area under the curve (the total number of the ions stopped in the gas cell) one obtains an expression for the longitudinal stopping curve independent from the number of the ^{107}Ag -ions stopped in the gas cell

$$S_{long}(L):$$

$$S_{long}(L) = 3.6 * 10^{-4} + 3.5 * 10^{-4} L - 4.3 * 10^{-5} L^2 + 2 * 10^{-6} L^3 - 3.4 * 10^{-8} L^4 + 2.3 * 10^{-10} L^5 \quad (\text{A4}_6)$$

where L should be in cm. The radial stopping range and straggling as a function of L is shown in Fig.(A4-4). The calculated value of the mean radial stopping range is shown in black circles. The blue curve is a fitting curve $R_{mean}(L)$ for these points (a polynomial of order 2). The error bars and the red curves $R_{up}(L)$, $R_{down}(L)$ fitted into them correspond to FWHM of the radial stopping range distribution.

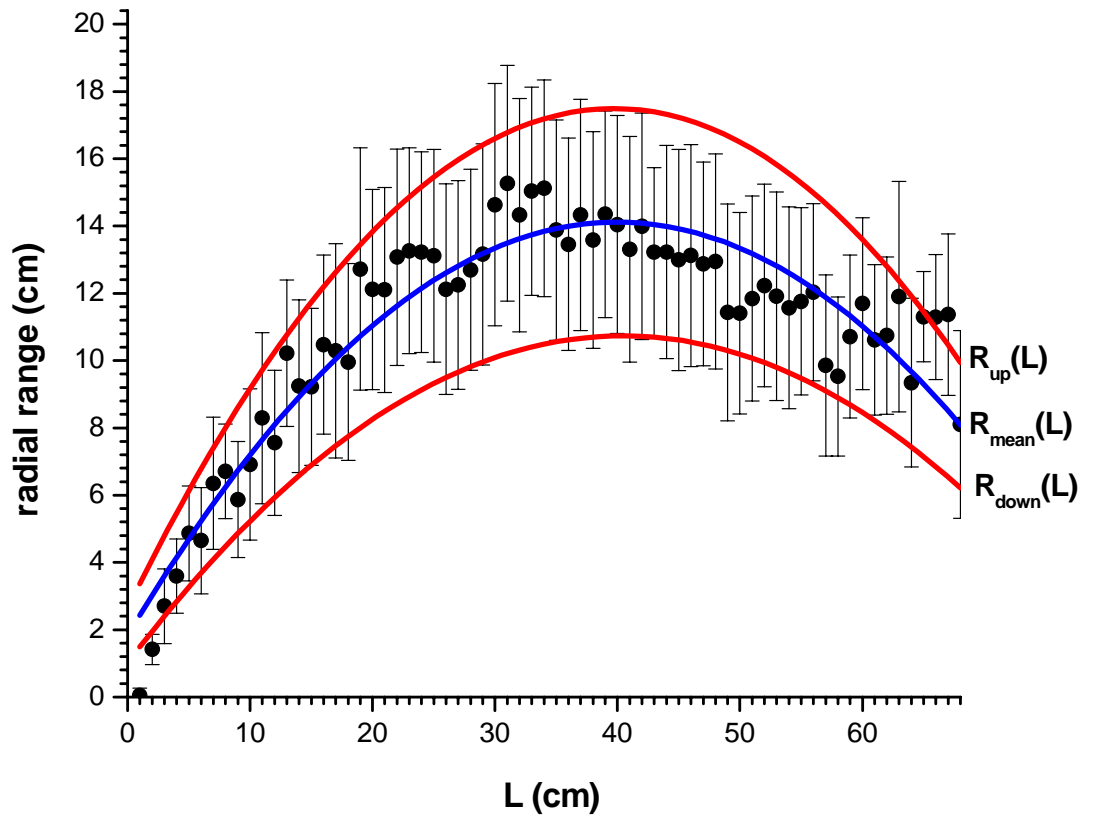


Fig.(A4-4): The radial stopping range and straggling of ^{107}Ag -ions with initial kinetic energy of 23 MeV as a function of the length of the gas cell [Sri00]

The result of the fitting for $R_{mean}(L)$ and $\Delta R(L) = R_{up}(L) - R_{down}(L)$ is shown in Eqs.(A4_7) and (A4_8).

$$R_{mean}(L) = 1.8 + 0.6 * L - 0.0077 * L^2 \quad [\text{cm}] \quad (\text{A4}_7)$$

$$\Delta R(L) = 2.6 + 0.27 * L - 0.0034 * L^2 \quad [\text{cm}] \quad (\text{A4}_8)$$

where L is in cm. After the ^{107}Ag -ions have passed the Ti-window they have a kinetic energy of (2.5 ± 1) MeV [Sri00]. The energy losses ε of the ^{107}Ag -ions in He at 30 mbar for kinetic energies ranging from 0 to 3.5 MeV is presented in Fig.(A4-5). It can be seen that the energy losses over the given energy range differ by maximum 20% with respect to ^{107}Ag -ions kinetic energy. For the simplicity of the calculation one can take ε equal to 0.06 MeV/cm over the whole kinetic energy range of interest.

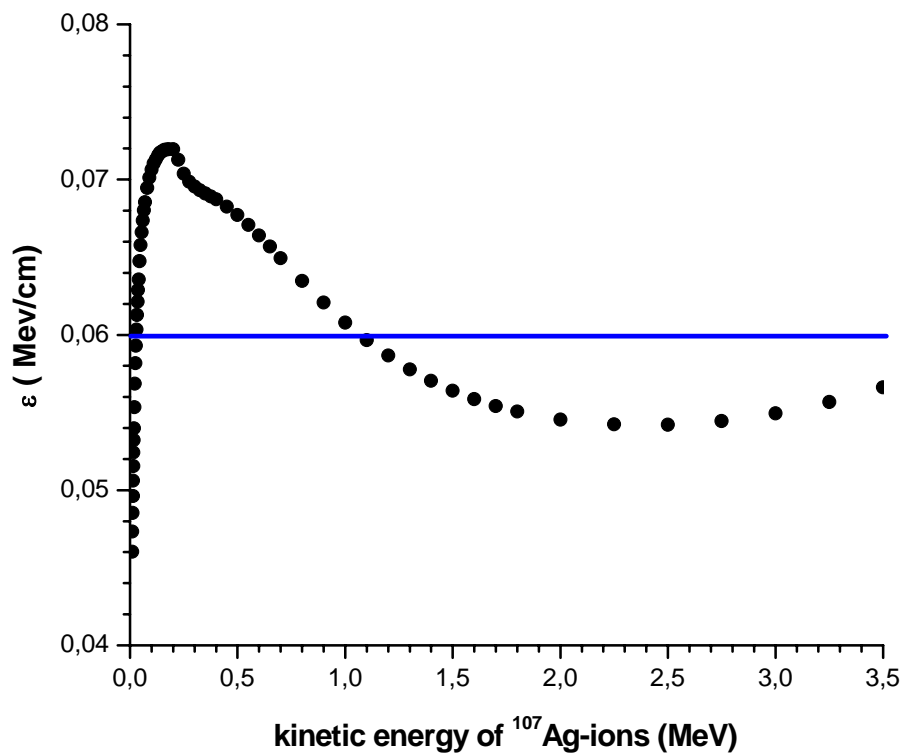


Fig.(A4-5): The energy losses of the ^{107}Ag -ions in He at 30 mbar as a function of the kinetic energy of the ^{107}Ag -ions [Sri00]

The stopping volume can be cut into layers parallel to W-H-plane (see Fig.(A4-2)). The position of the layers is described by the L . The energy $E(L)$ that is deposited into the layer located at L can be expressed as follows:

$$E(L) = \varepsilon * N_{Ag} * \int_L^{L_{MAX}} S_{long}(L) dL \quad (\text{A4}_9)$$

where $S_{long}(L)$ is taken from Eq.(A4_6), $L_{max}=65\text{ cm}$ (see Fig.(A4-3)).The stopping volume of the layer located at L is given by Eq.(A4_10):

$$V(L) = \pi * (R_{up}(L)^2 - R_{down}(L)^2) = 2\pi * R_{mean}(L) * \Delta R(L) \text{ [cm}^3\text{]} \quad (\text{A4}_{10})$$

The ionization rate B is a product of $E(L)$, $V(L)$ and the energy $E_{pair}=41\text{eV}$ required for creating one He-electron pair:

$$B(L) = \frac{E(L)}{V(L) * 41} \left[\frac{\text{pairs}}{\text{cm}^3 \text{ s}} \right] \quad (\text{A4}_{11})$$

The ratio $B(L)/N_{Ag}$ is plotted in Fig.(A4-6) as a function of L .

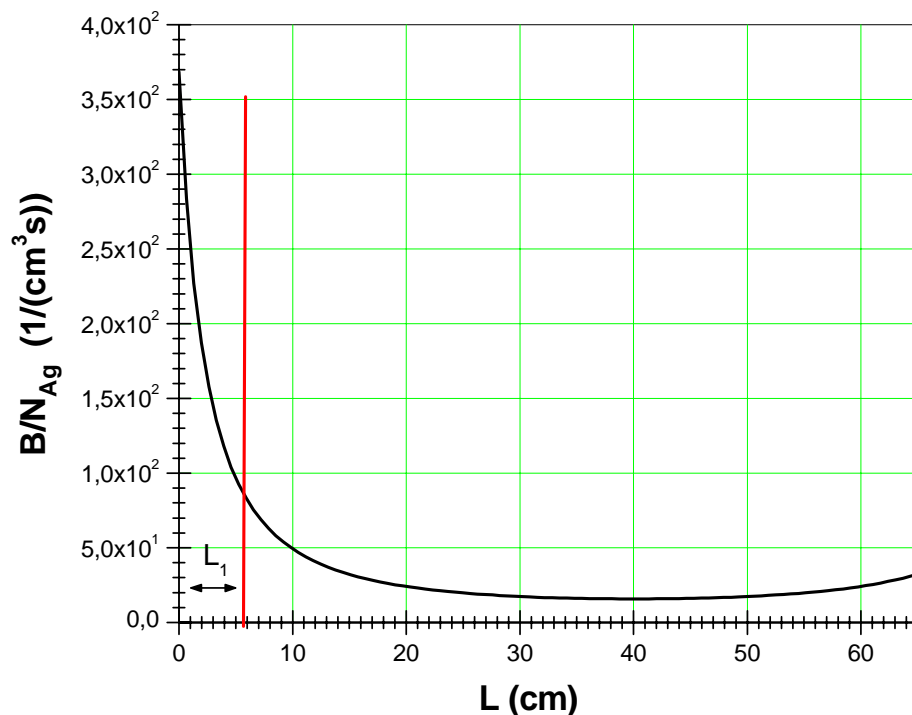


Fig.(A4-6):The ionization rate (the number of He-ion-electron pairs created in an unit volume per second) normalized to the number of Ag-ions N_{Ag} entering the gas cell as a function of the length of the gas cell L [Sri00]

The region between $L=0$ and $L=5\text{ cm}$ can be excluded because it is situated between the Ti-window and the entrance electrode (see Fig.(A4-1)) and does not belong to

the stopping volume. In the remaining volume, the ionization rate can be taken to be approximately constant and equal to $\sim 25 * N_{Ag} \text{ pairs}/(\text{cm}^3\text{s})$. A slightly higher ionization at the entrance electrode does not distort the whole picture because almost all Ag-ions still have high kinetic energy and hardly feel the space charge created about the entrance electrode. Substituting $B=25 * N_{Ag} \text{ pairs}/(\text{cm}^3\text{s})$ into Eq.(A4_4) one can obtain for $E_{space \text{ charge}}$:

$$E_{space \text{ charge}} = 1.8 * 10^{-2} (N_{Ag})^{\frac{1}{3}} \left[\frac{V}{m} \right] \quad (\text{A4}_{12})$$

Making E_{ext} equal to $E_{space \text{ charge}}$ (compensation of two fields) one can obtain the number of the Ag-ions N_{Ag}^{comp} needed for creating the compensating field:

$$N_{Ag}^{comp} = 1.7 * 10^5 E_{ext}^3 \left[\frac{\text{ions}}{s} \right] \quad (\text{A4}_{13})$$

where E_{ext} is in V/m.

Appendix 5

Geometry and electrical settings of the Ortho-TOF mass spectrometer

Designation	Length, mm
l_1	12
l_2	62.1
l	956.1
l_3	242
l_4	88

Table A5_1: Typical geometrical parameters of the Ortho-TOF-MS [see Fig.(2-4)]

Designation	Potential, V
$U_{\text{pulser+}}$	1000
$U_{\text{pulser-}}$	-1000
$U_{\text{acceleration}}$	-6000
U_{grid}	-300
$U_{\text{back plate}}$	+1300
$U_{\text{MCP-}}$	-6000
$U_{\text{MCP+}}$	-3300

Table A5_2: Typical electric potentials used in the TOF-analyzer

App. 5 Geometry and electrical settings of the Ortho-TOF MS XXVII

Designation	Potential, V
$U_{\text{Skimmer 1}}$	18
U_{begin}	10
U_{end}	27.5
$U_{\text{trapping electrode}}$	0
$U_{\text{Skimmer 2}}$	0 (continuous mode) 20 (bunch mode)
U_{DCQ} : up down left right	11 11 11 11
$U_{\text{output orifice}}$	-40
$U_{\text{einzel lens}}$: up down	from -10 to -20 from -10 to -20

Table A5_3: Typical electric potentials applied to the LINAC-quadrupole

Acknowledgement

I would like to thank everybody, who supported me in my work.

In particular, I would like to express my thanks to my supervisor Prof. Dr. Hans Geissel for having given me the opportunity to work on the development of the Ortho-TOF mass spectrometer in IONAs-group of the II Physical Institute, Giessen. Without his large personal support of this research work I would not be able to achieve my doctor degree.

I wish to express my gratitude to Prof. Dr. Yuri Novikov. He has been my supervisor in Russia since my study at St. Petersburg State University. His guidance over this period enabled my formation as a nuclear physicist.

I am grateful to Pr. Dr. Hermann Wollnik for my invitation to the II Physical Institute, Giessen. His continuous support and inexhaustible energy helped me get familiar with the world of the experimental physics.

My special thanks are addressed to Prof. Dr. Alexander Dodonov and his wife Tamara Dodonova for my introduction into the experimental time-of-flight mass spectrometry. Their professional skills and amiable personalities have been impressed in my memory.

I would like to thank all current as well as former members of the IONAs-group: Dr. C. Scheidenberger, Dr. W. Plass, Dr. Zhen Zhou, Dr. M. Weidenmueller, Dipl. Phys. Z. Wang for their instructive advices and fruitful discussions about experiments during my work.

I appreciate the technical support and professional advices of Mr. R. Weiss and his team from the workshop of the II Physical Institute.

The help of Mrs. Momberger in the arrangements of my professional and campus life is gratefully appreciated.

Last, but certainly not least, I wish to thank my wife Natalia for her love and support.

References

- [Aud03] **G.Audi et al.**, Nuclear Phys, A729 (2003) 3
- [Aug94] **G. Auger, W. Mittig, A. Lépine-Szily, L. K. Fifield, M. Bajard, E. Baron, D. Bibet, P. Bricault, J. M. Casandjian, M. Chabert, M. Chartier, J. Fermé, L.Gaudard, A. Gillibert, M. Lewitowicz, M. H. Moscatello, N. A. Orr, E. Plagnol, C. Ricault, A. C. C. Villari, and Yang Yong Feng**, *A cyclotron as a high resolution mass spectrometer for fast secondary ions*, Nucl. Instrum. Methods A 350 (1994) 235
- [Be089] **T. Bergmann, P. Martin and H. Schaber**, Rev. Sci. Instrum., 60(4) (1989) 792
- [Be189] **T. Bergmann, P. Martin and H. Schaber**, Rev. Sci. Instrum., 60(3) (1989) 347
- [Be090] **T. Bergmann, P. Martin and H. Schaber**, Rev. Sci. Instrum., 61(10) (1990) 2592
- [Bia89] **L. Bianchi, B. Fernández, J. Gastebois, A. Gillibert, W. Mittig, and J. Barrette**, *SPEG: An energy loss spectrometer for GANIL*, Nucl.Instrum. Methods A276 (1989) 509
- [Bol87] **G. Bollen et al.**, *First absolute mass measurements of short-lived isotopes*, Hyp. Int. 38 (1987) 793
- [Cam48] **A. E. Cameron, D. F. Eggers Jr.**, An Ion “Velocitron”, Rev. of Sci. Instrum., Vol. 19 (1948) 605
- [Daw76] **P. H. Dawson,ed.**, *Quadrupole Mass Spectrometry and Its Applications*, Elsevier scientific publishing company, North-Holland, Amsterdam, (1976)

- [Daw87] **J. H. J. Dawson and M. Guilhaus (inventors)**, Australian Provisional Patent, P16079 Unisearch Limited, Dec. (1987)
- [Deh67] **H. G. Dehmelt**, *Advan. At. Mol. Phys.*, 3 (1967) 53
- [Del00] **Del Mar Ventures**, <http://www.sciner.com/MCP/> (9.04.2004)
- [Dge74] **B. S. Dgeleпов**, “Analysis methods of complex decay schemes”, Science, Leningrad 1974
(Original: Б. С. Джелепов, “Методы разработки сложных схем распада“, Наука, Ленинград 1974)
- [Die92] **Gerlich Dieter**, Inhomogeneous RF fields: a versatile tool for the study of processes with slow ions in State-Selected and State-to-State Ion-Molecule Reaction Dynamics. Part 1. Experiment. Ed. By Cheuk-Yiu Ng and Michael Baer. *Advances in Chemical Physics Series*, 1992, Vol. LXXXII
- [Dil00] **J. Dilling, D. Ackermann, J. Bernard, F. P. Hessberger, S. Hoffmann, H. J. Kluge, E. Lamour, M. Maier, R. Mann, G. Marx, G. Münzenberg, W. Quint, D. Rodríguez, M. Schädel, J. Schönfelder, G. Sikler, C. Toader, L. Vermeeren, C. Weber, G. Bollen, O. Engels, D. Habs, P. Thirolf, H. Backe, A. Dretzke, W. Lauth, W. Ludolphs, M. Sewtz, and the SHIPTRAP Collaboration**, The SHIPTRAP project: A capture and storage facility at GSI for heavy radionuclides from SHIP, *Hyp. Int.* 127 (2000) 491
- [Dil01] **J. Dilling, D. Ackermann, F. P. Hessberger, S. Hoffmann, H. J. Kluge, G. Marx, G. Münzenberg, Z. Patik, W. Quint, D. Rodríguez, C. Scheidenberger, J. Schönfelder, G. Sikler, A. Sobiczewski, C. Toader, and C. Weber**, *A Physics Case for SHIPTRAP: Measuring the Masses of Transuranium Elements*, *Hyp. Int.* 132 (2001) 495
- [Dod87] **A. F. Dodonov, I. V. Chernushevich, T. F. Dodonova, V. V. Raznikov, V. L. Tal'rose**, Inventor's Certification No. 168134OA1, USSR, Feb. 15 (1987)

- [Dod91] **A. F. Dodonov, I. V. Chernushevich, V. V. Laiko**, Atmospheric pressure ionization time-of-flight mass spectrometer, 12th-International Mass Spectrometry Conference, Amsterdam, book of abstracts, TuA-D20 (1991) 53
- [Dod94] **A. F. Dodonov and V. V. Laiko**, Rapid Comm. In Mass Spectr., Vol. 8 (1994) 720
- [Dod97] **A. F. Dodonov, V. Raznikov, S. Koslovsky, A. Loboda, A. Kraft, Zh. Zhou, T. Horvath, M. Andreessen and H. Wollnik**, Volkswagen Project Report 1997
- [Dou92] **D. J. Douglas and J. B. French**, Collisional Focusing Effects in Radio Frequency Quadrupoles. J. Am. Soc. Mass. Spectrom. 3 (1992) 398-408
- [Fen89] **J. B. Fenn et al.**, Science, 246 (1989) 64
- [Fen93] **J. B. Fenn**, Journal of the American Society for Mass Spectrometry, 4 (1993) 524-535
- [Fra87] **B. Franzke**, *The heavy ion storage and cooler ring project ESR at GSI*, Nucl. Instrum. Methods B 24/25 (1987) 18
- [Gei92] **H. Geissel et al.**, *The GSI projectile fragment separator (FRS): a versatile magnetic system for relativistic heavy ions*, Nucl. Instrum. Methods B 70 (1992) 286
- [Gie84] **J. Gieniec, L. L. Mack, K. Nakamae, C. Gupta, V. Kumar, M. Dole**, Biomedical Mass Spectrometry, (1984) 259-268
- [Gru94] **J. M. Grundwuermer, M. Boenisch, G. R. Kinsel, J. Grottemeyer and E. W. Schlag**, Inter. J. Of Mass Spectro. and ion Proc., 131 (1994) 139
- [Gsi01] GSI Jahresbericht 2001, "SHIPTRAP: A Capture and Storage Facility for Radionuclides from SHIP "
- [Has72] **J. B. Hasted**, Physics of atomic collisions, Second Edition 1972

- [Her03] **F. Herfurth et al.**, *Mass measurements and nuclear physics-recent results from ISOLTRAP*, J. Phys. B: At. Mol. Opt. Phys. 36 (2003) 931
- [Huy02] **Mark Huysse, Marius Facina, Yuri Kudryavtsev, Piet Van Duppen, ISOLDE collaboration**, Nuclear Instruments and Methods in Physics Research B 187 (2002) 535-547
- [Kar88] **M. Karas and F. Hillenkamp**, Anal. Chem., 60 (1988) 2299
- [Kev85] **R. B. Kevin, K. G. Owens and J. P. Reilly**, Anal. Chem. 57 (1985) 1884
- [Koz99] **V. Kozlovsky**, Doctor Thesis, "Development of methods for investigation of ions extracted from solutions into gaseous phase with help of a high-resolution time-of-flight mass spectrometer ", Chernogolovka, 1999
(Original: В. Козловский, кандидатская диссертация, "Разработка методов исследования экстрагированных из раствора в газовую фазу ионов с помощью время-пролётного масс-спектрометра высокого разрешения ", Черногоровка, 1999)
- [Kru95] **A. N. Krutchinsky, I. V. Chernushevich, W. Ens, V. L. Spicer, K. G. Standing**, Proceedings of the 43rd ASMS Conference of Mass Spectrometry and Allied Topics, (1995) 126
- [Kru98] **A. N. Krutchinsky, I. V. Chernushevich, W. Ens, V. L. Spicer, K. G. Standing**, Collisional Damping Interface for an Electrospray Ionization Time-of-Flight Mass Spectrometer. Journal of American Society of Mass Spectrometry, 9 (1998) 569-579
- [Lan73] **L. D. Landau, E. M. Livshic**, "Mechanics", Science, Moscow 1973
(Original: Л. Д. Ландау, Е. М. Лившиц, Механика, "Наука", Москва 1973)
- [Lob98] **A. N. Krutchinsky, A. V. Loboda, V. L. Spicer, R. Dworschak, W. Ens and K. G. Standing**. Orthogonal Injection of Matrix-assisted Laser

Desorption/Ionization Ions into a Time-of-Flight Spectrometer Through a Collisional Damping Interface. *Rapid Communications in Mass Spectrometry* 12 (1998)508-518

[Lun01] **D. Lunney, G. Audi, H. Doubre, S. Henry, C. Monsanglant, M. de Saint Simon, C. Thibault, C. Toader, C. Borcea, G. Bollen, and the ISOLDE collaboration**, *Precision mass measurements of very short-lived, neutron-rich Na isotopes using a radio-frequency spectrometer*, *Phys. Rev. C* 64 (2001) 054311

[Mam73] **B. A. Mamyrin, V. I. Karataev, D. V. Shmikk, V. A. Zagulin**, *Soviet Phys., JEPT*, Vol.37 (1973) 45

[Mas49] **H. S. W. Massey**, *Rep. Prog. Phys.* 12 (1949) 248

[Mar89] **R. E. March and R. J. Hughes**. *Quadrupole Storage Mass Spectrometry*, Wiley-Interscience, New-York, (1989) 332-333

[Maj68] **F. G. Major and H. G. Dehmelt**, “*Exchange-collision technique for the rf Spectroscopy of stored ions*”, *Phys. Rev.* 170 (1968) 91

[Men88] **C. K. Meng, M. Mann and J. B. Fenn**, *Zeitschrift fuer Physik D: Atoms, Molecules and Clusters*, 10 (1988) 361

[Moo88] **R. B. Moore, S. Gulick**, *The Transfer of Continuous Beams and Storage Ring Beams into Electromagnetic Traps*, *Physica Scripta*, Vol.T22 (1988) 28-35

[Mün79] **G. Münzenberg, W. Faust, S. Hofmann, P. Armbruster, K. Güttner, and H. Ewald**, *The velocity filter ship, a separator of unslowed heavy ion fusion products*, *Nucl. Instrum. Methods* 161 (1979) 65

[Neu] **J. Neumayr**, PhD Thesis, LMU Munich, Germany, in preparation

[Nuc00] <http://chemlab.pc.maricopa.edu/periodic/default.html> (9.04.2004)

[Pau53] **W. Paul and H. Steinwedel**, *Z. Naturforsch*, A8 (1953) 448

- [Pfe68] **R. J. Pfeifer, C. D. Hendricks**, AIAA J.,6 (1968) 496
- [Piy99] **C. K. G. Piyadasa, P. Haakenson, T. R. Ariyaratne**, Rapid Commun. Mass Spectrom., 13(1999) 620
- [Pos53] **R. F. Post**, Univ. Calif. Radiat. Lab. Rep. U. C. R. L. 2209, 1953
- [Pro00] **PROXITRONIC**, <http://www.proxitronic.de> (9.04.2004)
- [Ray82] **L. Rayleigh**, Philos. Mag., 14 (1882) 184
- [Rut81] **J. A. Rutherford and D. A. Vroom**, J. Chem. Phys. 74(1), 1 Jan. 1981
- [Sav01] **G. Savard, R. C. Barber, C. Boudreau, F. Buchinger, J. Caggiano, J. Clark, J. E. Crawford, H. Fukutani, S. Gulick, J. C. Hardy, A. Heinz, J. K. P. Lee, R. B. Moore, K. S. Sharma, J. Schwartz, D. Seweryniak, G. D. Sprouse, and J. Vaz**, *The Canadian Penning Trap Spectrometer at Argonne*, Hyp. Int. 132 (2001) 223
- [Sik03] **G. Sikler, D. Ackermann, F. Attallah, D. Beck, J. Dilling, S. A. Elisseev, H. Geissel, D. Habs, S. Heinz, F. Herfurth, F. P. Hessberger, S. Hoffmann, H. J. Kluge, C. Kozhuharov, G. Marx, M. Mukherjee, J. Neumayr, W. R. Plass, W. Quint, S. Rahaman, D. Rodríguez, C. Scheidenberger, M. Tarisien, P. Thirolf, V. Varentsov, C. Weber, and Z. Zhou**, *First on-line test of SHIPTRAP*, Nucl. Instrum. Methods B 204 (2003) 482
- [Sim00] “SIMION 3D Version 6” by David A. Dahl 43ed ASMS Conference on Mass Spectrometry and Allied Topics, May 21-26 1995, Atlanta, Georgia, pg 717
- [Sri00] <http://www.srim.org> (9.04.2004)
- [Sta59] **A. M. Stashkevich**, “*Electron optics of non-symmetrical electrostatic fields*”, State Publishing House of physical and mathematical literature, Moscow 1959. (Original: A. M. Сташкевич, “*Электронная оптика электростатических полей*”)

не обладающих осевой симметрией“, Государственное издательство физико-математических наук, Москва 1959)

[Tal62] **V. L. Talrose**, Pure Appl. Chem. 5 (1962) 455

[Tol00] **A. V. Tolmachev, H. R. Udseth, and R. D. Smith**, Anal. Chem., 72 (2000) 970-978

[To097] **A. V. Tolmachev, I. V. Chernushevich and K. G. Standing**, Proceedings of the 45th ASMS Conference on Mass Spectrometry and Allied Topics, 1997

[Tol97] **A. V. Tolmachev, I. V. Chernushevich, A. F. Dodonov, K. G. Standing**. A collisional focusing ion guide for coupling an atmospheric ion source to a mass spectrometer. Nucl. Instr. And Meth. In Phys. Res., B 124 (1997) 112-119

[Val00] **L. Vályi**, Atom and ion sources, A Wiley-Interscience publication, New-York, (1977) 46-51

[Way73] **A. Wayne Johnson and J. B. Gerardo**, Physical Review A, Vol. 7, Num. 4 (1973)

[Wil55] **W. C. Wiley, I. H. McLaren**, Time-of-Flight Mass Spectrometer with Improved Resolution, Rev. of Sci. Instrum., 26(1955) 1150-1156

[Wil00] “Mass Spectrometry Reviews”, Wiley InterScience Vol. 19, Number 2 (2000)

[Wiz79] **J. L. Wiza**, Nucl. Instrum. And Meth., Vol. 162 (1979) 587

[Wol87] **H. Wollnik**, Optics of Charged Particles, Academic Press, Inc., 1987

[Wol99] **A. Casares, A. Kholomeev, N. Nankov, R. Roll, H. Rosenbauer, H. Wollnik**, Proc. 47th ASMS Conf., Dallas, (1999)

-
- [Wue59] **R. F. Wuerker, H. Shelton, and R. V. Langmuir**, “*Electrodynamic containment of charged particles*”, J. Appl. Phys., 30 (1959) 342
- [Wur94] **P. Wurz and L. Gubler**, Rev. Sci. Instrum., 65(4) (1994) 871
- [Wur96] **P. Wurz and L. Gubler**, Rev. Sci. Instrum., 67(5) (1996) 1790
- [Zhe00] **Zhen Zhou**, Doctor Thesis, “A High Mass Resolving Power Time-of-Flight Mass Spectrometer with Orthogonal Extraction and a Gas-Filled Radio Frequency Quadrupole Interface”, JLU Giessen, 2000